

A GENERALIZED THEORY OF DOUBLE-RESONANCE  
LASER-PUMPED HELIUM-4 MAGNETOMETERS

by

Michael K. Plante

APPROVED BY SUPERVISORY COMMITTEE:

---

Duncan L. MacFarlane, Chair

---

Lawrence J. Overzet

---

William Frensley

---

Robert E. Slocum

---

Joseph M. Izen

Copyright 2010

Michael K. Plante

All Rights Reserved

A GENERALIZED THEORY OF DOUBLE-RESONANCE  
LASER-PUMPED HELIUM-4 MAGNETOMETERS

by

MICHAEL K. PLANTE, B.S.E.E., B.S.C.S., M.S.E.E.

DISSERTATION

Presented to the Faculty of

The University of Texas at Dallas

in Partial Fulfillment

of the Requirements

for the Degree of

DOCTOR OF PHILOSOPHY IN ELECTRICAL ENGINEERING

THE UNIVERSITY OF TEXAS AT DALLAS

August, 2010

## PREFACE

This dissertation was produced in accordance with guidelines that permit the inclusion as part of the dissertation the text of an original paper or papers submitted for publication. The dissertation must still conform to all other requirements explained in the “Guide for the Preparation of Master’s Theses and Doctoral Dissertations at The University of Texas at Dallas.” It must include a comprehensive abstract, a full introduction and literature review and a final overall conclusion. Additional material (procedural and design data as well as descriptions of equipment) must be provided in sufficient detail to allow a clear and precise judgment to be made of the importance and originality of the research reported.

It is acceptable for this dissertation to include as chapters authentic copies of papers already published, provided these meet type size, margin and legibility requirements. In such cases, connecting texts that provide logical bridges between different manuscripts are mandatory. Where the student is not the sole author of a manuscript, the student is required to make an explicit statement in the introductory material to that manuscript describing the student’s contribution to the work and acknowledging the contribution of the other author(s). The signatures of the Supervising Committee, which precede all other material in the dissertation, attest to the accuracy of this statement.

## ACKNOWLEDGMENTS

I would like to thank Dana Hesse, Leroy Sverduk, and the US Office of Naval Research (ONR) for a grant to complete my research. Thanks are also due to Douglas D. McGregor for enlightening discussions and code to model portions of [34], to Andy W. Brown and William M. Sampson for empirical data and assistance with interpretation, to Robert E. Slocum for general and specific guidance, and to Andres Torres, Jeff Morgan, and Don King for providing information on reference implementations of the electronics and software in a functioning magnetometer.

June, 2010

A GENERALIZED THEORY OF DOUBLE-RESONANCE

LASER-PUMPED HELIUM-4 MAGNETOMETERS

Publication No. \_\_\_\_\_

Michael K. Plante, Ph.D.  
The University of Texas at Dallas, 2010

Supervising Professor: Duncan L. MacFarlane

We extend prior work on laser pumped helium-4 magnetometers to include the effects of an arbitrary three-dimensional Jones vector for the laser light, general arrangement of the  $H_1$  coils, arbitrary orientation of the elements of the instrument, both ranks of the spin-1 state, the Bloch-Siegert shift, and the virtual light shift. The theoretical equations are solved for several specific cases, as well as the general steady-state case, and theoretical plots are shown in cases of practical interest and for parameters that highlight unexpected or previously-unmodeled effects. A detailed examination of the consequences to the quality of the results is made for several of the approximations used. An improved arrangement of the apparatus is suggested for the case of linearly-polarized light. Comparisons are made between experimental data and theory for several modes of operation. The new model is useful for quickly identifying the appropriate parameters to use in order to optimize the sensitivity of double-resonance helium-4 magnetometers.

## TABLE OF CONTENTS

PREFACE .....	iv
ACKNOWLEDGMENTS .....	v
ABSTRACT .....	vi
LIST OF TABLES .....	x
LIST OF FIGURES .....	xi
CHAPTER 1. INTRODUCTION .....	1
CHAPTER 2. BACKGROUND .....	4
2.1 Optical Pumping and Optically Pumped Magnetometers .....	4
2.2 $^4\text{He}$ Magnetometer Concepts .....	8
2.3 $^4\text{He}$ Considerations .....	9
CHAPTER 3. DERIVATIONS .....	14
3.1 Electric Field of Light .....	14
3.2 Excitation and Deexcitation .....	17
3.3 Metastable Evolution With Light .....	21
3.4 Metastable Evolution With Magnetic Field .....	23
3.5 Dipole Matrix Elements .....	24
3.6 Spherical Basis For Spin 1 .....	26
3.7 Light With Spherical Tensors .....	28
3.7.1 General Concerns .....	28
3.7.2 Building Blocks for Expressing Traces .....	31
3.7.3 Traces With Arbitrary Polarization .....	31
3.7.4 Summary Plots .....	32

3.7.5	Compilation of Traces .....	38
3.8	Magnetic Field With Spherical Tensors .....	39
3.8.1	General Concerns .....	40
3.8.2	Orientation Issues .....	41
3.8.3	Compilation of Magnetic Evolution Equations .....	44
3.9	Doppler Broadening .....	46
3.10	State Space Form .....	50
3.10.1	Rotating Coordinates .....	52
3.11	Cell Slicing .....	53
CHAPTER 4. SPECIAL-CASE SOLUTIONS .....		57
4.1	Z-Aligned LCP ( $\sigma$ ) .....	58
4.2	Z-Linearly-Polarized ( $\pi$ -Parallel) .....	61
4.3	Linearly-polarized against Z ( $\pi$ -Perpendicular) .....	68
CHAPTER 5. GENERAL STEADY-STATE SOLUTION .....		73
5.1	General Concerns .....	73
5.2	Examples – Pumping with LCP Light ( $\sigma$ ) .....	76
5.2.1	Comparisons With Prior $\sigma$ Theory .....	77
5.2.2	Three Cells .....	81
5.3	Examples – $H_1$ Improvements for Linearly-Polarized Pumping Light .....	83
5.4	Examples – Bloch-Siegert and Virtual Light Shifts .....	86
CHAPTER 6. EXPERIMENTAL DATA .....		89
6.1	Linearly-Polarized ( $\pi$ -Parallel Pumping) Data From 4-12-2010 .....	89
6.2	Fits to Data with Linearly-Polarized Light .....	92
6.3	LCP ( $\sigma$ -pumping) Data From 5-5-2010 .....	101
CHAPTER 7. CONCLUSIONS, APPLICATIONS, AND FUTURE EXTENSIONS .....		105
APPENDIX A. ELECTRIC DIPOLE APPROXIMATION .....		106

APPENDIX B. COORDINATE ROTATIONS.....	108
B.1 3-D Jones Vector.....	109
B.2 3-D Magnetic Field .....	109
B.3 Multiple Cells .....	110
APPENDIX C. REDUCED CROSS SECTIONS WITH ARBITRARY POLARIZATION..	111
APPENDIX D. COMMUTATOR LIST .....	114
D.1 Commutators.....	114
D.2 Anticommutators .....	114
APPENDIX E. FURTHER $\pi$ -PERPENDICULAR CALCULATIONS.....	115
REFERENCES.....	117

VITA

## LIST OF TABLES

1.1	Symbols Introduced In Chapter 1 .....	1
3.1	Symbols Introduced In Section 3.1 .....	14
3.2	Symbols Introduced In Section 3.2 .....	17
3.3	Symbols Introduced In Section 3.4 .....	23
3.4	Symbols Introduced In Section 3.5 .....	24
3.5	Symbols Introduced In Section 3.7 .....	28
3.6	Symbols Introduced In Section 3.8 .....	39
3.7	Symbols Introduced In Section 3.9 .....	46
3.8	Symbols Introduced In Section 3.10 .....	50
4.1	Symbols Introduced In Chapter 4 (Intro Only) .....	57
4.2	Symbols Introduced In Section 4.1 .....	58
4.3	Symbols Introduced In Section 4.2 .....	61
4.4	Symbols Introduced In Section 4.3 .....	68
5.1	Symbols Introduced In Chapter 5 .....	73

## LIST OF FIGURES

1.1	Relevant helium energy levels .....	2
1.2	Helium Absorption Spectrum .....	2
2.1	Representative block diagram of a double-resonance $^4\text{He}$ magnetometer .....	8
2.2	Helium Cell in Operation .....	8
3.1	Local and World Coordinate Systems .....	15
3.2	2-D Polarization .....	15
3.3	$Q_I$ for all polarizations .....	33
3.4	$Q_z$ for LCP light .....	33
3.5	$Q_+$ for LCP light .....	34
3.6	$Q_+$ for RCP light .....	34
3.7	$Q_1$ for LCP light .....	35
3.8	$Q_1$ for almost-LCP light .....	35
3.9	$Q_1$ for linearly-polarized light .....	35
3.10	$Q_1$ for RCP light .....	35
3.11	$Q_0$ for LCP light .....	36
3.12	$Q_0$ for almost-LCP light .....	36
3.13	$Q_0$ for linearly-polarized light .....	36
3.14	$Q_{zz}$ for linearly-polarized light .....	37
3.15	$Q_{+-}$ for linearly-polarized light .....	37
3.16	$Q_2$ for linearly-polarized light .....	37
3.17	$Q_2$ for almost-LCP light .....	37
3.18	Magnetic Field Orientation in Local and World Systems .....	42
3.19	Orientation of Quadrature Field After Approximation .....	43
3.20	Some Example Orientations of the Magnetic Fields .....	43
3.21	$G(\omega')$ Approximation Comparison, Overlay .....	48

3.22	$G(\omega')$ Approximation Comparison, Difference . . . . .	49
3.23	$G'(\omega')$ Approximation Comparison, Overlay . . . . .	49
3.24	$G'(\omega')$ Approximation Comparison, Relative Error . . . . .	49
3.25	Effect of Slice Count, Off-Resonance ( $H_1 = 0$ ) . . . . .	54
3.26	Effect of Slice Count, $\gamma H_0 = \omega$ , $H_1$ Optimized for Each Power . . . . .	54
3.27	Effect of Slice Count, Resonance Curve, $n_S$ Chosen to give 15% in One Case . . . . .	55
3.28	Effect of Slice Count, Resonance Curve, $n_S$ Chosen to give 15% in Each Case . . . . .	56
5.1	Diagram of Matrix Equation Layout for $m_o = 3$ . . . . .	76
5.2	Resonance curve for typical circularly-polarized configuration . . . . .	77
5.3	Slope of resonance curve for circularly-polarized configuration . . . . .	78
5.4	Shot-noise sensitivity for circularly-polarized configuration . . . . .	78
5.5	Shot-noise for circularly-polarized configuration over laser power and $H_1$ strength . . . . .	79
5.6	Inflection point , circularly-polarized light, over laser power and $H_1$ strength . . . . .	80
5.7	Optimal $H_1$ amplitude as a function of laser power, circularly-polarized light . . . . .	80
5.8	Shot-noise sensitivity limit for circularly-polarized configuration over laser power . . . . .	81
5.9	Slope of sum of 3 photodiodes' signals (A/T) . . . . .	82
5.10	Optimal detuning (nT) for sum of 3 photodiode signals . . . . .	82
5.11	Slope of signal from cell 1 (A/T) . . . . .	82
5.12	Optimal detuning (nT) when using only cell 1 . . . . .	82
5.13	Slope of signal from cell 2 (A/T) . . . . .	83
5.14	Optimal detuning (nT) when using only cell 2 . . . . .	83
5.15	Slope of signal from cell 3 (A/T) . . . . .	83
5.16	Optimal detuning (nT) when using only cell 3 . . . . .	83
5.17	Shot-noise floor over orientation, linearly-polarized light, $\xi \approx 54.7^\circ$ . . . . .	84
5.18	Shot-noise floor over orientation, linearly-polarized light, $\xi = 90^\circ$ . . . . .	84
5.19	Shot-noise floor for selected values of $\theta$ , linearly-polarized light, $\xi \approx 54.7^\circ$ . . . . .	85
5.20	Shot-noise floor for selected values of $\theta$ , linearly-polarized light, $\xi = 90^\circ$ . . . . .	85
5.21	Inflection point, linearly-polarized light, $\xi \approx 54.7^\circ$ . . . . .	85
5.22	Inflection point, linearly-polarized light, $\xi = 90^\circ$ . . . . .	85
5.23	Virtual light shift and Bloch-Siegert (BS) shift, at 0.5 mW optical power . . . . .	86

5.24	Derivative of virtual light shift with respect to $\omega'$ .....	87
5.25	Derivative of virtual light shift with respect to $\omega'$ , divided by optical power .....	87
6.1	Theoretical and experimental magnetic resonance curves at $H_1 \approx 52$ nT .....	90
6.2	Theoretical and experimental slopes with varying $H_1$ amplitude .....	91
6.3	Theoretical fit to experimental magnetic resonance curves, for $H_1 \approx 11.8$ nT .....	94
6.4	Theoretical fit to experimental magnetic resonance curves, for $H_1 \approx 18.9$ nT .....	94
6.5	Theoretical fit to experimental magnetic resonance curves, for $H_1 \approx 23.7$ nT .....	94
6.6	Theoretical fit to experimental magnetic resonance curves, for $H_1 \approx 28.4$ nT .....	95
6.7	Theoretical fit to experimental magnetic resonance curves, for $H_1 \approx 35.5$ nT .....	95
6.8	Theoretical fit to experimental magnetic resonance curves, for $H_1 \approx 47.3$ nT .....	95
6.9	Theoretical fit to experimental magnetic resonance curves, for $H_1 \approx 52.1$ nT .....	96
6.10	Theoretical fit to experimental magnetic resonance curves, for $H_1 \approx 59.2$ nT .....	96
6.11	Theoretical fit to experimental magnetic resonance curves, for $H_1 \approx 66.3$ nT .....	96
6.12	Theoretical fit to experimental magnetic resonance curves, for $H_1 \approx 71.0$ nT .....	97
6.13	Theoretical fit to experimental magnetic resonance curves, for $H_1 \approx 82.8$ nT .....	97
6.14	Theoretical fit to experimental magnetic resonance curves, for $H_1 \approx 94.6$ nT .....	97
6.15	Theoretical fit to experimental magnetic resonance curves, for $H_1 \approx 106.5$ nT .....	98
6.16	Theoretical fit to experimental magnetic resonance curves, for $H_1 \approx 118.3$ nT .....	98
6.17	Theoretical fit to experimental magnetic resonance curves, for $H_1 \approx 142.0$ nT .....	98
6.18	Theoretical fit to experimental magnetic resonance curves, for $H_1 \approx 165.6$ nT .....	99
6.19	Theoretical fit to experimental magnetic resonance curves, for $H_1 \approx 189.3$ nT .....	99
6.20	Theoretical fit to experimental magnetic resonance curves, for $H_1 \approx 213.0$ nT .....	99
6.21	Theoretical fit to experimental magnetic resonance curves, for $H_1 \approx 236.6$ nT .....	100
6.22	Fit of $H_1$ , as a function of $H_1$ .....	101
6.23	Fit of $\tau_0^{-1}$ , $\tau_1^{-1}$ , and $\tau_2^{-1}$ , as a function of $H_1$ .....	101
6.24	$\sigma$ -pumping data, cell C, AD in field .....	103
6.25	$\sigma$ -pumping data, cell F, AD in field .....	103
6.26	$\sigma$ -pumping data, cell C, CF in field .....	103
6.27	$\sigma$ -pumping data, cell F, CF in field .....	103
6.28	$\sigma$ -pumping data, cell A, AD in field .....	103

6.29 $\sigma$ -pumping data, cell D, AD in field .....	103
6.30 $\sigma$ -pumping data, cell A, CF in field .....	104
6.31 $\sigma$ -pumping data, cell D, CF in field .....	104

CHAPTER 1  
INTRODUCTION<sup>1</sup>

Table 1.1. Symbols Introduced In Chapter 1

Symbol	Units	Description
$H_0$	nT	Total magnetic field of Earth and any sensed objects
$H_1$	nT	Half the peak magnetic field for 1-axis Helmholtz coils (AC)

The measurement of magnetic fields has a long history with diverse applications [31], and one of the most precise types of magnetic sensors is the optically-pumped magnetometer, which typically uses either an alkali vapor or helium [11]. Helium is often used in space and military applications [2, 17].

McGregor [34] presents a detailed overview of a magnetometer system, while presenting significant detail on much of the relevant quantum mechanics of  $^4\text{He}$ . In this document, we describe the details of the model of McGregor [34] for precision magnetometers and extend it to include arbitrary orientation of all elements, arbitrary polarization of the light, the virtual light shift [27, 50], and the Bloch-Siegert shift [8] within the context of laser pumping of the  $^4\text{He}$   $D_0$  line. We also model orientation-dependence for one common multi-cell magnetometer system. The theory presented here allows the optimization of a large number of parameter selections in the present and next generation of magnetometer instruments and applications. Finally, we present qualitative comparisons with observations and quantitative comparisons with experiments.

The state evolution, governed by the Hamiltonian  $\mathcal{H}$ , is described by five contributions  $\mathcal{H} = \mathcal{H}_0 + \mathcal{H}_L + \mathcal{H}_R + \mathcal{H}_C + \mathcal{H}_M$ , given in [34]: the unperturbed helium Hamiltonian  $\mathcal{H}_0$ , which describes the atoms to the level of fine structure; the spontaneous emission  $\mathcal{H}_R$  from the  $2^3P_J$  excited states  $m$  (see Figure 1.1) to the  $2^3S_1$  metastable states  $\mu$  with lifetime  $\tau \approx 10^{-7}$  s; the

---

<sup>1</sup>A significant portion of the text of this chapter is based on [43], © 2010 American Physical Society.

semiclassical loss  $\mathcal{H}_C$  of metastables through processes such as collisions with walls or with free electrons; the influence  $\mathcal{H}_L$  of the pumping beam on the helium atoms; and the precession of the polarization of the metastable atoms under the influence of both the oscillating field  $H_1$  and the ambient magnetic field  $H_0$ , described by  $\mathcal{H}_M$ . The resulting density matrix differential equation is amenable to a steady state solution.

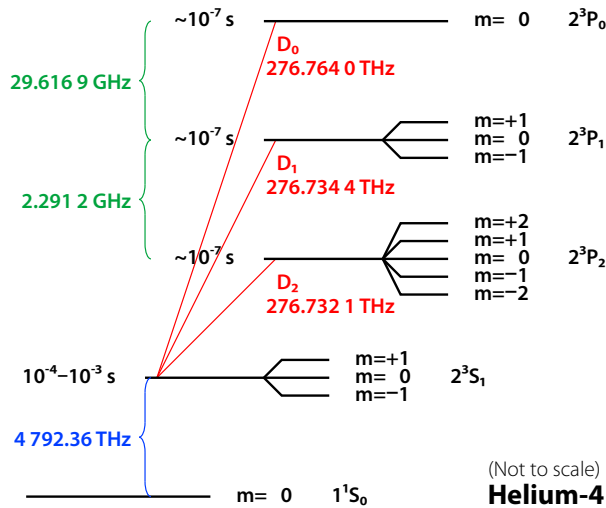


Figure 1.1. Relevant helium energy levels. Fine structure deltas come from [42, 29], and other frequencies come from [47]. Radiative transitions between  $2^3S_1$  and the ground state are strictly forbidden. (from [43], © 2010, American Physical Society)

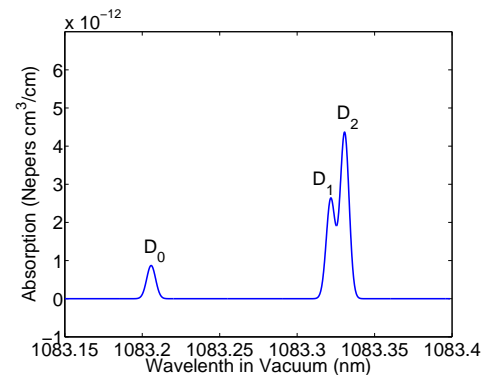


Figure 1.2. Helium Absorption Spectrum. Attenuation per unit length per metastable density.

The limited model presented by McGregor [34] assumed left-circularly polarized light propagating parallel to  $H_0$ , with the  $H_1$  coils perpendicular to this direction, and neglected the rank two spherical tensors in the expansion of the density matrix. Driven by current advances in instrument development, we have extended the evaluation of the Hamiltonian terms above to include the dispersive lineshape components, both rank one and two spherical tensors, arbitrary optical polarization and orientation of the pumping light with respect to  $H_0$ , and arbitrary orientation of the  $H_1$  field. Beyond the features described in [34], some of the additional effects that can be modeled as a direct result of these extensions include a quantitative treatment of the Bloch-Siegert shift and the virtual light shift, as well as a proper treatment of the magnetic resonance

curve in the “dead zones” assumed by prior theory, which are known experimentally to typically show non-zero signal amplitude.

This extended model is compared with the simpler model in [34] for laser pumping. Experimental results with linearly-polarized pumping light and experimental results with circularly-polarized pumping light are compared with the model, basing the calculations on our best experimental knowledge of the operating conditions. Subsequently, fits to the data for linearly-polarized light are also presented.

## CHAPTER 2

### BACKGROUND<sup>2</sup>

#### 2.1 Optical Pumping and Optically Pumped Magnetometers

One of the seminal works on magnetic resonance is that of Bloch [7], which gave phenomenological equations generally applicable to a variety of media. An outline of the methods involved in the use of rotating coordinate systems was presented in [46]. The transformation to a rotating coordinate system, while itself exact, is nearly always followed in theoretical magnetic resonance work by the approximation of neglecting the counter-rotating components of the circular decomposition of a linearly-oscillating field. This approximation results in an apparent shift in the magnetic resonance. An estimate of this Bloch-Siegert shift incurred for a two-level system is given in [8]. While nothing prevents the experimental use of a rotating field, experiments nearly always use an oscillating field in its place [48, 58], allowing the use of half as many coils. The Bloch-Siegert shift is of practical concern in weak fields under  $1 \mu\text{T}$ , as found in the fly-by calibration of the Cassini spacecraft [62]. We note that  $^4\text{He}$  has traditionally been the medium of choice for optically pumped magnetometers in space applications [11]. An accessible introduction to magnetic resonance and many associated effects can be found in [58].

One of the earliest papers describing the changes in optical properties of a medium as a function of ambient and rotating magnetic fields was [6], which describes alkali atoms, but neglects the nuclear moment. Kastler credited<sup>3</sup> this paper as the motivation for the development of optical pumping, a technique used to substantially increase the typically small thermal population difference in electron sublevels. Changes in the polarization or intensity of the scattered or transmitted light leaving the sample may be used to monitor the ensemble atomic polarization.

---

<sup>2</sup>A significant portion of the text of this chapter is based on [43], © 2010 American Physical Society.

<sup>3</sup>It was first proposed in a *Comptes Rendus de l'Académie des sciences* paper in 1949, which Kastler coauthored, and was carried out experimentally in [10].

The first experimental demonstration of simultaneous optical and magnetic<sup>4</sup> excitation, known as double-resonance optical pumping, used the mercury vapor  $6^3P_1$  state [10]. A review of experimental results for pumping mercury and alkali vapors is presented in [26], along with an examination of two opposing effects of foreign gases on the orientation. Data was given for contamination by  $^1H$  and  $^2H$ , and for intermodulation products observed when excited with two  $H_1$  frequencies.

Optical pumping of metastable  $^4He$  was first reported in [16]. Relative sublevel population as a function of the direction of pumping radiation was given, as were linewidths in inhomogeneous fields. Shortly thereafter, Franken and Colegrove also published a longer paper [13], giving equations that allow calculation of  $2^3S_1$  population distribution (assuming complete mixing, although this also applies to selective  $D_0$  excitation, described in Section 3.2), and giving a table of relative absorption probabilities and spontaneous emission probabilities. They proceeded to derive an angular correction to their rate equation solution. The approach is a bit simplistic, though perhaps justifiable when using unpolarized light. The lifetime of the metastables was measured and loss of polarization due to impurities was addressed. Inversion of the resonance line was then discussed, a matter of interest primarily when all 3 lines are pumped, as in a lamp. Finally, they suggested the device can be used to build a magnetometer.

At about the same time that Franken and Colegrove first demonstrated optical pumping of  $^4He$ , Skillman and Bender [57] used  $^{85}Rb$  and  $^{87}Rb$  to demonstrate one of the first optically-pumped magnetometers. Shortly thereafter, Keyser, et al. [28] built the first helium magnetometer. This magnetometer used transmission monitoring and yielded experimental recordings from “magnetic storms.”

The Larmor frequency may be shifted as a function of light intensity, wavelength, metastable density, and ambient field strength, and experimental measurements of these shifts have been made in  $2^3S_1$  metastable helium [50]. The shifts were measured by reversing the handedness of the circular polarization of the pumping light. Often considered is the concept of a virtual light shift,

---

<sup>4</sup>Some of the non- $^4He$  literature confusingly refers to the magnetic  $H_1$  excitation as “RF.” However, we reserve the term “RF” for the electrostatic stimulus used to generate and maintain the weak plasma discharge that replenishes the metastable  $^4He$   $2^3S_1$  state. Atomic species pumped in the ground state do not suffer this confusion.

which appears as an additive output on top of the desired magnetic field [27]. This virtual light shift is proportional to the product of the intensity of the pumping beam and a dispersive function of wavelength about each optical line center.

In [27], Kastler also demonstrated how to measure longitudinal ( $T_1$ ) and transverse ( $T_2$ ) lifetimes, and broke  $1/T_2$  into two real and two imaginary contributions, including the effects of light broadening, real light shifts, and virtual light shifts. Kastler identified the energy shift of the levels with a change in the velocity of the light, a dispersive effect. A general classification scheme for light shifts is presented in [22], framing the situation as a Hamiltonian perturbed by a light shift operator, one component of which corresponds to this virtual light shift.

Helium magnetometers had typically been pumped using a helium lamp as the light source. A solid-state laser in the vicinity of 1050–1080 nm was then reported in [49], and several solid state lasers around these wavelengths were discussed in [54]. More recently, following theoretical work by McGregor [34], laser pumped helium magnetometers have used tunable diode lasers operating at 1083 nm [12, 19, 61, 60].

An alternate approach to optical pumping, Optically-driven Spin-Precession (OSP), modulates the light intensity at the Larmor frequency, instead of using  $H_1$  magnetic modulation [5], and a recent review of applications in  $^4\text{He}$  is presented in [19]. While this document is concerned with  $^4\text{He}$ , it is important to point out that the optical pumping of  $^3\text{He}$  has also been observed in [59], and a magnetometer was constructed using  $^3\text{He}$ .

The most important application of optically-pumped  $^4\text{He}$  magnetometers is MAD (magnetic anomaly detection), used to detect submarines, and primarily taking the form of a magnetometer towed behind a propeller plane. The heart of the instrument is one or more  $^4\text{He}$  cells, although  $^3\text{He}$  is used in stationary applications, such as seafloor arrays. Other applications of the  $^4\text{He}$  system, or variations thereof, include detection of mines (land and sea) and measurement of planetary magnetic fields [44].

There are quite a few papers on geomagnetic noise (noise associated with random currents in the ionosphere, driven by Earth's magnetic field) available, and, while geomagnetic noise is a signal-processing problem and therefore outside the scope of this document, these papers are of

some general interest, since geomagnetic noise is one of the more serious limitations of any actual magnetometer system. One example of a paper describing a new method of rejecting this noise using a long baseline gradiometer is [18], which also gives a qualitative description of the spatial coherence of this noise.

Generally, literature that examines magnetic resonance theory uses an empirically-driven, heuristic rate equation approach, with treatments and results directed to specific physical effects prevalent in the apparatus. One exception is Happer [21], which thoroughly reviews optical pumping and monitoring of various atoms, but does not discuss magnetometers and does not address the use of lasers in optical pumping. While the various rate-equation based literature is useful and elucidating, a comprehensive treatment of this instrument can also give a valuable perspective. The other exception is that prior theory of a somewhat general nature for circularly-polarized pumping beams with additional restrictions can be found in McGregor [34]. Reference [34] not only addresses the magnetic resonance control loop of a magnetometer, but also gives quantitative data on expected sensitivities.

Some published effort has been devoted to alternative  $^4\text{He}$  configurations not considered in [34], such as the use of OSP in [19], and the use of linearly-polarized pumping light in [20]. Very little literature on magnetometers seems to address noise sources, but [34] at least discusses photodiode shot noise as a limiting factor. Reference [34] introduces a sufficient amount of material from magnetometer-related topics to make extensions directly applicable to existing systems, rather than simply applying to a one-off experiment designed to measure some particular physical quantity. Reference [34] serves as one of many efforts that can benefit from comprehensive treatment of arbitrary orientations and optical polarizations in simulation. With goals such as this in mind, [34] henceforth serves as the guide for *ab initio* theoretical development, having provided good experimental agreement within the assumptions of the time. In this document, we take the same approach, but with fewer restrictions. The generalizations made here will become increasingly useful in the next few generations of magnetometers.

## 2.2 $^4\text{He}$ Magnetometer Concepts

Figure 2.1 is a block diagram of a generic double-resonance laser-pumped  $^4\text{He}$  magnetometer. The sensing element, pictured in Figure 2.2, is a cylindrical cell containing  $^4\text{He}$  at a few Torr. Copper bands around the cell introduce a weak electrodeless RF discharge that excites a small fraction of the helium into the  $2^3\text{S}_1$  metastable state, shown in Figure 1.1. This excitation introduces unpolarized metastable atoms. Figure 1.2 shows that the  $\text{D}_0$  line is the best-resolved of the three. Laser light in the near IR (1083 nm) is isolated, attenuated, polarized, collimated, and directed into the cell, where it selectively excites the  $\text{D}_0$  transition, with a tendency to depopulate certain Zeeman states, depending on the optical polarization. The excited  $2^3\text{P}_0$  atoms spontaneously decay unpreferentially to each Zeeman sublevel of the metastable  $2^3\text{S}_1$  state. Thus the light establishes a longitudinal magnetic polarization of the gas. The transmitted laser light is monitored with an InGaAs or Si photodiode.

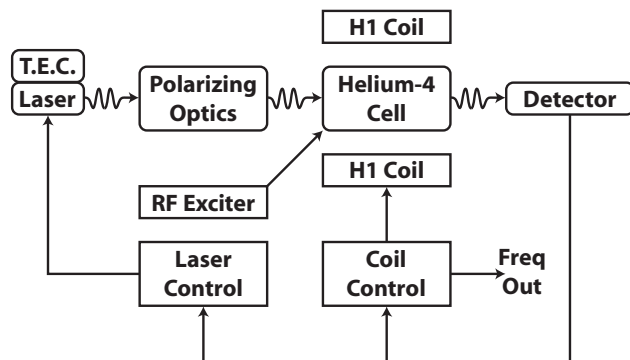


Figure 2.1. Representative block diagram of a double-resonance  $^4\text{He}$  magnetometer. (from [43], © 2010, American Physical Society)



Figure 2.2. Helium Cell in Operation.

A thermoelectric cooler (T.E.C.) either holds the temperature of the single-mode diode laser in a mode-hop-free operating region, or else actively compensates low-frequency coarse laser wavelength drift, depending on the system in question. Fine control of the laser wavelength is obtained by adjusting the center point of the laser current modulation, seeking to null the observed fundamental of the modulation on the photodiode.

In typical double-resonance, longitudinally-monitored magnetometers, small coils, absent from the photo to allow an unobstructed view, establish a weak oscillating magnetic field  $H_1$

across the cell, nominally directed perpendicularly to the ambient magnetic field  $H_0$ . The frequency  $\omega$  of the magnetic resonance coils is swept across the Larmor frequency  $\gamma H_0$ , where  $-\gamma \approx -28.025 \text{ Hz/nT}$  is the gyromagnetic ratio of metastable  $^4\text{He}$ . The true value of  $\gamma$  is known to nine significant figures [56], allowing an accurate absolute measurement of a scalar magnetic field  $H_0$ .

The monitored light is synchronously detected at the fundamental frequency of the FM-modulated  $H_1$  coils, and the center frequency of the modulation is adjusted until the fundamental vanishes from the detected output light, at which point the center frequency of the input modulation equals  $\gamma H_0$ , giving an absolute measurement of the ambient magnetic field. The frequency modulation of the  $H_1$  coils is slow enough to allow the atoms to respond, but must be fast enough to provide application-specific bandwidth. The use of modulation to operate away from baseband also reduces most sources of low-frequency noise originating in the electronics themselves. A typical experimental approach to determining the metastable density is to measure the percentage of light absorbed when either the magnetic resonance coils' frequency  $\omega$  is off-resonance or the coils are deactivated.

An example of a commercial  $^4\text{He}$  magnetometer is the Polatomic P-2000, which has a sensitivity of  $200 \text{ fT}/\sqrt{\text{Hz}}$  from DC–50 Hz, and this instrument is discussed, along with other optically-pumped magnetometers, in [11, 61, 60].

### 2.3 $^4\text{He}$ Considerations

Depending on which second-order effects are included, solutions of hydrogen are available in closed form. Since helium is the next-simplest atom, it has attracted significant theoretical attention, beginning at least in 1929<sup>5</sup>. For example, [40, 39] established variational wavefunctions and expectation values of operators of interest, refining and bounding past calculations. Oscillator strengths, which can be compared directly against the NIST spectral line database, were determined shortly thereafter in [55]. Many similar papers continue to appear to this day, including [15] in 2004, which attempts to choose a more physically-meaningful set of basis functions.

---

<sup>5</sup>Reference [15] only cites back to Hylleraas 1929, which is in German.

Reference [9] gives a qualitative description of relativistic emission routes for the metastable  $2^3S_1$  state of helium. In [41], the lifetime of helium  $2^3S_1$ , as well as neon and argon metastables, was measured over a range of pressures at two temperatures by observing the exponential decay in absorption of light after a very brief spark. The lifetimes obtained are not directly applicable here, since they were measured with the discharge off and disagree with more relevant sources (presumably for that reason), but several fit parameters may be useful, such as diffusion coefficients and collision cross sections. Much later, [14] used variational calculations to give two-photon emission rates and a distribution of photon energies for the decay of metastable  $2^1S_0$  and  $2^3S_1$  helium, as well as some results on neon. He finds that the singlet level prefers to emit two photons of equal energy, while the triplet level never does; this seems like it might be an interesting way to determine the amount of the singlet level in the discharge, given a selective-enough wavelength filter.

Hughes, et al. [25] determined the  $g_J$  factor, which is proportional to the gyromagnetic ratio, for  $^4\text{He}$  in terms of that of  $^2S_{1/2}$  hydrogen. Scheerer and Sinclair [53] determined the gyromagnetic ratio by comparing the frequency of a  $^4\text{He}$  gradiometer using unpolarized lamp light with that of a proton free-precession magnetometer. Shifrin, et al. [56] determined the gyromagnetic ratio by comparing the frequency of a free induction decay signal from a  $^3\text{He}$  cell with the frequency of a cell containing a mixture of  $^4\text{He}$  and  $^{133}\text{Cs}$ , where the former is excited by spin-exchange with the latter.

Because the gyromagnetic ratio of the pumped  $2^3S_1$   $^4\text{He}$  metastable state is the highest of any relevant state used in an optically-pumped magnetometer,  $^4\text{He}$  magnetometers are relatively insensitive to the angular velocities experienced in field use. The lack of hyperfine structure in helium makes the energy levels fairly simple, as shown in Figure 1.1. Additionally, because the density of the metastable states to be pumped is a function of electronic RF excitation, rather than ambient temperature, helium magnetometers function over wide temperature ranges without the need for temperature stabilization of the atomic sample. Scalar  $^4\text{He}$  magnetometers operate over a very wide dynamic range, with one typical case being 25 000–75 000 nT, which is bounded primarily by electronics constraints, rather than the basic physics. The physical lower bound is on the order of the magnetic resonance linewidth (about 100 nT). The Larmor frequency is linearly

related to the ambient magnetic field strength by the well-known gyromagnetic ratio, providing a simple absolute measurement.

An essential feature is the existence of a metastable  $2^3S_1$  state in the helium atom that cannot decay radiatively to the true ground state, but does eventually decay to the ground state primarily by diffusion to the cell wall at pressures of interest, but atom-atom collisions dominate in other regimes. The lifetime of the  $2^3S_1$  state is given as 0.1–1 ms in [13], who assume the discharge is on, in contrast to [41], who give 1–10 ms with the discharge off. Double-photon emission does not contribute noticeably to the lifetime, having an Einstein A coefficient  $\sim 10^{-9} \text{ sec}^{-1}$ , from [14]. The metastable state is populated by a weak electrodeless RF discharge [13], which leads to a variety of discrete spectral lines, some of which are visible as a glow, shown in Figure 2.2.

Metastable  $^4\text{He}$  is particularly robust against loss of coherence in atom-atom collisions because the  $2^3S_1$  state has no hyperfine structure and therefore only has one gyromagnetic ratio, while the ground state  $1^1S_0$  is a singlet and possesses neither Zeeman splitting nor hyperfine structure. Collisions between  $2^3P_0$  and other species do not matter, since the lack of any Zeeman splitting causes no shifts, and collisions between any two  $2^3P_J$  atoms or a  $2^3P_J$  atom and a  $2^3S_1$  atom are infinitesimally unlikely. Thus no particular restrictions need be made on the magnetometer design to accommodate collisions.

However, the light itself can still affect coherence, at least in a lamp-pumped system. Real light shifts [21, 27], where coherence is maintained through a transition from  $2^3S_1$  to  $2^3P_1$  or  $2^3P_2$  if a mixing collision does not occur, can be a concern when  $^4\text{He}$  is lamp-pumped. At higher pressures, collisions occur more frequently, causing decoherence to dominate shifts. In this regard, the high-pressure case resembles what one obtains by selectively pumping only the  $D_0$  line.

The collision-induced mixing cross section of the excited states of helium was determined in [51] by measuring the relative intensities of the spectral lines as a function of pressure, and fitting to a form predicted by some rate equations. A new estimate of this cross section, along with a lifetime for the excited states, was determined in [52] by using a more granular rate equation model including populations for all the Zeeman states to fit to the difference in polarization of scattered light. Landman [30] obtained another estimate of the lifetimes of the excited states, along with cross sections for collisions with ground state atoms. He showed that the alignment depolarization

cross section for the excited states is approximately explained by ground state collisions, but lumps  $J = 0, 1, 2$  together (which may be justified). Only laser pumping is considered here, so the real light shifts (and, by extension, collisional mixing) are not a concern.

Since the relaxation time  $\tau_c$  of  $^4\text{He}$  is relatively short, the longitudinal polarization responds quickly to magnetic field transients. This, combined with the very low sensitivity to rotations, has led to applications on dynamic platforms, such as airplanes. It is therefore desirable to characterize the operation of the magnetometer over all orientations.

Circularly-polarized light is commonly used to pump the helium, since the signal strength falls off approximately as the square of the cosine of the angle between the light beam and the ambient  $H_0$  field [23]. Adding the signals from three orthogonal cells yields approximately isotropic sensitivity, in spite of the highly-dynamic towed environment. However, this arrangement is approximate because the optical absorption changes with orientation, and because it is experimentally known that there is a small resonance curve visible even in the theoretically-predicted dead zone. The model we introduce remedies this theoretical gap by demonstrating the transition from the ordinary Lorentzian magnetic resonance lineshape to the double-trough curve more characteristic of pumping with linearly polarized light. The rigorous evaluation of the effects of orientation enables rapid evaluation of design ideas.

The laser wavelength is actively locked to a particular absorption line. However, use of circularly polarized light introduces errors associated with the virtual light shift: any wavelength detuning introduces a deviation in the measurement indistinguishable from a small change in the ambient magnetic field. When the laser noise is close to either the FM rate applied to the  $H_1$  coils or to DC, it appears in the low-frequency output band where magnetic signals are usually measured. Therefore, the wavelength noise of the laser and any wavelength modulation used to actively lock the laser to the center of the absorption line both contribute nontrivially to the noise floor of the magnetometer.

We have extended the theory to include these virtual light shifts. One can reduce these noises by the using two sets of cells, either adding the outputs of cells with opposite circular polarization, or subtracting the outputs of cells with like polarization. The latter, a gradiometer

[17], yields an asymptotically more rapid roll-off of signal, inversely proportional to the fourth power of range instead of the third, but with the benefit of eliminating most geomagnetic noise.

Pumping with linearly polarized light avoids virtual light shifts, and greatly reduces the magnetometer noise floor, but at the expense of more complicated arrangements of cells in order to achieve isotropic sensitivity. This, together with analysis of the importance of imperfect polarizer and waveplate alignment, motivates the extension of the theory to arbitrary optical polarization. Moreover, it will be shown that a nonintuitive choice of orientation of the  $H_1$  coils in the case of linearly-polarized pumping light reduces the overall variability of shot-noise sensitivity of the magnetometer over orientation.

Finally, the broad dynamic range required in space applications includes low  $H_0$  fields, where the Bloch-Siegert shift cannot be ignored. Therefore, we have accounted for this shift in the theory developed herein.

CHAPTER 3  
DERIVATIONS

Section 3.1 extends the first few equations of [34] to arbitrary quasistatic polarized light in an arbitrary direction. Sections 3.2, 3.3, 3.4, 3.5, and 3.6 fill in missing steps in [34]. Section 3.7 extends [34] to include all quadrupole terms with all optical polarizations and orientations. Section 3.8 extends [34] to include the rank-two components of the density matrix, under the action of magnetic fields, and details the approximation required to make the equations tractable. Section 3.9 fills in details in [34], as well as some details from private communication regarding the Doppler-broadened dispersive lineshape. Section 3.10 adds terms from all previous sections in a digestible state-space form and completes the transformation to a rotating coordinate system, in preparation for solution. Section 3.11 presents the details and some results of the cell slicing approach briefly mentioned in [34] for handling longitudinal parameter variation.

3.1 Electric Field of Light

Table 3.1. Symbols Introduced In Section 3.1

Symbol	Units	Description
$\vec{\mathbf{E}}(t)$	statvolt/cm	time-varying electric field due to pumping/monitoring light
$t$	sec	time
$E_0$	statvolt/cm	amplitude of electric field of light
$\vec{\mathbf{e}}$	—	3D Jones vector
$\omega'$	rad/s	frequency of light
$\hat{\mathbf{z}}$	—	direction of light propagation
$\hat{\mathbf{x}}$	—	azimuth of polarization (see text for circular case)
$\hat{\mathbf{y}}$	—	completes RHS of $\hat{\mathbf{x}}, \hat{\mathbf{y}}, \hat{\mathbf{z}}$
$\hat{\mathbf{Z}}$	—	direction of quasistatic magnetic field $H_0$
$\hat{\mathbf{X}}, \hat{\mathbf{Y}}$	—	arbitrary world directions $\perp \hat{\mathbf{Z}}$ , RHS
$\theta, \phi$	rad	see Figure 3.1
$\epsilon$	rad	ellipticity angle of light polarization

This section is intended to extend the first few equations of [34] to arbitrary quasistatic polarized light in an arbitrary direction.

A time-varying field at a point can be represented by [34]:

$$\vec{\mathbf{E}}(t) = \frac{1}{2}E_0\vec{\mathbf{e}}e^{-i\omega't} + \frac{1}{2}E_0\vec{\mathbf{e}}^*e^{i\omega't} \quad (3.1)$$

See Appendix A for details on the electric dipole approximation, which allows us to neglect the spatial dependence of the field.  $\vec{\mathbf{e}}$  is a Jones vector, e.g.,  $\frac{1}{\sqrt{2}}(\hat{\mathbf{X}} + i\hat{\mathbf{Y}})$  gives left circularly polarized light, LCP, propagating in the  $\hat{\mathbf{Z}}$  direction. In general, the polarization with respect to the cell is fixed, but the orientation of the cell with respect to the world is not.

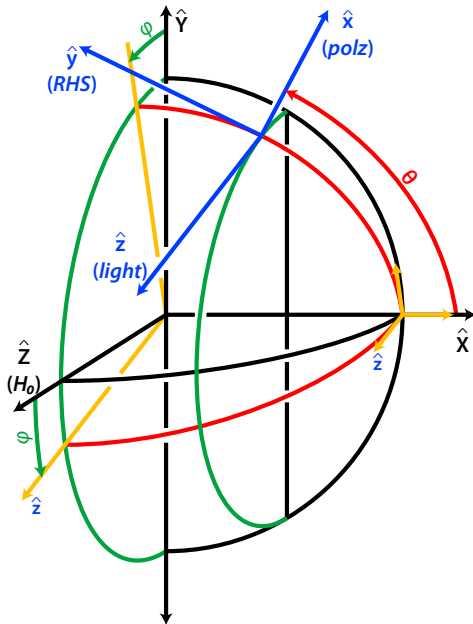


Figure 3.1. Local and World Coordinate Systems. (from [43], © 2010, American Physical Society)

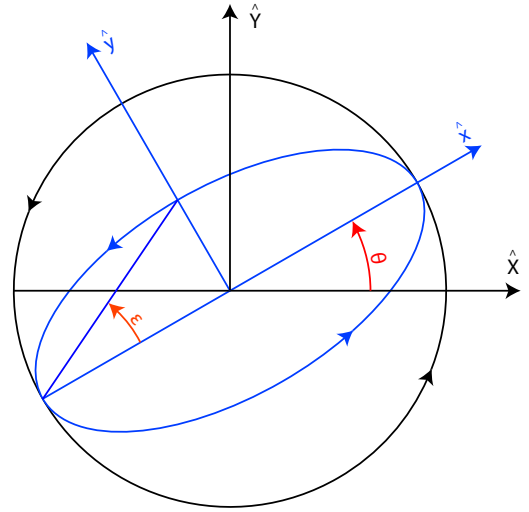


Figure 3.2. 2-D Polarization.

Now the Zeeman effect due to  $H_0$  splits energy levels having the same total angular momentum and orbital angular momentum according to total magnetic quantum number, so degenerate perturbation theory dictates that the coordinate system we work in must be oriented with the  $\hat{\mathbf{Z}}$  axis along  $H_0$  so that the Zeeman perturbation is diagonal in that basis. Therefore, there is an effective rotation of the other components of the problem. It makes sense to define a local coordinate system

by the light parameters (polarization and propagation directions), and a world coordinate system by the direction of  $H_0$ , and then work in the world system, as shown in Figure 3.1.

Note that the directions of  $\hat{\mathbf{X}}$  and  $\hat{\mathbf{Y}}$  must be chosen, but do not matter too much, provided they form a right-handed set. In the case of circularly-polarized light, we have the same indeterminacy with  $\hat{\mathbf{x}}$  and  $\hat{\mathbf{y}}$ , where it does not make sense to ask for the azimuth of polarization, but it will be shown not to matter anyway.

Now if the Jones vector in the local system is given by  $[\cos \epsilon \ -i \sin \epsilon \ 0]^T$  [4], it is shown in Appendix B.1 that the 3D Jones vector in the world system is given by:

$$\vec{\mathbf{e}} = \begin{bmatrix} \cos \epsilon \cos \theta & + i \sin \epsilon \sin \theta \\ \cos \epsilon \sin \theta \cos \phi - i \sin \epsilon \cos \theta \cos \phi \\ \cos \epsilon \sin \theta \sin \phi - i \sin \epsilon \cos \theta \sin \phi \end{bmatrix} \quad (3.2)$$

The ellipticity angle  $\epsilon \in \left[-\frac{\pi}{4}, \frac{\pi}{4}\right]$  identifies how linear or circular the light is, with, e.g.,  $\epsilon = 0$  representing linearly-polarized light along the  $\hat{\mathbf{x}}$  axis and  $\epsilon = -\frac{\pi}{4}$  representing LCP light [4]. If we took  $\phi = 0$ , left-elliptically polarized light would look like Figure 3.2, looking into the beam (i.e., looking in the  $-\hat{\mathbf{z}}$  direction). Figure 3.2 is based loosely on a figure in [4].

This can be rewritten in terms of the direction cosines, in order to eliminate the  $\theta, \phi$  nomenclature:

$$\vec{\mathbf{e}} = \begin{bmatrix} \frac{(\hat{\mathbf{y}} \cdot \hat{\mathbf{z}}) \cos \epsilon + i (\hat{\mathbf{x}} \cdot \hat{\mathbf{z}}) \sin \epsilon}{\sqrt{1 - (\hat{\mathbf{z}} \cdot \hat{\mathbf{z}})^2}} \\ (\hat{\mathbf{z}} \cdot \hat{\mathbf{z}}) \frac{(\hat{\mathbf{x}} \cdot \hat{\mathbf{z}}) \cos \epsilon - i (\hat{\mathbf{y}} \cdot \hat{\mathbf{z}}) \sin \epsilon}{\sqrt{1 - (\hat{\mathbf{z}} \cdot \hat{\mathbf{z}})^2}} \\ (\hat{\mathbf{x}} \cdot \hat{\mathbf{z}}) \cos \epsilon - i (\hat{\mathbf{y}} \cdot \hat{\mathbf{z}}) \sin \epsilon \end{bmatrix} \quad (3.3)$$

## 3.2 Excitation and Deexcitation

Table 3.2. Symbols Introduced In Section 3.2

Symbol	Units	Description
$\mathcal{H}$	erg	Total Hamiltonian of ${}^4\text{He}$ during operation
$\mathcal{H}_0$	erg	Unperturbed Hamiltonian of ${}^4\text{He}$ , including fine structure
$\mathcal{H}_L$	erg	Perturbation due to pumping/monitoring light
$\mathcal{H}_M$	erg	Perturbation due to $H_0$ and $H_1$ fields
$\mathcal{H}_R$	erg	Phenomenological relaxation perturbation
$\vec{\mathbf{D}}$	statcoulomb · cm	Electric dipole operator
$\vec{\mathbf{R}}$	cm	Position operator in world coordinates, length $R$
$\mu$	—	$2^3\text{S}_1$ metastable sublevel index, total $J_z$ quantum number
$m$	—	$2^3\text{P}_j$ magnetic sublevel index, total $J_z$ quantum number
$E_m, E_\mu$	erg	Energies of $m$ and $\mu$ levels, respectively (averaged, if necessary)
$\rho$	—	Density operator
$\omega'_0$	rad/s	Mean transition frequency of any of the three absorption lines at zero atomic velocity
$\tau$	sec	Relaxation rate governing natural and collisional linewidths

This section merely fills in many missing steps in [34].

The helium atom's dynamics can be described by [34]:

$$\mathcal{H} = \mathcal{H}_0 + \mathcal{H}_L + \mathcal{H}_R + \mathcal{H}_M \quad (3.4)$$

Note that [34] does not explicitly list  $\mathcal{H}_M$ .  $\mathcal{H}_L$  is derived in Appendix A, where  $\vec{\mathbf{D}} \equiv q\vec{\mathbf{R}}$ :

$$\mathcal{H}_L = -\vec{\mathbf{E}}(t) \cdot \vec{\mathbf{D}} \quad (3.5)$$

The standard equation for time evolution of the density operator is [48]:

$$i\hbar \frac{d\rho}{dt} = [\mathcal{H}, \rho] \quad (3.6)$$

We can partition  $\rho$  according to total orbital angular momentum:

$$\rho \doteq \begin{bmatrix} \langle \mu | \rho | \mu' \rangle & \langle \mu | \rho | m' \rangle \\ \langle m | \rho | \mu' \rangle & \langle m | \rho | m' \rangle \end{bmatrix} \equiv \begin{bmatrix} \rho_{\mu\mu'} & \rho_{\mu m'} \\ \rho_{m\mu'} & \rho_{mm'} \end{bmatrix} \quad (3.7)$$

where  $\doteq$  denotes “is represented by,” when moving, for example, from an operator to a matrix in a particular basis.

This allows us to represent just the portion of Equation (3.6) related to excitation and de-excitation:

$$\begin{aligned} i\hbar \frac{d\rho_{m\mu}}{dt} &= [\mathcal{H}, \rho]_{m\mu} = \langle m | \mathcal{H} \rho | \mu \rangle - \langle m | \rho \mathcal{H} | \mu \rangle \\ &= \sum_{m'} \left[ \underbrace{\langle m | \mathcal{H} | m' \rangle}_{\text{A}} \rho_{m'\mu} - \underbrace{\rho_{mm'} \langle m' | \mathcal{H} | \mu \rangle}_{\text{B}} \right] + \sum_{\mu'} \left[ \underbrace{\langle m | \mathcal{H} | \mu' \rangle}_{\text{C}} \rho_{\mu'\mu} - \underbrace{\rho_{m\mu'} \langle \mu' | \mathcal{H} | \mu \rangle}_{\text{D}} \right] \end{aligned} \quad (3.8)$$

The on-diagonal terms of  $\rho_{mm'}$  represent the population of  $2^3P_J$  states, which is small, given the short lifetime of about 100 ns [30]. For the  $2^3P_0$  state (the highest state in Figure 1.1), corresponding to the  $D_0$  line, the single on-diagonal term is the only component of  $\rho_{mm'}$ , so  $\rho_{mm'}$  (and therefore term B) can be neglected whenever we only allow  $\omega'$  near  $D_0$ . This is realistic with the current systems, which are excited by lasers, rather than lamps. Keeping term B would have allowed us to account for “repopulation pumping” and “real light shifts,” which are not an issue with the  $D_0$  line, as mentioned. This is not to be confused with “virtual light shifts” [27, 50, 53], which *will* be accounted for.

Repopulation pumping arises when the some amount of the atoms’ polarization is maintained through a transition through  $2^3P_J$  states. To occur, there must be more than one Zeeman sublevel (i.e., for  $2J + 1$  of 3 or 5) and the atom must not undergo a “mixing collision.” When a  $2^3P_J$  excited atom collides with a ground-state atom, the Zeeman sublevels, and, to a certain extent, the different  $J$  fine-structure levels, get redistributed more or less evenly, particularly at higher gas pressures, destroying any polarization [51]. Reference [13] indicates complete mixing is achieved above a few torr, but many of the  $^4\text{He}$  cells are charged to about 1.5 torr.

Since the excited  $2^3P_J$  states have nonzero orbital angular momentum, they have a lower gyromagnetic ratio, and the expectation value of the polarization precesses more slowly than the  $2^3S_1$  state would in the same  $H_0$  field, giving what is called a “real light shift.” Therefore, when those states return to the  $2^3S_1$  level, assuming they have not collided in the meantime, the metastable atoms’ polarizations are now “out of step,” and, on average, they have precessed less [53]. As expected from a calculation of the Landé g-factor,  $2^3P_1$  and  $2^3P_2$  have roughly equal gyromagnetic ratios [30].

Since the  $2^3P_0$  state has only one Zeeman sublevel, it does not maintain any polarization information, and it does not precess (the excited density “matrix” is scalar). Even if the  $2^3P_0$  states are mixed into  $2^3P_1$  or  $2^3P_2$  by collisions, polarization information has already been lost before the collision, so mixing collisions do not change the fact that real light shifts and repopulation pumping do not occur for selective  $D_0$  pumping. Since the spontaneous emission from a particular ensemble-unpolarized level (e.g.,  $2^3P_1$ ) does not preferentially populate any particular  $2^3S_1$  state, a mixing collision makes little difference<sup>6</sup> in the relaxation effect on selective pumping of  $D_0$ .

Now  $\mathcal{H}_0$  is completely diagonal, so only terms A and D survive on the RHS when it is applied:

$$\left(i\hbar\frac{d\rho_{m\mu}}{dt}\right)_0 = \langle m|\mathcal{H}_0|m\rangle\rho_{m\mu} - \rho_{m\mu}\langle\mu|\mathcal{H}_0|\mu\rangle = \rho_{m\mu}(E_m - E_\mu) = \hbar\omega'_0\rho_{m\mu}$$

$\mathcal{H}_L$  is induced by the very rapid oscillation of the light’s electric field, and therefore only acts between the widely-spaced levels  $m$  and  $\mu$ . This means that only terms B and C survive, and we’ve already discarded B:

$$\left(i\hbar\frac{d\rho_{m\mu}}{dt}\right)_L = \sum_{\mu'}\langle m|\mathcal{H}_L|\mu'\rangle\rho_{\mu'\mu} = -\sum_{\mu'}\langle m|\vec{\mathbf{E}}(t)\cdot\vec{\mathbf{D}}|\mu'\rangle\rho_{\mu'\mu}$$

On the other hand,  $\mathcal{H}_M$  is induced by the slower  $H_1$  field, and therefore only mixes the Zeeman sublevels with one another. It can be argued that  $\rho_{m\mu}$  represents transitions between the  $m$  and  $\mu$  states, and so cannot be affected by  $\mathcal{H}_M$ .  $\mathcal{H}_M$  does affect  $\rho_{\mu\mu'}$ , a fact we will make use of in Section 3.4.

Finally, we consider  $\mathcal{H}_R$ , the phenomenological relaxation term intended to give the natural linewidth. It is a common trick in quantum mechanics to take an imaginary (i.e., skew-Hermitian) Hamiltonian when nonconservation of probability is desired. In this case, the desired result is loss of electrons from the  $2^3P_J$  states, since the time constant for loss from the  $2^3S_1$  metastable state is so much longer, and therefore negligible. Therefore,  $\mathcal{H}_R$  has the  $2^3P_J$  states as eigenvalues:

$$\mathcal{H}_R|m\rangle = \frac{-i\hbar}{\tau}|m\rangle$$

---

<sup>6</sup>It is thought that reabsorption of light may be affected by mixing at higher pressures, but that will not be examined here.

where constants are inserted in order to make the linewidth come out correctly (recall this term is phenomenological).

In LS coupling, transitions of type E1, M1, and E2 obey the selection rule  $\Delta S = 0$ , which prohibits  $2^3S_1$  and  $2^3P_J$  levels from decaying to the  $1^1S_0$  ground state [32]. One could also introduce a term of the opposite sign for the eigenvalue with respect to  $|\mu\rangle$ , to account for the corresponding *gain* in the  $2^3S_1$  state, but, again, this would just adjust the value of  $\tau$ , and we are already planning on adjusting it. Note that [9] qualitatively states that M1 radiation from the  $2^3S_1$  level is *possible*, but [14] states that its probability is negligible compared to two-photon emission. As mentioned previously, radiative decay from  $2^3S_1$  does not contribute significantly. Reference [14] also states that no other single-photon emission processes contribute at all, aside from M1. The existence of M1 radiation from the  $2^3S_1$  level implies that LS coupling does not strictly hold, but M1's *relative* unlikelihood clearly implies that LS coupling is still a very good approximation.

Doppler broadening, to be incorporated later (Section 3.9), dominates the resulting linewidth, so we needn't dwell too long on the details of  $\tau$ . Choosing to only keep the A term, or to keep both A and D, will not make a practical difference in the result, so the former is chosen:

$$\left( i\hbar \frac{d\rho_{m\mu}}{dt} \right)_R = \langle m | \mathcal{H}_R | m \rangle \rho_{m\mu} = \frac{-i\hbar}{\tau} \rho_{m\mu}$$

Combining, and using Equation (3.1), we obtain:

$$i\hbar \frac{d\rho_{m\mu}}{dt} = \hbar\omega'_0 \rho_{m\mu} - \frac{E_0}{2} \sum_{\mu'} \left[ \langle m | \vec{e} \cdot \vec{D} | \mu' \rangle \rho_{\mu'\mu} e^{-i\omega't} + \langle m | \vec{e}^* \cdot \vec{D} | \mu' \rangle \rho_{\mu'\mu} e^{i\omega't} \right] - \frac{i\hbar}{\tau} \rho_{m\mu} \quad (3.9)$$

Now  $\rho_{\mu'\mu}$  represents either populations of the  $2^3S_1$  metastable states, or oscillations within that state. The populations are quasistatic values under steady-state operation, and populations are quite generally nonnegative. Oscillations within the state can only be induced by the appropriate frequency, namely, the frequency of the  $H_1$  coils.  $\rho_{m\mu}$  is clearly driven by an  $e^{-i\omega'_0 t}$  from the first term ( $\mathcal{H}_0$ ), and by  $e^{\pm i\omega't}$  from the bracketed terms ( $\mathcal{H}_L$ ). Both  $\omega'_0$  and  $\omega'$  are over eight orders of magnitude larger than the oscillation frequency of the  $H_1$  coils on Earth<sup>7</sup>. As such,  $\rho_{\mu'\mu}$  can be treated as a constant *while solving* this differential equation.

<sup>7</sup>Even using JPL estimates for ambient magnetic field for a proposed mission to Jupiter, the ratio is thought to be almost seven orders of magnitude, so this approximation is valid over all reasonable applications of the magnetometer system.

The solution must be of the form:

$$\boldsymbol{\rho}_{m\mu}(t) = \mathbf{a}e^{-i\omega'_0 t} + \mathbf{b}e^{-i\omega' t} + \mathbf{c}e^{i\omega' t} \quad (3.10)$$

where the choice of  $\omega'_0$  depends on which values of  $m$  we are considering, and so can be considered a single value for the purposes of solution.

Substituting and simplifying, we obtain  $\mathbf{a} = 0$  and:

$$\mathbf{b} = \frac{\tau}{-i + \tau(\omega'_0 - \omega')} \frac{E_0}{2\hbar} \sum_{\mu'} \langle m | \vec{\mathbf{e}} \cdot \vec{\mathbf{D}} | \mu' \rangle \boldsymbol{\rho}_{\mu'\mu}$$

$$\mathbf{c} = \frac{\tau}{-i + \tau(\omega'_0 + \omega')} \frac{E_0}{2\hbar} \sum_{\mu'} \langle m | \vec{\mathbf{e}}^* \cdot \vec{\mathbf{D}} | \mu' \rangle \boldsymbol{\rho}_{\mu'\mu}$$

Let's just examine the first fraction in those results. The ratio of the magnitude-squared of the first to the magnitude-squared of the second is:

$$\frac{1 + \tau^2 (\omega'_0 + \omega')^2}{1 + \tau^2 (\omega'_0 - \omega')^2}$$

The numerator is always very large (probably about  $10^{17}$  if  $\tau \sim 10^{-7}$  s). The worst-case scenario in practical operation is for the laser to be tuned approximately to  $D_0$ , while finding the effect of  $D_2$ . This makes the worst case of  $(\omega' - \omega'_0)/2\pi$  approximately 32 GHz, which gives about  $10^8$  for the denominator. The ratio is largely independent of  $\tau$ . Therefore, at worst,  $|b| \sim 10^4 |c|$ , and  $\frac{|b|}{|c|}$  will usually be even larger than that, since we're usually not even interested in the other lines. As far as the guess for  $\tau$  goes, any  $\tau$  longer than about 1 ps will round to a ratio of  $10^4$  for our choice of 32 GHz. We neglect  $\mathbf{c}$  and write the approximate solution:

$$\boldsymbol{\rho}_{m\mu}(t) = \frac{i\tau}{2\hbar} E_0 \sum_{\mu'} \langle m | \vec{\mathbf{e}} \cdot \vec{\mathbf{D}} | \mu' \rangle \boldsymbol{\rho}_{\mu'\mu} e^{-i\omega' t} f(\omega'), \quad f(\omega') \equiv \frac{1}{1 - i\tau(\omega' - \omega'_0)} \quad (3.11)$$

as shown in Equations (6)-(7) in [34].

### 3.3 Metastable Evolution With Light

This section also serves only to fill in missing steps in [34].

Much like we did with Equation (3.8), we can write:

$$\begin{aligned}
i\hbar \frac{d\rho_{\mu\mu'}}{dt} &= [\mathcal{H}, \rho]_{\mu\mu'} = \langle \mu | \mathcal{H} \rho | \mu' \rangle - \langle \mu | \rho \mathcal{H} | \mu' \rangle \\
&= \sum_m \left[ \underbrace{\langle \mu | \mathcal{H} | m \rangle \rho_{m\mu'}}_A - \underbrace{\rho_{\mu m} \langle m | \mathcal{H} | \mu' \rangle}_B \right] + \sum_{\mu''} \left[ \underbrace{\langle \mu | \mathcal{H} | \mu'' \rangle \rho_{\mu''\mu'}}_C - \underbrace{\rho_{\mu\mu''} \langle \mu'' | \mathcal{H} | \mu' \rangle}_D \right] \quad (3.12)
\end{aligned}$$

Now  $\mathcal{H}_0$  only acts between  $\mu$  and  $\mu'$  here, since it's diagonal, so we keep terms C and D. However, terms C and D cancel one another, and so we get no contribution from  $\mathcal{H}_0$  at all. Because  $\mathcal{H}_R$  behaves the same way, it also fails to contribute. We will treat  $\mathcal{H}_M$ 's contributions in Section 3.4.

$\mathcal{H}_L$  only keeps terms A and B, so we obtain:

$$\left( i\hbar \frac{d\rho_{\mu\mu'}}{dt} \right)_L = \sum_m \left[ \langle \mu | \mathcal{H}_L | m \rangle \rho_{m\mu'} - \rho_{\mu m} \langle m | \mathcal{H}_L | \mu' \rangle \right] \quad (3.13)$$

Substituting our solution from Equation (3.11), we obtain four terms:

$$\begin{aligned}
\frac{-4\hbar^2}{\tau E_0^2} \left( \frac{d\rho_{\mu\mu'}}{dt} \right)_L &= \sum_{m,\mu''} \langle \mu | \vec{\mathbf{e}} \cdot \vec{\mathbf{D}} | m \rangle \langle m | \vec{\mathbf{e}} \cdot \vec{\mathbf{D}} | \mu'' \rangle \rho_{\mu''\mu'} f(\omega') e^{-2i\omega' t} \\
&\quad + \sum_{m,\mu''} \langle \mu | \vec{\mathbf{e}}^* \cdot \vec{\mathbf{D}} | m \rangle \langle m | \vec{\mathbf{e}} \cdot \vec{\mathbf{D}} | \mu'' \rangle \rho_{\mu''\mu'} f(\omega') \\
&\quad + \sum_{m,\mu''} \rho_{\mu\mu''} \langle \mu'' | \vec{\mathbf{e}}^* \cdot \vec{\mathbf{D}} | m \rangle \langle m | \vec{\mathbf{e}} \cdot \vec{\mathbf{D}} | \mu' \rangle f^*(\omega') \\
&\quad + \sum_{m,\mu''} \rho_{\mu\mu''} \langle \mu'' | \vec{\mathbf{e}}^* \cdot \vec{\mathbf{D}} | m \rangle \langle m | \vec{\mathbf{e}}^* \cdot \vec{\mathbf{D}} | \mu' \rangle f^*(\omega') e^{2i\omega' t} \quad (3.14)
\end{aligned}$$

Now it should be obvious that the metastable densities are not changing at the second harmonic of 277 THz (or the fundamental, for that matter). It should also be apparent that light cannot cause the transition rates between the metastable sublevels to vary that fast, either. Indeed, this sort of assumption was already made, so not making it again here may lead to strange results.

Therefore, the solution is as given in [34]:

$$\begin{aligned}
&\left( \frac{d\rho_{\mu\mu'}}{dt} \right)_L \\
&= -\frac{\tau E_0^2}{4\hbar^2} \sum_{m,\mu''} \left[ \langle \mu | \vec{\mathbf{e}}^* \cdot \vec{\mathbf{D}} | m \rangle \langle m | \vec{\mathbf{e}} \cdot \vec{\mathbf{D}} | \mu'' \rangle \rho_{\mu''\mu'} f(\omega') + \rho_{\mu\mu''} \langle \mu'' | \vec{\mathbf{e}}^* \cdot \vec{\mathbf{D}} | m \rangle \langle m | \vec{\mathbf{e}} \cdot \vec{\mathbf{D}} | \mu' \rangle f^*(\omega') \right] \quad (3.15)
\end{aligned}$$

## 3.4 Metastable Evolution With Magnetic Field

Table 3.3. Symbols Introduced In Section 3.4

Symbol	Units	Description
$\vec{\mathbf{H}}(t)$	nT	Vector total magnetic field, including $H_0$ and $H_1$ , in world coordinates.
$\gamma$	rad/s·nT	$-2\pi \times$ the $2^3\text{S}_1$ gyromagnetic ratio (physical constant)
$\omega$	rad/s	Frequency of Helmholtz coils, $\sim \gamma H_0$
$\mathbf{J}$	erg · s	Angular momentum operator
$\rho$	—	Shorthand for $\rho_{\mu\mu'}$ in subsequent sections.

Similarly, this section fills in details of [34].

We know that [58]:

$$\mathcal{H}_M = \gamma \vec{\mathbf{H}} \cdot \vec{\mathbf{J}}, \quad (3.16)$$

where  $-\gamma/2\pi$  is the gyromagnetic ratio of metastable  $2^3\text{S}_1$  helium-4. We have chosen the value  $\gamma/2\pi \approx 28.025$  Hz/nT, which is exact for a free electron. Some authors show a slightly modified value of  $-\gamma/2\pi$  of about 28.0235–28.0238 Hz/nT [53, 56]. The corresponding value of the g-factor is found in [25].

Beginning from Equation (3.12), we now work with  $\mathcal{H}_M$ . Since  $\vec{\mathbf{J}}$  only mixes within the Zeeman sublevels, we can only keep terms C and D. The result is straightforward:

$$\left( \frac{d\rho_{\mu\mu'}}{dt} \right)_M = \frac{i\gamma}{\hbar} \sum_{\mu''} [\rho_{\mu\mu''} \langle \mu'' | \vec{\mathbf{H}} \cdot \vec{\mathbf{J}} | \mu' \rangle - \langle \mu | \vec{\mathbf{H}} \cdot \vec{\mathbf{J}} | \mu'' \rangle \rho_{\mu''\mu'}] \quad (3.17)$$

Notice that there are no longer any references to  $m$ . This equation, along with Equation (3.15), are the only density matrix equations we need [34], and neither references  $m$  in the subscript of the density matrix. Therefore, we will stop subscripting  $\rho$ . Of course, if we had kept  $\rho_{mm'}$ , we would not have that notational convenience.

## 3.5 Dipole Matrix Elements

Table 3.4. Symbols Introduced In Section 3.5

Symbol	Units	Description
$\hat{\mathbf{i}}_{\pm 1}, \hat{\mathbf{i}}_0$	—	unit vectors in world coordinates
$D_0$	statcoulomb · cm	physical constant, related to dipole moment
$S_{ik}$	statcoulomb · cm	line strengths, as defined by [47]
$\hat{\mathbf{R}}$	—	Normalized position operator in world coordinates
$X, Y, Z$	cm	Position operators in world coordinates
$T^{(k)}$	a.u. <sup>†</sup>	Spherical tensor of rank $k$
$T_{\xi}^{(k)}$	a.u. <sup>†</sup>	Spherical tensor of rank $k$ and magnetic quantum number $\xi$

<sup>†</sup>units are the same as those of  $D_0$  in this section, but are angular momentum units in later sections

This section fills in the origins of Table I of [34].

In this section alone, we will write  $|m\rangle$  and  $|\mu\rangle$  more explicitly as  $|j_m, m_m\rangle$  and  $|1, m_\mu\rangle$ . In other sections, we will continue to use the former notation, and, without the ket, we let  $m$  and  $\mu$  stand for the magnetic quantum number.

We wish to apply the Wigner-Eckart theorem, so it is desirable to expand the electric dipole (see Appendix A) operator  $\vec{\mathbf{D}} \equiv q\vec{\mathbf{R}}$  in terms of spherical tensors of rank one, given in [48] as:

$$T_0^{(1)} = \sqrt{\frac{3}{4\pi}} V_z \equiv q \frac{Z}{R} \quad T_{\pm 1}^{(1)} = \mp \sqrt{\frac{3}{4\pi}} \frac{V_x \pm iV_y}{\sqrt{2}} \equiv \mp q \frac{\frac{X}{R} \pm i\frac{Y}{R}}{\sqrt{2}}$$

where we've substituted a normalized form of the dipole operator for the generic vector operator  $\vec{\mathbf{V}}$ .

It is easily verified that

$$q\hat{\mathbf{R}} \equiv q \frac{\vec{\mathbf{R}}}{\|\vec{\mathbf{R}}\|} = \hat{\mathbf{i}}_0 T_0^{(1)} - \hat{\mathbf{i}}_{-1} T_1^{(1)} + \hat{\mathbf{i}}_1 T_{-1}^{(1)} \quad (3.18)$$

where we've defined [34]:

$$\hat{\mathbf{i}}_0 = \hat{\mathbf{Z}} \quad \hat{\mathbf{i}}_{\pm 1} = \frac{\hat{\mathbf{X}} \pm i\hat{\mathbf{Y}}}{\sqrt{2}}$$

The Wigner-Eckart theorem is given by:

$$\langle \alpha_m; j_m, m_m | T_\xi^{(1)} | \alpha_\mu; 1, m_\mu \rangle = \langle 1, 1; m_\mu, \xi | 1, 1; j_m, m_m \rangle \frac{\langle \alpha_m, j_m | T^{(1)} | \alpha_\mu, 1 \rangle}{\sqrt{3}} \quad (3.19)$$

where  $\xi$  is defined by its use in  $T_\xi^{(1)}$ , and the  $m$  and  $\mu$  subscripts denote the  $2^3P_J$  and  $2^3S_1$  quantum numbers.  $\alpha$  includes any non-angular quantum numbers, but our states are completely specified without it, so we will omit it. The double-bar matrix element will be determined by spectroscopic data in [47]. A table of Clebsch-Gordan coefficients can be found in [3]. Note that for the  $D_1$  line, the choice of  $\langle 1, 1; m_\mu, \xi |$  over  $\langle 1, 1; \xi, m_\mu |$  will cause a sign flip, but, quite generally, an absolute phase on all factors will be irrelevant to our later calculations for any given spectral line, as they will all eventually be multiplied by a complex conjugate, though possibly of a different state (i.e., different Zeeman  $m$  component) in the line.

In order to see how normalization will fit in, let us rearrange the Clebsch-Gordan tables. Note that the header rows/columns are not part of the matrices:

$$\begin{aligned} D_0 : \quad & \langle 1, 1; m_\mu, -m_\mu | 1, 1; 0, 0 \rangle = \frac{1}{\sqrt{3}} \left[ \begin{array}{c|ccc} & (m_\mu = 1) & (m_\mu = 0) & (m_\mu = -1) \\ (m_m = 0) & 1 & -1 & 1 \end{array} \right] \\ D_1 : \quad & \langle 1, 1; m_\mu, m_m - m_\mu | 1, 1; 1, m_m \rangle = \frac{1}{\sqrt{2}} \left[ \begin{array}{c|ccc} & (m_\mu = 1) & (m_\mu = 0) & (m_\mu = -1) \\ (m_m = 1) & 1 & -1 & 0 \\ (m_m = 0) & 1 & 0 & -1 \\ (m_m = -1) & 0 & 1 & -1 \end{array} \right] \\ D_2 : \quad & \langle 1, 1; m_\mu, m_m - m_\mu | 1, 1; 2, m_m \rangle = \frac{1}{\sqrt{6}} \left[ \begin{array}{c|ccc} & (m_\mu = 1) & (m_\mu = 0) & (m_\mu = -1) \\ (m_m = 2) & \sqrt{6} & 0 & 0 \\ (m_m = 1) & \sqrt{3} & \sqrt{3} & 0 \\ (m_m = 0) & 1 & 2 & 1 \\ (m_m = -1) & 0 & \sqrt{3} & \sqrt{3} \\ (m_m = -2) & 0 & 0 & \sqrt{6} \end{array} \right] \end{aligned}$$

The spectroscopic data [47] is written in terms of line strengths  $S_{ik}$ , as a sum over all 27 transitions, and  $S_{ik}$  is equal to the sum of the magnitude squared of Equation (3.19), so we now examine the sum of the squares of all the Clebsch-Gordan coefficients. Note that each of the nine rows has a sum-of-squares equal to unity. Because the multiplicity of the metastable states is 3 for all cases, we will not split that off. Reference [47] gives  $\sum_{i,k} S_{ik} = 57.66q^2a_B^2$ . Reference [47] also gives numbers for the multiplets (e.g.,  $D_1$ ), and, to one unit in the last place, the numbers are

consistent with a simple division by the multiplicity ( $2m_m + 1 = 1,3,5$ ). Therefore, dividing evenly among the 9  $2^3P_J$  states, we find that

$$\begin{aligned} (2.5311qa_B)^2 &= \sum_{m_\mu} \left| \langle j_m, m_m | T_\xi^{(1)} | 1, m_\mu \rangle \right|^2 = \frac{\left| \langle j_m | T^{(1)} | 1 \rangle \right|^2}{3} \sum_{m_\mu} \left| \langle 1, 1; m_\mu, \xi | 1, 1; j_m, m_m \rangle \right|^2 \\ &= \frac{\left| \langle j_m | T^{(1)} | 1 \rangle \right|^2}{3} \end{aligned}$$

in close agreement with the definition of  $D_0 = 2.5312qa_B$  in [34]. For the sake of consistency, we will assume the two definitions are equal. Note that, as assumed, this constant is independent of which multiplet  $j_m$  we examine.

For each element of the matrices, Equation (3.18) contributes at most one term, governed by the angular momentum addition rule that  $m_\mu + \xi = m_m$ . Substituting this constant, Equation (3.18), and the Clebsch-Gordan coefficient tables into Equation (3.19), we obtain the final tables, matching Reference [34], where the argument of  $\vec{\mathbf{D}}$  is redundant and could be dropped:

$$\begin{aligned} D_0 : \quad & \langle 0, 0 | \vec{\mathbf{D}}(-m_\mu) | 1, m_\mu \rangle = \frac{D_0}{\sqrt{3}} \left[ \begin{array}{c|ccc} & (m_\mu = 1) & (m_\mu = 0) & (m_\mu = -1) \\ (m_m = 0) & \mathbf{i}_1 & -\mathbf{i}_0 & -\mathbf{i}_{-1} \end{array} \right] \\ D_1 : \quad & \langle 1, m_m | \vec{\mathbf{D}}(m_m - m_\mu) | 1, m_\mu \rangle = \frac{D_0}{\sqrt{2}} \left[ \begin{array}{c|ccc} & (m_\mu = 1) & (m_\mu = 0) & (m_\mu = -1) \\ (m_m = 1) & \mathbf{i}_0 & \mathbf{i}_{-1} & 0 \\ (m_m = 0) & \mathbf{i}_1 & 0 & \mathbf{i}_{-1} \\ (m_m = -1) & 0 & \mathbf{i}_1 & -\mathbf{i}_0 \end{array} \right] \\ D_2 : \quad & \langle 2, m_m | \vec{\mathbf{D}}(m_m - m_\mu) | 1, m_\mu \rangle = \frac{D_0}{\sqrt{6}} \left[ \begin{array}{c|ccc} & (m_\mu = 1) & (m_\mu = 0) & (m_\mu = -1) \\ (m_m = 2) & -\sqrt{6}\mathbf{i}_{-1} & 0 & 0 \\ (m_m = 1) & \sqrt{3}\mathbf{i}_0 & -\sqrt{3}\mathbf{i}_{-1} & 0 \\ (m_m = 0) & \mathbf{i}_1 & 2\mathbf{i}_0 & -\mathbf{i}_{-1} \\ (m_m = -1) & 0 & \sqrt{3}\mathbf{i}_1 & \sqrt{3}\mathbf{i}_0 \\ (m_m = -2) & 0 & 0 & \sqrt{6}\mathbf{i}_1 \end{array} \right] \end{aligned} \quad (3.20)$$

### 3.6 Spherical Basis For Spin 1

This section fills in details omitted from [34].

Reference [48] gives the defining relations for spherical tensors as:

$$[\mathbf{J}_z, T_\xi^{(2)}] = \hbar \xi T_\xi^{(2)} \quad [\mathbf{J}_\pm, T_\xi^{(2)}] = \hbar \sqrt{(2 \mp \xi)(3 \pm \xi)} T_{\xi \pm 1}^{(2)}$$

$$[\mathbf{J}_z, \mathbf{T}_\xi^{(1)}] = \hbar \xi \mathbf{T}_\xi^{(1)} \quad [\mathbf{J}_\pm, \mathbf{T}_\xi^{(1)}] = \hbar \sqrt{(1 \mp \xi)(2 \pm \xi)} \mathbf{T}_{\xi \pm 1}^{(1)}$$

where  $|\xi| \leq k$  in  $\mathbf{T}_\xi^{(k)}$ . One can show that the following definitions are consistent with the given commutation relations, where the rows and columns are numbered in decreasing order of  $\mu$ :

$$\begin{aligned} \mathbf{T}_1^{(1)} = \frac{-\mathbf{J}_+}{2} &\doteq \frac{\hbar}{\sqrt{2}} \begin{bmatrix} 0 & -1 & 0 \\ 0 & 0 & -1 \\ 0 & 0 & 0 \end{bmatrix} & \mathbf{T}_0^{(1)} = \frac{\mathbf{J}_z}{\sqrt{2}} &\doteq \frac{\hbar}{\sqrt{2}} \begin{bmatrix} 1 & 0 & 0 \\ 0 & 0 & 0 \\ 0 & 0 & -1 \end{bmatrix} \\ \mathbf{T}_{-1}^{(1)} = \frac{\mathbf{J}_-}{2} &\doteq \frac{\hbar}{\sqrt{2}} \begin{bmatrix} 0 & 0 & 0 \\ 1 & 0 & 0 \\ 0 & 1 & 0 \end{bmatrix} & \mathbf{T}_2^{(2)} = \frac{\mathbf{J}_\pm^2}{2\hbar} &\doteq \hbar \begin{bmatrix} 0 & 0 & 1 \\ 0 & 0 & 0 \\ 0 & 0 & 0 \end{bmatrix} \\ \mathbf{T}_1^{(2)} = -\frac{\mathbf{J}_+\mathbf{J}_z}{\hbar} - \frac{\mathbf{J}_+}{2} &\doteq \frac{\hbar}{\sqrt{2}} \begin{bmatrix} 0 & -1 & 0 \\ 0 & 0 & 1 \\ 0 & 0 & 0 \end{bmatrix} & \mathbf{T}_0^{(2)} = -\hbar \mathbf{I} \sqrt{\frac{2}{3}} + \frac{\mathbf{J}_z^2}{\hbar} \sqrt{\frac{3}{2}} &\doteq \frac{\hbar}{\sqrt{6}} \begin{bmatrix} 1 & 0 & 0 \\ 0 & -2 & 0 \\ 0 & 0 & 1 \end{bmatrix} \\ \mathbf{T}_{-1}^{(2)} = \frac{\mathbf{J}_-\mathbf{J}_z}{\hbar} - \frac{\mathbf{J}_-}{2} &\doteq \frac{\hbar}{\sqrt{2}} \begin{bmatrix} 0 & 0 & 0 \\ 1 & 0 & 0 \\ 0 & -1 & 0 \end{bmatrix} & \mathbf{T}_{-2}^{(2)} = \frac{\mathbf{J}_-^2}{2\hbar} &\doteq \hbar \begin{bmatrix} 0 & 0 & 0 \\ 0 & 0 & 0 \\ 1 & 0 & 0 \end{bmatrix} \end{aligned} \quad (3.21)$$

The matrix representations are specific to a spin-1 space, but the rest of the equation is general. An overall constant factor was chosen such that the trace of the product of an operator with its own transpose was  $\hbar^2$ , which leaves only two overall minus signs—one in each rank—to be chosen arbitrarily. It can also be shown that, together with the identity matrix, these form a complete linearly-independent set over the set of  $3 \times 3$  matrices. Thus, we can use them as a basis for the density matrix:

$$\boldsymbol{\rho} = \frac{\mathbf{I}}{3} + \frac{1}{\hbar^2} \left[ \frac{\langle \mathbf{J}_z \rangle \mathbf{J}_z}{2} + \frac{\langle \mathbf{J}_- \rangle \mathbf{J}_+}{4} + \frac{\langle \mathbf{J}_+ \rangle \mathbf{J}_-}{4} + \langle \mathbf{T}_0^{(2)} \rangle \mathbf{T}_0^{(2)} + \langle \mathbf{T}_2^{(2)} \rangle \mathbf{T}_2^{(2)} + \langle \mathbf{T}_{-2}^{(2)} \rangle \mathbf{T}_{-2}^{(2)} - \langle \mathbf{T}_1^{(2)} \rangle \mathbf{T}_{-1}^{(2)} - \langle \mathbf{T}_{-1}^{(2)} \rangle \mathbf{T}_1^{(2)} \right] \quad (3.22)$$

Recall that  $\boldsymbol{\rho} \equiv \rho_{\mu\mu'}$  here. However, the above expansion would also apply to the  $2^3\mathbf{P}_1$  form of  $\rho_{mm'}$ , if we needed it. The  $2^3\mathbf{P}_2$  form would need rank 3 and rank 4 tensors, while the  $2^3\mathbf{P}_0$  form is just a scalar.

$$\text{Also, } \mathbf{J}_+ = \mathbf{J}_-^\dagger, \mathbf{T}_1^{(2)} = -(\mathbf{T}_{-1}^{(2)})^\dagger, \mathbf{T}_2^{(2)} = (\mathbf{T}_{-2}^{(2)})^\dagger.$$

## 3.7 Light With Spherical Tensors

Table 3.5. Symbols Introduced In Section 3.7

Symbol	Units	Description
$F(\omega')$	—	Lorentzian lineshape factor
$F'(\omega')$	—	Dispersive counterpart to $F(\omega')$
$\Phi(z)$	$\text{cm}^{-2}\text{s}^{-1}$	Photon flux density; argument will usually be omitted
$z$	cm	Length along cell in local system
$W_i$	a.u.	Arbitrary operators
$K_1$	none or $\text{erg}^{-2}\text{s}^{-2}$	Selected coefficient in expansion of $\rho$ , as in Equation (3.22)
$\alpha(z)$	$\text{cm}^{-3}\text{s}^{-1}$	Photons gained (negative) per unit volume per unit time
$n_S$	$\text{cm}^{-3}$	$2^3\text{S}_1$ metastable density
$Q_*$	$\text{erg}^2\text{cm}^3\text{s}$	“Reduced” cross sections, to shorten later expressions
$A_1$	$\text{erg}^2\text{cm}^3\text{s}$	Symmetrical transition matrix, function of polarization
$A_2$	$\text{erg}^2\text{cm}^3\text{s}$	Dispersive transition matrix, function of polarization
$\vec{a}_p$	$\text{erg}^2\text{cm}^3\text{s}$	Optical forcing vector, inhomogeneous term
$C_1$	$\text{erg}^2\text{cm}^3\text{s}$	Output matrix, function of polarization
$C_p$	$\text{erg}^2\text{cm}^3\text{s}$	Output scalar, inhomogeneous term, function of polarization
$\vec{v}$	$\text{erg} \cdot \text{s}$	Vector of ensemble expectations

Note that the entries listed as being in  $\text{erg}^2\text{cm}^3\text{s}$  may, in fact, only be proportional to those units. That is, factors such as  $\pi$  or  $10^3$  are not examined in assigning these units.

This section extends [34] to include all quadrupole terms with all optical polarizations and orientations.

## 3.7.1 General Concerns

When we use Equation (3.15), we will find it more useful to rewrite all references to the lineshape factor  $f(\omega')$  defined in Equation (3.11) as [34]:

$$F(\omega') \equiv f(\omega') + f^*(\omega') = \frac{2}{1 + \tau^2 (\omega' - \omega'_0)^2} \quad F'(\omega') \equiv f(\omega') - f^*(\omega') = \frac{2i\tau (\omega' - \omega'_0)}{1 + \tau^2 (\omega' - \omega'_0)^2} \quad (3.23)$$

The first of these is Lorentzian with half-width at half-maximum  $\tau^{-1}$ , while the second is its dispersive counterpart.

Note that the photon flux density  $\Phi = \frac{cE_0^2}{8\pi\hbar\omega'}$  [34] and substitute it into Equation (3.15):

$$\begin{aligned} & \left( \frac{d\rho_{\mu\mu'}}{dt} \right)_L \\ &= \frac{-2\pi\omega'\tau}{\hbar c} \Phi \sum_{m,\mu''} \left[ \langle \mu | \vec{e}^* \cdot \vec{D} | m \rangle \langle m | \vec{e} \cdot \vec{D} | \mu'' \rangle \rho_{\mu''\mu'} f(\omega') + \rho_{\mu\mu''} \langle \mu'' | \vec{e}^* \cdot \vec{D} | m \rangle \langle m | \vec{e} \cdot \vec{D} | \mu' \rangle f^*(\omega') \right] \end{aligned} \quad (3.24)$$

We'd like to find out how the density operator  $\rho$  evolves in time, but, given the expansion in Equation (3.22), we instead choose to find, equivalently, how the expectation values of the operators used therein evolve in time. It is a basic property of the density operator (e.g., [48]) that the ensemble expectation of an operator is equal to the trace of the product of the density operator with the operator in question. Given the properties of the trace operator, it is clear that, for time-invariant operators (such as the angular momentum operators), the evolution of the various expectation values are, e.g.:

$$\frac{d\langle J_z \rangle}{dt} = \text{Tr} \left[ \frac{d\rho}{dt} J_z \right], \quad \frac{d\langle J_+ \rangle}{dt} = \text{Tr} \left[ \frac{d\rho}{dt} J_+ \right], \quad \text{etc...} \quad (3.25)$$

The time evolution of each of these expectations is linear in  $\frac{d\rho}{dt}$ , Equation (3.24) shows  $\frac{d\rho}{dt}$  is linear in  $\rho$ , and Equation (3.22) shows  $\rho$  is linear in each of its terms. Consequently, provided we repeat for every term in Equation (3.22), each equation of the form of Equations (3.25) can be expressed instead as a sum of terms, each due to a different term of Equation (3.22), and, more to the point, these terms can be obtained quite simply by temporarily *ignoring* all other terms of Equation (3.22).

The procedure is to substitute one term of Equation (3.22) — identified as  $K_1 \langle W_1 \rangle W_2$  — into Equation (3.24). For each form of Equations (3.25), we can find the time evolution of the expectation  $\langle W_3 \rangle$  due to the aforementioned term by simple substitution. For the identity term of Equation (3.22), simply take  $W_1 = W_2 = I$ .

Following the procedure described above, we obtain:

$$\begin{aligned}
& \left. \frac{d\langle W_3 \rangle}{dt} \right|_{W_1, W_2} \\
&= \frac{-2\pi\omega'\tau K_1}{\hbar c} \Phi \left[ \langle \mu | \vec{e}^* \cdot \vec{D} | m \rangle \langle m | \vec{e} \cdot \vec{D} | \mu'' \rangle \langle \mu'' | W_2 | \mu' \rangle \langle \mu' | W_3 | \mu \rangle f(\omega') \right. \\
&\quad \left. + \langle \mu | W_2 | \mu'' \rangle \langle \mu'' | \vec{e}^* \cdot \vec{D} | m \rangle \langle m | \vec{e} \cdot \vec{D} | \mu' \rangle \langle \mu' | W_3 | \mu \rangle f^*(\omega') \right] \langle W_1 \rangle \\
&= \frac{-\pi\omega'\tau K_1}{\hbar c} \Phi \langle \mu | \vec{e}^* \cdot \vec{D} | m \rangle \langle m | \vec{e} \cdot \vec{D} | \mu' \rangle \left[ \langle \mu' | \{W_2, W_3\} | \mu \rangle F(\omega') + \langle \mu' | [W_2, W_3] | \mu \rangle F'(\omega') \right] \langle W_1 \rangle
\end{aligned} \tag{3.26}$$

Summation over  $m, \mu, \mu',$  and  $\mu''$  is assumed in this equation.

Not only do we need to compute the time evolution of the density matrix (or the expectation values), but we also need to know how much light is absorbed in the cell. Similarly to [34], we define the photon gain (always negative) per unit volume per unit time as:

$$\alpha(z) = n_S \text{Tr} \left( \frac{d\rho}{dt} \right), \tag{3.27}$$

where we've called attention to the fact that this value, like others, tends to change over the length of the cell; we will return to this fact in Section 3.11.

The relation equivalent to Equation (3.26) is:

$$- \text{Tr} \left( \frac{d\rho}{dt} \right) \Big|_{W_1, W_2} = \frac{2\pi\omega'\tau K_1}{\hbar c} \Phi \langle \mu | \vec{e}^* \cdot \vec{D} | m \rangle \langle m | \vec{e} \cdot \vec{D} | \mu' \rangle \langle \mu' | W_2 | \mu \rangle F(\omega') \langle W_1 \rangle$$

We can cut the work involved in evaluating Equations (3.25) down by a third by noting:

$$\left( \langle \alpha | W_4 | \beta \rangle \right)^* = \langle \beta | W_4^\dagger | \alpha \rangle \quad \left( \vec{e} \cdot \vec{D} \right)^\dagger = \vec{e}^* \cdot \vec{D}$$

where  $|\alpha\rangle$  and  $|\beta\rangle$  are arbitrary kets in a compatible space. This can be used to deduce that:

$$\begin{aligned}
& \left[ \langle \mu | \vec{e}^* \cdot \vec{D} | m \rangle \langle m | \vec{e} \cdot \vec{D} | \mu' \rangle \langle \mu' | W_4 | \mu \rangle F(\omega') \right]^* = \langle \mu | \vec{e}^* \cdot \vec{D} | m \rangle \langle m | \vec{e} \cdot \vec{D} | \mu' \rangle \langle \mu' | W_4^\dagger | \mu \rangle F(\omega') \\
& \left[ \langle \mu | \vec{e}^* \cdot \vec{D} | m \rangle \langle m | \vec{e} \cdot \vec{D} | \mu' \rangle \langle \mu' | W_4 | \mu \rangle F'(\omega') \right]^* = - \langle \mu | \vec{e}^* \cdot \vec{D} | m \rangle \langle m | \vec{e} \cdot \vec{D} | \mu' \rangle \langle \mu' | W_4^\dagger | \mu \rangle F'(\omega')
\end{aligned}$$

$W_4$  is, of course, one of the [anti-]commutators in Equation (3.26). This means we do not need to evaluate with  $W_3 = J_-, T_{-1}^{(2)},$  or  $T_{-2}^{(2)}$ .

### 3.7.2 Building Blocks for Expressing Traces

Knowing that a number of traces will show up repeatedly, we assign shorter names:

$$\begin{aligned}
\hbar Q_{zz} &= \langle \mu | \vec{\mathbf{e}}^* \cdot \vec{\mathbf{D}} | m \rangle \langle m | \vec{\mathbf{e}} \cdot \vec{\mathbf{D}} | \mu' \rangle \langle \mu' | J_z^2 | \mu \rangle & Q_z &= \langle \mu | \vec{\mathbf{e}}^* \cdot \vec{\mathbf{D}} | m \rangle \langle m | \vec{\mathbf{e}} \cdot \vec{\mathbf{D}} | \mu' \rangle \langle \mu' | J_z | \mu \rangle \\
\hbar Q_{+-} &= \langle \mu | \vec{\mathbf{e}}^* \cdot \vec{\mathbf{D}} | m \rangle \langle m | \vec{\mathbf{e}} \cdot \vec{\mathbf{D}} | \mu' \rangle \langle \mu' | J_- J_+ + J_+ J_- | \mu \rangle & Q_{+-} &= \langle \mu | \vec{\mathbf{e}}^* \cdot \vec{\mathbf{D}} | m \rangle \langle m | \vec{\mathbf{e}} \cdot \vec{\mathbf{D}} | \mu' \rangle \langle \mu' | J_+ | \mu \rangle \\
Q_I &= \langle \mu | \vec{\mathbf{e}}^* \cdot \vec{\mathbf{D}} | m \rangle \langle m | \vec{\mathbf{e}} \cdot \vec{\mathbf{D}} | \mu \rangle \hbar & Q_- &= \langle \mu | \vec{\mathbf{e}}^* \cdot \vec{\mathbf{D}} | m \rangle \langle m | \vec{\mathbf{e}} \cdot \vec{\mathbf{D}} | \mu' \rangle \langle \mu' | J_- | \mu \rangle \\
Q_{-2} &= \langle \mu | \vec{\mathbf{e}}^* \cdot \vec{\mathbf{D}} | m \rangle \langle m | \vec{\mathbf{e}} \cdot \vec{\mathbf{D}} | \mu' \rangle \langle \mu' | T_{-2}^{(2)} | \mu \rangle & Q_2 &= \langle \mu | \vec{\mathbf{e}}^* \cdot \vec{\mathbf{D}} | m \rangle \langle m | \vec{\mathbf{e}} \cdot \vec{\mathbf{D}} | \mu' \rangle \langle \mu' | T_2^{(2)} | \mu \rangle \\
Q_{-1} &= \langle \mu | \vec{\mathbf{e}}^* \cdot \vec{\mathbf{D}} | m \rangle \langle m | \vec{\mathbf{e}} \cdot \vec{\mathbf{D}} | \mu' \rangle \langle \mu' | T_{-1}^{(2)} | \mu \rangle & Q_1 &= \langle \mu | \vec{\mathbf{e}}^* \cdot \vec{\mathbf{D}} | m \rangle \langle m | \vec{\mathbf{e}} \cdot \vec{\mathbf{D}} | \mu' \rangle \langle \mu' | T_1^{(2)} | \mu \rangle \\
\hbar Q_{00} &= \langle \mu | \vec{\mathbf{e}}^* \cdot \vec{\mathbf{D}} | m \rangle \langle m | \vec{\mathbf{e}} \cdot \vec{\mathbf{D}} | \mu' \rangle \langle \mu' | (T_0^{(2)})^2 | \mu \rangle & Q_0 &= \langle \mu | \vec{\mathbf{e}}^* \cdot \vec{\mathbf{D}} | m \rangle \langle m | \vec{\mathbf{e}} \cdot \vec{\mathbf{D}} | \mu' \rangle \langle \mu' | T_0^{(2)} | \mu \rangle \\
\hbar Q_{11} &= \langle \mu | \vec{\mathbf{e}}^* \cdot \vec{\mathbf{D}} | m \rangle \langle m | \vec{\mathbf{e}} \cdot \vec{\mathbf{D}} | \mu' \rangle \langle \mu' | T_{-1}^{(2)} T_1^{(2)} + T_1^{(2)} T_{-1}^{(2)} | \mu \rangle \\
\hbar Q_{22} &= \langle \mu | \vec{\mathbf{e}}^* \cdot \vec{\mathbf{D}} | m \rangle \langle m | \vec{\mathbf{e}} \cdot \vec{\mathbf{D}} | \mu' \rangle \langle \mu' | T_{-2}^{(2)} T_2^{(2)} + T_2^{(2)} T_{-2}^{(2)} | \mu \rangle
\end{aligned}$$

Many of these can be expressed in terms of each other:

$$\begin{aligned}
Q_{zz} &= \frac{2}{3} Q_I + \sqrt{\frac{2}{3}} Q_0 & Q_{+-} &= \frac{8}{3} Q_I - \sqrt{\frac{8}{3}} Q_0 \\
Q_{00} &= \frac{1}{3} Q_I - \sqrt{\frac{1}{6}} Q_0 & Q_{11} &= -\frac{2}{3} Q_I + \sqrt{\frac{1}{6}} Q_0 & Q_{22} &= \frac{2}{3} Q_I + \sqrt{\frac{2}{3}} Q_0
\end{aligned}$$

### 3.7.3 Traces With Arbitrary Polarization

All of the traces of the preceding subsection can be evaluated in the coordinate system described in Section 3.1, with the values of  $\vec{\mathbf{e}}$  given by Equation (3.3). The results, from Appendix C, are:

$$\begin{aligned}
Q_z &= \frac{D_0^2 \hbar \sin 2\epsilon}{6} (\hat{\mathbf{z}} \cdot \hat{\mathbf{Z}}) \begin{bmatrix} 2 & 3 & -5 \end{bmatrix} \\
Q_{+-} &= \frac{i D_0^2 \hbar \sin 2\epsilon}{6} \sqrt{1 - (\hat{\mathbf{z}} \cdot \hat{\mathbf{Z}})^2} \begin{bmatrix} -2 & -3 & 5 \end{bmatrix} \\
Q_I &= \frac{D_0^2 \hbar}{3} \begin{bmatrix} 1 & 3 & 5 \end{bmatrix} \\
Q_2 &= \frac{D_0^2 \hbar}{12} \frac{[(\hat{\mathbf{y}} \cdot \hat{\mathbf{Z}}) + i(\hat{\mathbf{x}} \cdot \hat{\mathbf{Z}})(\hat{\mathbf{z}} \cdot \hat{\mathbf{Z}})]^2 \cos^2 \epsilon + [(\hat{\mathbf{x}} \cdot \hat{\mathbf{Z}}) - i(\hat{\mathbf{y}} \cdot \hat{\mathbf{Z}})(\hat{\mathbf{z}} \cdot \hat{\mathbf{Z}})]^2 \sin^2 \epsilon}{(\hat{\mathbf{z}} \cdot \hat{\mathbf{Z}})^2 - 1} \begin{bmatrix} 2 & -3 & 1 \end{bmatrix}
\end{aligned}$$

$$Q_1 = \frac{D_0^2 \hbar}{12} \frac{i(\hat{\mathbf{z}} \cdot \hat{\mathbf{Z}}) \left[ 1 - (\hat{\mathbf{z}} \cdot \hat{\mathbf{Z}})^2 \right] + \cos 2\epsilon \left[ i(\hat{\mathbf{x}} \cdot \hat{\mathbf{Z}})^2 (\hat{\mathbf{z}} \cdot \hat{\mathbf{Z}}) - i(\hat{\mathbf{y}} \cdot \hat{\mathbf{Z}})^2 (\hat{\mathbf{z}} \cdot \hat{\mathbf{Z}}) + 2(\hat{\mathbf{x}} \cdot \hat{\mathbf{Z}})(\hat{\mathbf{y}} \cdot \hat{\mathbf{Z}}) \right]}{\sqrt{1 - (\hat{\mathbf{z}} \cdot \hat{\mathbf{Z}})^2}} \\ \times \begin{bmatrix} 2 & -3 & 1 \end{bmatrix}$$

$$Q_0 = \frac{D_0^2 \hbar}{12 \sqrt{6}} \left\{ 3(\hat{\mathbf{z}} \cdot \hat{\mathbf{Z}})^2 - 1 - 3 \left[ (\hat{\mathbf{x}} \cdot \hat{\mathbf{Z}})^2 - (\hat{\mathbf{y}} \cdot \hat{\mathbf{Z}})^2 \right] \cos 2\epsilon \right\} \begin{bmatrix} 2 & -3 & 1 \end{bmatrix}$$

$$Q_- = Q_+^* \quad Q_{-2} = Q_2^* \quad Q_{-1} = -Q_1^*$$

### 3.7.4 Summary Plots

The color in these plots is a continuously-varying function of phase, with key points being:

cyan	blue	red	green
+real	+imag	-real	-imag
0	90	180	270

The axes serve as both dependent and independent variables. The magnitude of the distance from the origin is the dependent variable, and is equal to the reduced cross section in question, times  $10^{68}$  (since the reduced cross sections are very tiny). The direction represents the two independent variables, and gives the direction of light propagation in the world system. Each figure contains, from left to right, the  $D_0$ ,  $D_1$ , and  $D_2$  components, respectively. Due to the apparent likeness, it should be emphasized that these are *not* constant-probability contours of any sort. These are plots of *selected* reduced cross sections from Section 3.7.2. Most of the possible plots were significantly less “interesting.”

Figure 3.3 illustrates that  $Q_I$  is isotropic for all polarizations. This is to be expected, as it indicates absorption regardless of the atomic polarization, and, for that matter, optical polarization.

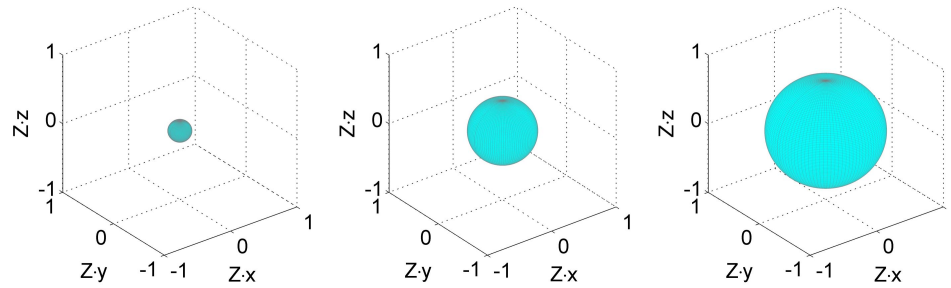


Figure 3.3.  $Q_l$  for all polarizations  $\epsilon$ . The radial units are  $10^{-61} \text{ cm}^2$ .

Figure 3.4 illustrates, for LCP light, the very frequently-occurring reduced cross section  $Q_z$ . The dependence is a simple cosine of the angle between the light and  $H_0$ , and also flips sign when the handedness of the polarization changes. This cross section appears, among other places, in monitoring the rank-one portion of the density matrix, in increasing the longitudinal polarization of metastables (*pumping*), and in introducing virtual light shifts. Clearly, the reversal of sign is very important in the latter case for the ability to operate in magnetometer mode, as described in Section 2.3.

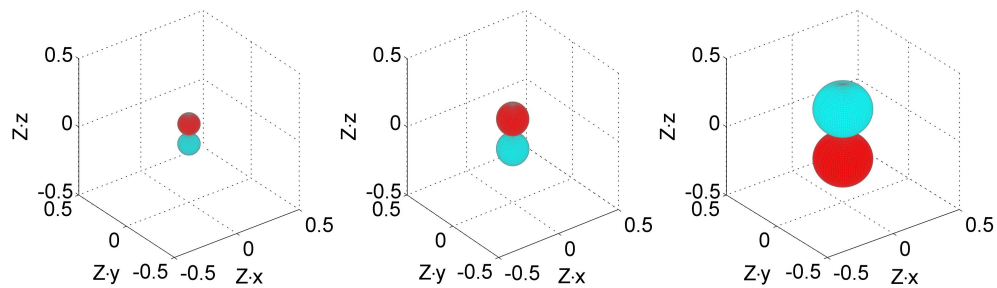


Figure 3.4.  $Q_z$  for LCP light,  $\epsilon = -\pi/4$ . The radial units are  $10^{-61} \text{ cm}^2$ .

Figures 3.5 and 3.6 illustrate that  $Q_+$  changes sign between left- and right-handed circularly polarized light, but does not change sign when light propagates in the opposite direction. Figures 3.7 and 3.10 illustrate the opposite: a parity flip changes the sign of the cross section, but the handedness of the polarization does not. Figures 3.8 and 3.9 illustrate intermediate polarizations. 90% left-circular was chosen to illustrate misalignments, and because it was difficult to visually discern 99%, e.g., from 100%.

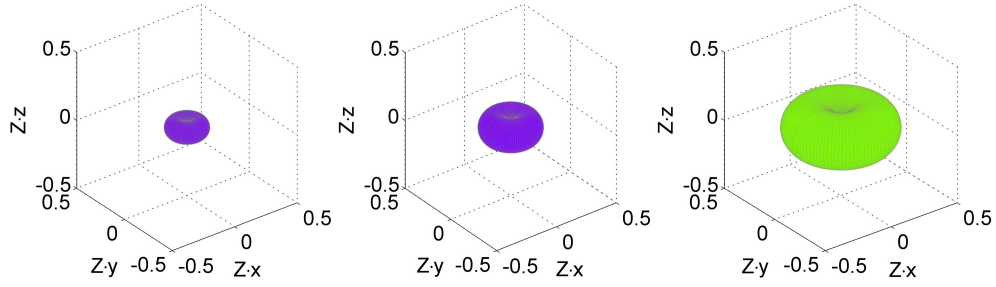


Figure 3.5.  $Q_+$  for LCP light,  $\epsilon = -\pi/4$ . The radial units are  $10^{-61} \text{ cm}^2$ .

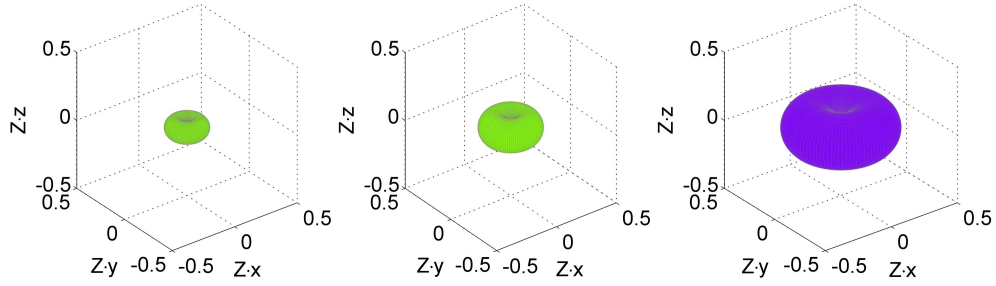


Figure 3.6.  $Q_+$  for RCP light,  $\epsilon = \pi/4$ . The radial units are  $10^{-61} \text{ cm}^2$ .

The failure to observe an equivalency between a flip in polarization of the light and flip in the direction of propagation on  $Q_+$  ( $Q_+$  was selected because it, along with its conjugate, was the only difficult one) is likely related to the choice of coordinate system affecting the definitions of  $Q_{\pm}$ . A simple thought experiment associated with the electric dipole approximation should lead one to believe that the overall *signal* on the photodetector must observe this equivalency [50]. But the plots show that, for  $-2\epsilon = \theta = \mp\pi/2$  and  $\phi = \pi/2$ ,  $Q_+ = \frac{\pm i D_0^2 \hbar}{6} \begin{bmatrix} -2 & -3 & 5 \end{bmatrix}$ . Correspondingly, upon solving for the state of the system using the methods of Chapter 5, we find that the difference is that the sign flips on the solutions of  $\langle J_{\pm} \rangle$ , but not  $\langle J_z \rangle$ . As described later in Equation (3.29), however, the output is measured by multiplying again with  $Q_{\pm}$  and  $Q_z$ , so the reversal cannot be measured on the transmitted light, and the situation is consistent with our expectations. Note that the issue does not arise in [34] because  $Q_{\pm} = 0$  when the light propagates [anti-]parallel to  $H_0$ .

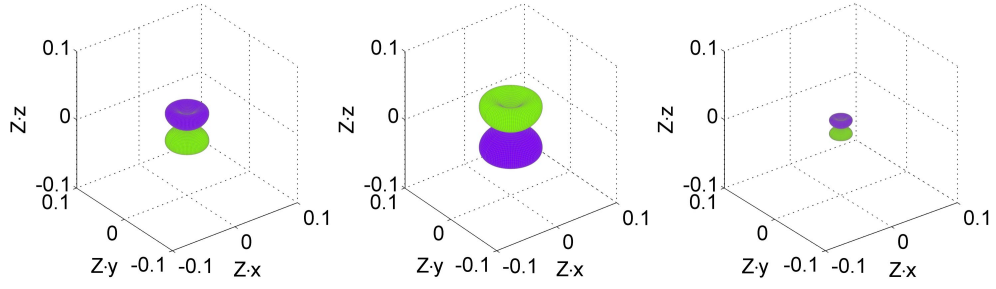


Figure 3.7.  $Q_1$  for LCP light,  $\epsilon = -\pi/4$ . The radial units are  $10^{-61} \text{ cm}^2$ .

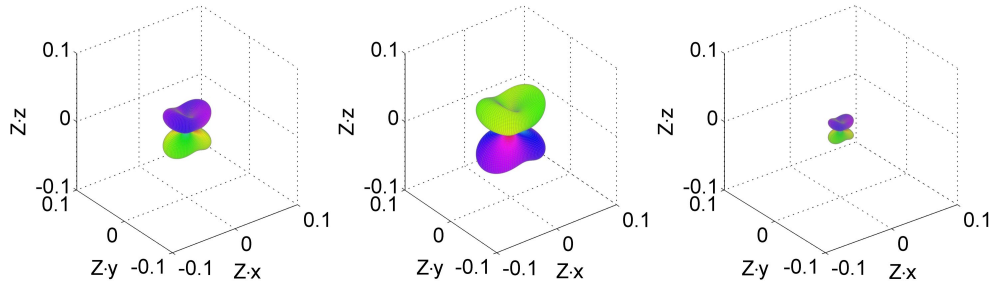


Figure 3.8.  $Q_1$  for almost-LCP light (90%),  $\epsilon = -9\pi/40$ . The radial units are  $10^{-61} \text{ cm}^2$ .

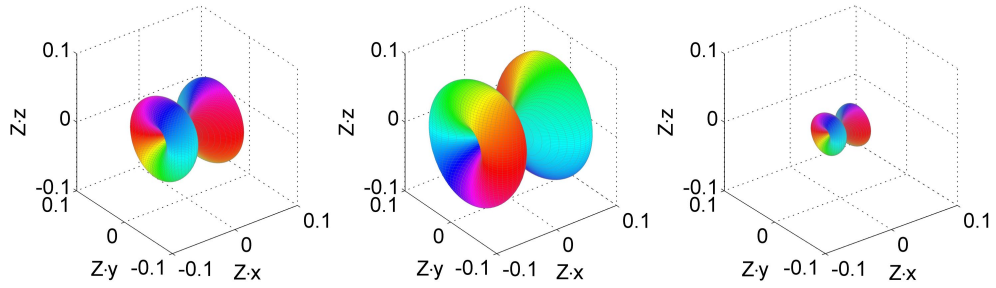


Figure 3.9.  $Q_1$  for linearly-polarized light,  $\epsilon = 0$ . The radial units are  $10^{-61} \text{ cm}^2$ .

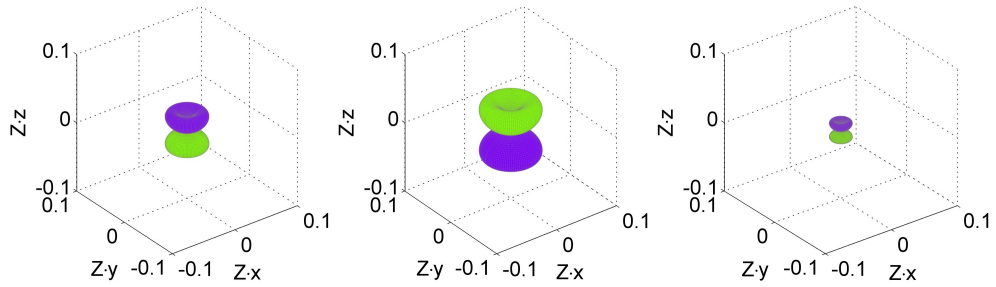


Figure 3.10.  $Q_1$  for RCP light,  $\epsilon = \pi/4$ . The radial units are  $10^{-61} \text{ cm}^2$ .

Figures 3.11, 3.12, and 3.13 illustrate the progression of  $Q_0$  from LCP to linearly-polarized light. These are roughly the equivalent of  $Q_z$  in importance, but for the rank-two portion of the density matrix.

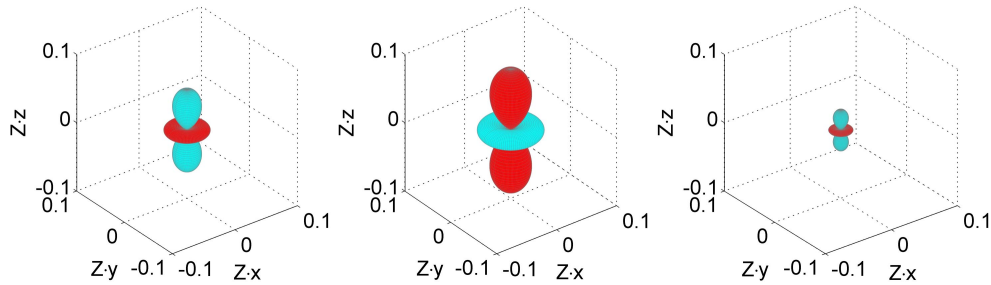


Figure 3.11.  $Q_0$  for LCP light,  $\epsilon = -\pi/4$ . The radial units are  $10^{-61} \text{ cm}^2$ .

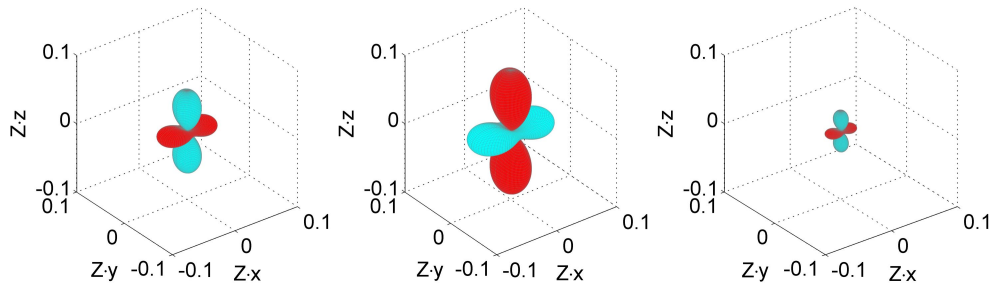


Figure 3.12.  $Q_0$  for almost-LCP light (90%),  $\epsilon = -9\pi/40$ . The radial units are  $10^{-61} \text{ cm}^2$ .

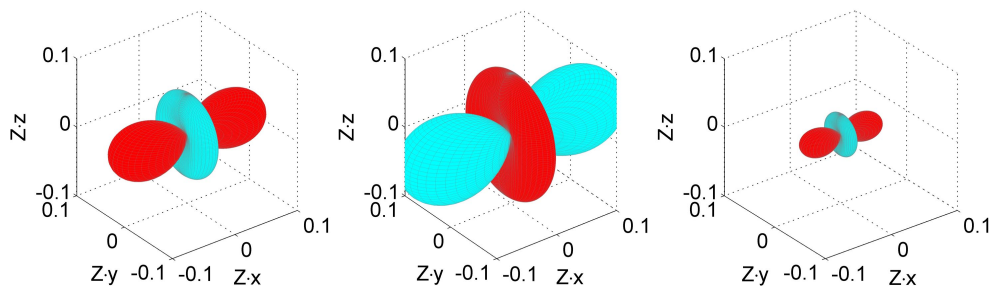


Figure 3.13.  $Q_0$  for linearly-polarized light,  $\epsilon = 0$ . The radial units are  $10^{-61} \text{ cm}^2$ .

Figures 3.14, 3.15, 3.16, and 3.17 are merely an assortment of other effects visible on some of the other cross sections, and have no immediately apparent interpretation, other than to note that all of the “almost-LCP” plots, some of which are shown in Figures 3.12, 3.8, and 3.17, bear a strong similarity to the LCP plots, but with a marked distortion.

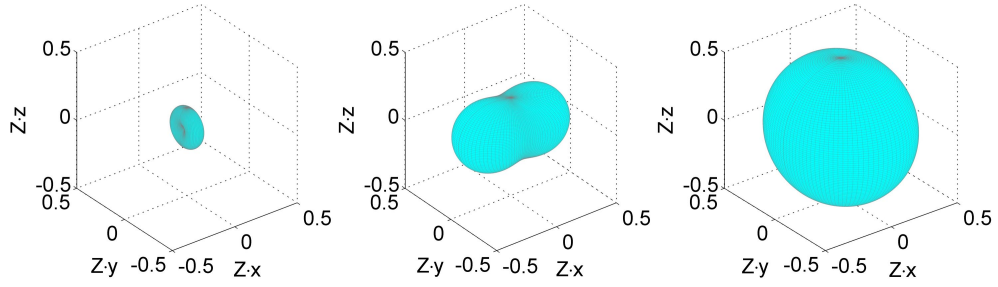


Figure 3.14.  $Q_{zz}$  for linearly-polarized light,  $\epsilon = 0$ . The radial units are  $10^{-61} \text{ cm}^2$ .

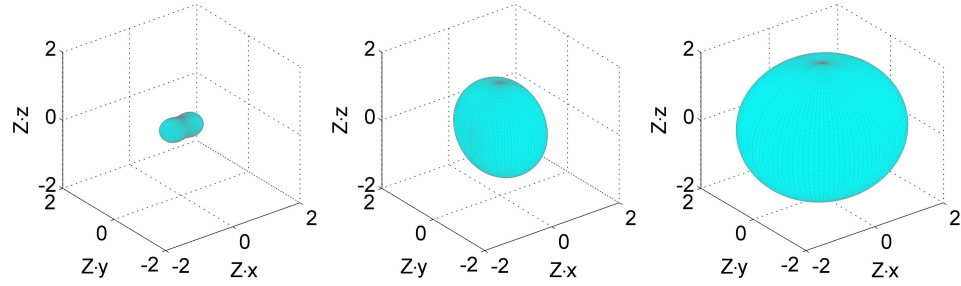


Figure 3.15.  $Q_{+-}$  for linearly-polarized light,  $\epsilon = 0$ . The radial units are  $10^{-61} \text{ cm}^2$ .

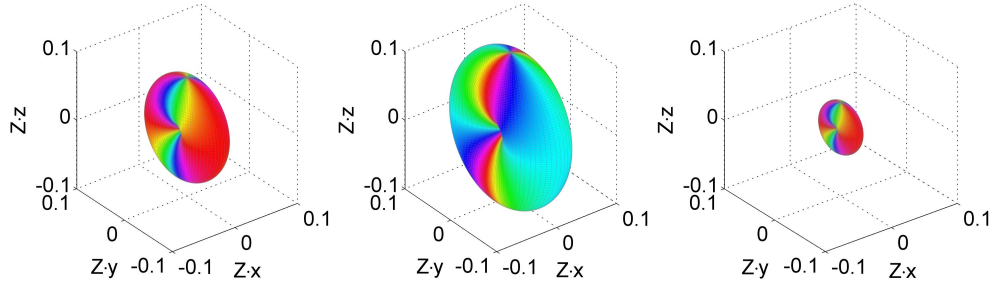


Figure 3.16.  $Q_2$  for linearly-polarized light,  $\epsilon = 0$ . The radial units are  $10^{-61} \text{ cm}^2$ .

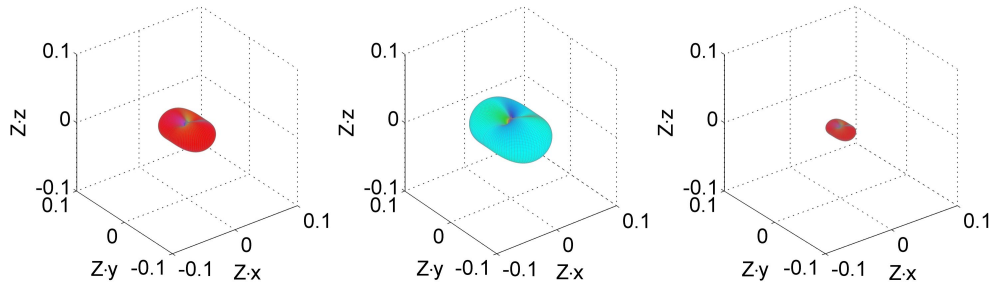


Figure 3.17.  $Q_2$  for almost-LCP light (90%),  $\epsilon = -9\pi/40$ . The radial units are  $10^{-61} \text{ cm}^2$ .

### 3.7.5 Compilation of Traces

Equation (3.24), which describes the time evolution, can be reformulated as:

$$\left(\frac{d\vec{v}}{dt}\right)_L = \frac{\pi\Phi\omega'}{24c\hbar^2} \sum_{\omega'_0} [\tau F(\omega' - \omega'_0) \mathbf{A}_1 + \tau F'(\omega' - \omega'_0) \mathbf{A}_2] \vec{v} - \frac{2\pi\Phi\omega'}{3c\hbar} \sum_{\omega'_0} \tau F(\omega' - \omega'_0) \vec{a}_p, \quad (3.28)$$

$$\text{where } \vec{a}_p = \begin{bmatrix} Q_+ \\ Q_z \\ Q_- \\ Q_2 \\ Q_1 \\ Q_0 \\ Q_{-1} \\ Q_{-2} \end{bmatrix}, \text{ and } \vec{v} \equiv \begin{bmatrix} \langle J_+ \rangle \\ \langle J_z \rangle \\ \langle J_- \rangle \\ \langle T_2^{(2)} \rangle \\ \langle T_1^{(2)} \rangle \\ \langle T_0^{(2)} \rangle \\ \langle T_{-1}^{(2)} \rangle \\ \langle T_{-2}^{(2)} \rangle \end{bmatrix}.$$

After a good deal of work, applying the techniques outlined in Section 3.7.1, we can obtain the values of the propagation matrices in terms of the reduced cross sections. This is an extraordinarily unpleasant exercise in bookkeeping, but the derivation is hardly profound. See Appendix D for the list of commutators and anticommutators used in the process.

$$\mathbf{A}_1 = \begin{bmatrix} -6Q_{+-} & 24Q_1 & -24Q_2 & -24Q_- & 24Q_z & 4\sqrt{6}Q_+ & 0 & 0 \\ -12Q_{-1} & -24Q_{zz} & 12Q_1 & 0 & 12Q_- & -8\sqrt{6}Q_z & -12Q_+ & 0 \\ -24Q_{-2} & -24Q_{-1} & -6Q_{+-} & 0 & 0 & 4\sqrt{6}Q_- & -24Q_z & -24Q_+ \\ -6Q_+ & 0 & 0 & -24Q_{22} & 24Q_1 & -8\sqrt{6}Q_2 & 0 & 0 \\ 6Q_z & 6Q_+ & 0 & -24Q_{-1} & 24Q_{11} & 4\sqrt{6}Q_1 & -24Q_2 & 0 \\ \sqrt{6}Q_- & -4\sqrt{6}Q_z & \sqrt{6}Q_+ & -8\sqrt{6}Q_{-2} & -4\sqrt{6}Q_{-1} & -48Q_{00} & -4\sqrt{6}Q_1 & -8\sqrt{6}Q_2 \\ 0 & -6Q_- & -6Q_z & 0 & -24Q_{-2} & 4\sqrt{6}Q_{-1} & 24Q_{11} & -24Q_1 \\ 0 & 0 & -6Q_- & 0 & 0 & -8\sqrt{6}Q_{-2} & 24Q_{-1} & -24Q_{22} \end{bmatrix},$$

and

$$\mathbf{A}_2 = \begin{bmatrix} 12Q_z & -12Q_+ & 0 & 48Q_{-1} & -24\sqrt{6}Q_0 & 24\sqrt{6}Q_1 & -48Q_2 & 0 \\ -6Q_- & 0 & 6Q_+ & -48Q_{-2} & 24Q_{-1} & 0 & -24Q_1 & 48Q_2 \\ 0 & 12Q_- & -12Q_z & 0 & -48Q_{-2} & 24\sqrt{6}Q_{-1} & -24\sqrt{6}Q_0 & 48Q_1 \\ -12Q_1 & -24Q_2 & 0 & 24Q_z & 12Q_+ & 0 & 0 & 0 \\ -6\sqrt{6}Q_0 & -12Q_1 & -12Q_2 & 12Q_- & 12Q_z & 6\sqrt{6}Q_+ & 0 & 0 \\ -6\sqrt{6}Q_{-1} & 0 & -6\sqrt{6}Q_1 & 0 & 6\sqrt{6}Q_- & 0 & 6\sqrt{6}Q_+ & 0 \\ -12Q_{-2} & 12Q_{-1} & -6\sqrt{6}Q_0 & 0 & 0 & 6\sqrt{6}Q_- & -12Q_z & 12Q_+ \\ 0 & 24Q_{-2} & -12Q_{-1} & 0 & 0 & 0 & 12Q_- & -24Q_z \end{bmatrix}.$$

Similarly, Equation (3.27) can be recast as:

$$\alpha(z) = -\frac{\pi\Phi\omega'}{6c\hbar^3} n_S \sum_{\omega'_0} \tau F(\omega' - \omega'_0) (\mathbf{C}_1 \vec{v} + \hbar C_p), \quad \text{where } C_p = 4Q_l \quad (3.29)$$

and  $\mathbf{C}_1 = \left[ 3Q_- \quad 6Q_z \quad 3Q_+ \mid 12Q_{-2} \quad -12Q_{-1} \quad 12Q_0 \quad -12Q_1 \quad 12Q_2 \right]$ .

Five of these terms are kept in [34], and all five are assigned names. Using those names, and expanding a bit, we can say:

- $C_p$  is the *absorption* cross section.
- The terms in  $\mathbf{C}_1$  proportional to  $\langle J_z \rangle$  or  $\langle T_0^{(2)} \rangle$  are *dichroic monitoring* cross sections. “Dichroic” reflects the fact that absorption changes with input polarization, but output polarization is neglected here.
- $\vec{\mathbf{a}}_p$  contains the *polarization* cross sections.
- The “diagonal” terms of  $\mathbf{A}_1$  are the *light broadening* cross sections. In particular, the one corresponding to  $\langle J_z \rangle$  is considered *longitudinal*, and the one corresponding to  $\langle J_+ \rangle$  is considered *transverse*.
- The “diagonal” terms of  $\mathbf{A}_2$  are the *virtual light shift* cross sections.

### 3.8 Magnetic Field With Spherical Tensors

Table 3.6. Symbols Introduced In Section 3.8

Symbol	Units	Description
$H_z, H_\pm$	nT	Alternative description of magnetic fields
$\xi, \eta$	rad	longitude, colatitude, respectively of $H_1$ in local system
$\Theta$	rad	Replacement angle, $\theta + \xi$
$\langle \tilde{J}_z \rangle$ , etc.	erg · s	Slowly-varying angular momentum expectation value
$\langle \tilde{T}_2^{(2)} \rangle$ , etc.	erg · s	Slowly-varying angular momentum expectation value
$H'_x, H'_y, H'_z$	—	Direction cosines for true $H_1$ in world system
$\mathbf{A}_3$	—	Diagonal coupling matrix for magnetic fields $H_0$ and $H_1$
$\mathbf{A}_4$	—	Off-diagonal coupling matrix for magnetic field $H_1$
$\mathbf{A}_{4'}$	—	$\mathbf{A}_4$ , after transformation to rotating coordinates
$\mathbf{A}_4^{(1)}, \mathbf{A}_4^{(2)}, \mathbf{A}_{4'}^{(1)}, \mathbf{A}_{4'}^{(2)}$	—	rank 1&2 partitions of above
$\vec{\mathbf{v}}'$	erg · s	Vector of ensemble expectations in rotating system

This section extends [34] to include the rank-two components of the density matrix, under the action of magnetic fields, and details the approximation required to make the equations stand a chance of analytical solution.

### 3.8.1 General Concerns

Let  $2H_- \equiv H_x + iH_y$  and  $2H_+ \equiv H_x - iH_y$ . Note that this is the opposite of the way  $J_+$  and  $J_-$  are defined. The motivation for these definitions can be seen by substituting into Equation (3.16):

$$\mathcal{H}_M = \gamma H_z J_z + \gamma H_+ J_+ + \gamma H_- J_-$$

Substituting instead into Equation (3.17), we obtain:

$$\left( \frac{d\rho}{dt} \right)_M = \frac{i\gamma}{\hbar} (H_z [\rho, J_z] + H_+ [\rho, J_+] + H_- [\rho, J_-]) \quad (3.30)$$

Each of these commutators can be expanded:

$$\begin{aligned} \hbar [J_z, \rho] &= \frac{\langle J_- \rangle J_+ - \langle J_+ \rangle J_-}{4} - 2 \langle T_2^{(2)} \rangle T_{-2}^{(2)} + 2 \langle T_{-2}^{(2)} \rangle T_2^{(2)} + \langle T_1^{(2)} \rangle T_{-1}^{(2)} - \langle T_{-1}^{(2)} \rangle T_1^{(2)} \\ \hbar [J_+, \rho] &= -\frac{\langle J_z \rangle J_+ + \langle J_+ \rangle J_z}{2} + \sqrt{6} \langle T_0^{(2)} \rangle T_1^{(2)} + 2 \langle T_2^{(2)} \rangle T_{-1}^{(2)} - \sqrt{6} \langle T_1^{(2)} \rangle T_0^{(2)} - 2 \langle T_{-1}^{(2)} \rangle T_2^{(2)} \\ \hbar [J_-, \rho] &= \frac{\langle J_z \rangle J_- - \langle J_- \rangle J_z}{2} + \sqrt{6} \langle T_0^{(2)} \rangle T_{-1}^{(2)} + 2 \langle T_{-2}^{(2)} \rangle T_1^{(2)} - 2 \langle T_1^{(2)} \rangle T_{-2}^{(2)} - \sqrt{6} \langle T_{-1}^{(2)} \rangle T_0^{(2)} \end{aligned} \quad (3.31)$$

Now the operators themselves are not time-dependent, but their expectation values are. Thus, if we substituted Equation (3.22) into the LHS of Equation (3.30), we would find terms containing operators times time derivatives of expectation values of operators.

Now the operators themselves are a linearly-independent basis for  $\rho$ . Thus we can equate the coefficients of these operators on either side of the equation and drop the operators themselves. Note also that the identity operator has dropped out of both sides of the equation. Therefore, the solutions are:

$$\left( \frac{d\vec{v}}{dt} \right)_M = i\gamma \begin{bmatrix} H_z & -2H_- & 0 & 0 & 0 & 0 & 0 & 0 & 0 \\ -H_+ & 0 & H_- & 0 & 0 & 0 & 0 & 0 & 0 \\ 0 & 2H_+ & -H_z & 0 & 0 & 0 & 0 & 0 & 0 \\ \hline 0 & 0 & 0 & 2H_z & 2H_- & 0 & 0 & 0 & 0 \\ 0 & 0 & 0 & 2H_+ & H_z & \sqrt{6}H_- & 0 & 0 & 0 \\ 0 & 0 & 0 & 0 & \sqrt{6}H_+ & 0 & \sqrt{6}H_- & 0 & 0 \\ 0 & 0 & 0 & 0 & 0 & \sqrt{6}H_+ & -H_z & 2H_- & 0 \\ 0 & 0 & 0 & 0 & 0 & 0 & 2H_+ & -2H_z & 0 \end{bmatrix} \vec{v} \quad (3.32)$$

The rank-one portion, after some algebra, reduces to [34]:

$$\frac{d\langle \vec{\mathbf{J}} \rangle}{dt} = \gamma \vec{\mathbf{H}} \times \langle \vec{\mathbf{J}} \rangle$$

### 3.8.2 Orientation Issues

Ordinarily, we take  $H_0$  along world  $\hat{\mathbf{Z}}$ , and the Helmholtz coil pair  $H_1$  along world  $\hat{\mathbf{X}}$ . The Helmholtz coils, assuming uniformity, produce a field at any point in the cell of  $2H_1 \cos \omega t$ . It is common practice to introduce a “fake” quadrature component of  $H_1$ , and treat the sum as two counter-rotating magnetic fields [58]. The approximation is then to drop the rotational direction which does not match the Larmor precession introduced by  $H_0$ , leaving:

$$\vec{\mathbf{H}}' = \hat{\mathbf{X}}H_1 \cos \omega t + \hat{\mathbf{Y}}H_1 \sin \omega t + \hat{\mathbf{Z}}H_0 \quad \Rightarrow \quad H_+ = \frac{H_1}{2}e^{-i\omega t}, \quad H_- = \frac{H_1}{2}e^{i\omega t}, \quad H_z = H_0$$

The error introduced in that approach is quantified as the Bloch-Siegert shift [8], and is small for terrestrial values of  $H_0 \sim 50\,000$  nT, but noticeable in space applications, where a small  $H_0 \lesssim 1000$  nT is common, as observed in the fly-by calibration of the Cassini spacecraft [62]. We will roll back this approximation later. Note that  $H_1$  was perpendicular to world  $\hat{\mathbf{Z}}$  to begin with, so the obvious direction to take the quadrature component was along *the* mutually perpendicular direction.

However, the Helmholtz coils are fixed in the local frame, not the world frame, so their axis will generally not be perpendicular to  $H_0$ , and will sometimes even be closer to parallel. Failing to make the approximation of counter-rotating fields seems to yield an intractable differential equation, so we will make the approximation for the purposes of analytical solutions, and later describe how we rolled it back for numerical solutions.

Define the Helmholtz coil direction  $[\sin \eta \cos \xi \quad \sin \eta \sin \xi \quad \cos \eta]^T$  in local coordinates as the direction the  $H_1$  field points at time  $t = 0$ , as indicated in Figure 3.18. The dependence in that direction is  $2H_1 \cos \omega t$ .

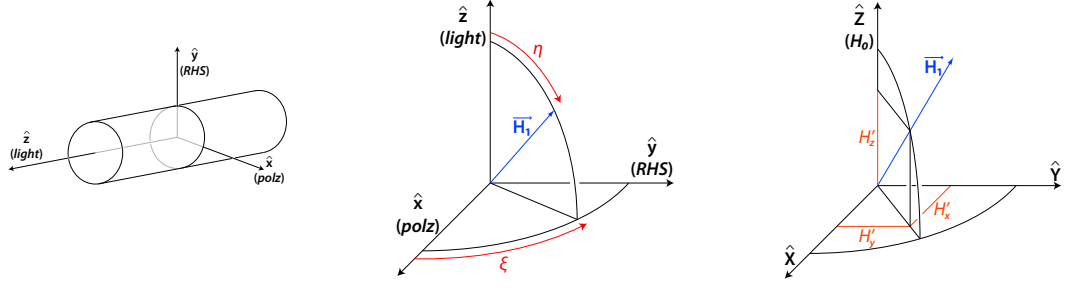


Figure 3.18. Magnetic Field Orientation in Local and World Systems.

Recall the world-local transform of Figure 3.1. Because the equations will not distinguish  $\theta$  and  $\xi$  in this section, it is prudent to define  $\Theta \equiv \theta + \xi$ . Then the field (see Appendix B.2) in the world system is given by:

$$\vec{\mathbf{H}} = 2H_1 \cos \omega t \begin{bmatrix} H'_x \\ H'_y \\ H'_z \end{bmatrix} + \begin{bmatrix} 0 \\ 0 \\ H_0 \end{bmatrix}, \quad \begin{bmatrix} H'_x \\ H'_y \\ H'_z \end{bmatrix} \equiv \begin{bmatrix} \sin \eta \cos \Theta \\ \sin \eta \sin \Theta \cos \phi - \cos \eta \sin \phi \\ \sin \eta \sin \Theta \sin \phi + \cos \eta \cos \phi \end{bmatrix} \quad (3.33)$$

Keep in mind that these are direction cosines:  $H_x'^2 + H_y'^2 + H_z'^2 = 1$ . We are now in a position to approximate:

$$\begin{aligned} H_- &= H_1 \cos \omega t \left[ H'_x + iH'_y \right] && \approx \frac{H_1}{2} e^{-i\omega t} \left[ H'_x + iH'_y \right] \\ H_+ &= H_1 \cos \omega t \left[ H'_x - iH'_y \right] && \approx \frac{H_1}{2} e^{i\omega t} \left[ H'_x - iH'_y \right] \\ H_z &= 2H_1 \cos \omega t \left[ H'_z \right] + H_0 \end{aligned} \quad (3.34)$$

This is equivalent to saying:

$$\begin{bmatrix} H_x \\ H_y \end{bmatrix} = 2H_1 \begin{bmatrix} H'_x & 0 \\ H'_y & 0 \end{bmatrix} \begin{bmatrix} \cos \omega t \\ \sin \omega t \end{bmatrix} \approx H_1 \begin{bmatrix} H'_x & -H'_y \\ H'_y & H'_x \end{bmatrix} \begin{bmatrix} \cos \omega t \\ \sin \omega t \end{bmatrix}$$

Notice that  $H_z$  is not approximated, and that the quadrature  $\sin \omega t$  component is perpendicular to the  $\hat{\mathbf{Z}}$  direction. It should also be apparent that the  $\cos \omega t$  term's direction has not been affected by the approximation. Finally, note that the  $\cos \omega t$  and  $\sin \omega t$  columns are orthogonal (but not orthonormal). The situation is shown in Figure 3.19.

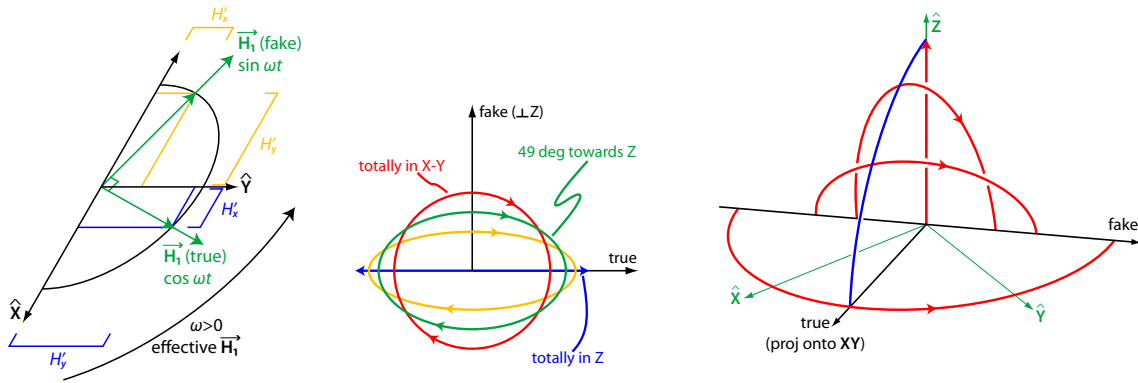


Figure 3.19. Orientation of Quadrature Field After Approximation.

Take a moment to try to understand the geometry there. The leftmost drawing shows the situation when there is no  $\hat{Z}$  component to  $H_1$ , so we just get a circular rotation in the plane. The rightmost drawing shows what the ellipses look like as the plane of  $H_1$  rotates towards  $\hat{Z}$ : there is less of a component along  $\hat{X}$  or  $\hat{Y}$ . The projection into the  $\hat{X}$ - $\hat{Y}$  plane is always circular, but the actual figure traced by the presumed  $H_1$  goes from circular to elliptical to linear. Staying in that plane and tracing over previous figures, we get the middle drawing.

We now check if the approximation makes sense by checking some limiting cases. We really only need to examine cases where the local and world systems are aligned in one fixed fashion with respect to each other, as the orientation of the light does not figure into the approximation. Therefore, in Figure 3.20, I have shown 3 of these limiting cases with the local and world systems totally aligned, as well as a (superfluous) example of what it might look like if the two systems were not the same.

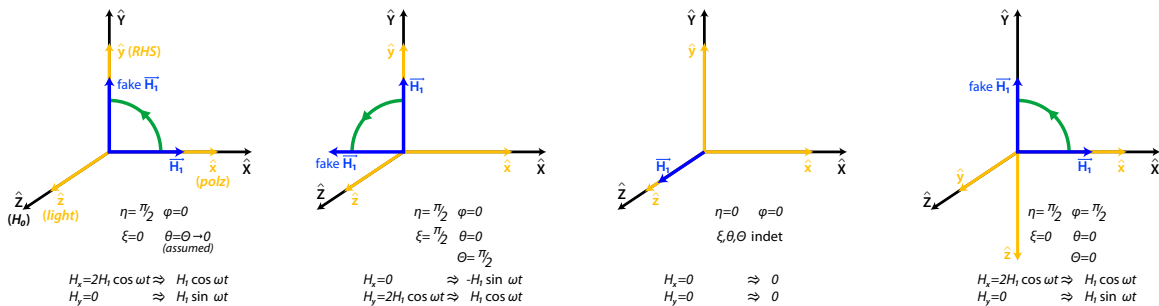


Figure 3.20. Some Example Orientations of the Magnetic Fields.

When we take  $H_1$  to be in the  $\hat{\mathbf{x}}$  direction, with both coordinate systems aligned, as the situation usually is, this gives  $\eta = \frac{\pi}{2}$ ,  $\phi = 0$  and  $\theta$  undetermined, but we can still conclude that  $\Theta = 0$ , by assuming  $\xi$  compensates any choice of  $\theta$ , which is to say that we choose  $H_1$  along the world  $\hat{\mathbf{X}}$  axis. From that, we recover the nominal MSP model of [34]. Even if we add an excess to  $\xi$ , thereby adjusting  $\Theta$ , we just get an in-plane rotation, so this is encouraging.

If we instead took  $H_1$  along  $H_0$ , but otherwise kept a nominal aligned system of  $\theta = \phi = 0$ , then  $\eta = 0$ ,  $\xi$  is indeterminate, and therefore  $\Theta$  is indeterminate. This gives  $H_1$  entirely along  $\hat{\mathbf{Z}}$ , which is not even an approximation. Therefore, with the nominal aligned coordinate system, we have a good approximation at the two limiting points. Since it varies smoothly between the two extremes, it is a good approximation in the aligned system. Due to the way the approximation is constructed, it is good in unaligned systems, as well.

### 3.8.3 Compilation of Magnetic Evolution Equations

Substituting Equations (3.34) back into Equation (3.32):

$$\left(\frac{d\vec{\mathbf{v}}}{dt}\right)_M = \left[ i(\gamma H_0 + 2H_1\gamma H'_z \cos \omega t) \mathbf{A}_3 + \frac{i\gamma H_1}{2} \mathbf{A}_4 \right] \vec{\mathbf{v}}, \quad \mathbf{A}_4 \equiv \left[ \begin{array}{c|c} \mathbf{A}_4^{(1)} & \mathbf{0} \\ \hline \mathbf{0} & \mathbf{A}_4^{(2)} \end{array} \right], \quad (3.35)$$

where  $\mathbf{A}_3 \equiv \text{diag} [1 \ 0 \ -1 \ | \ 2 \ 1 \ 0 \ -1 \ -2]$ ,  $\text{diag}$  is the operator that puts an  $n$ -element vector onto the main diagonal of a diagonal  $n \times n$  matrix, and where  $\mathbf{A}_4$  has been split into rank one and rank two portions, respectively:

$$\mathbf{A}_4^{(1)} = \begin{bmatrix} 0 & 2(-H'_x - iH'_y)e^{i\omega t} & 0 \\ (-H'_x + iH'_y)e^{-i\omega t} & 0 & (H'_x + iH'_y)e^{i\omega t} \\ 0 & 2(H'_x - iH'_y)e^{-i\omega t} & 0 \end{bmatrix},$$

$$\mathbf{A}_4^{(2)} = \begin{bmatrix} 0 & 2(H'_x + iH'_y)e^{i\omega t} & 0 & 0 & 0 \\ 2(H'_x - iH'_y)e^{-i\omega t} & 0 & \sqrt{6}(H'_x + iH'_y)e^{i\omega t} & 0 & 0 \\ 0 & \sqrt{6}(H'_x - iH'_y)e^{-i\omega t} & 0 & \sqrt{6}(H'_x + iH'_y)e^{i\omega t} & 0 \\ 0 & 0 & \sqrt{6}(H'_x - iH'_y)e^{-i\omega t} & 0 & 2(H'_x + iH'_y)e^{i\omega t} \\ 0 & 0 & 0 & 2(H'_x - iH'_y)e^{-i\omega t} & 0 \end{bmatrix}.$$

To properly account for the oscillating, rather than rotating, field (i.e., avoid the Bloch-Siegert shift), at the expense of having to compute the solution numerically, simply replace the  $e^{\pm i\omega t}$  in  $\mathbf{A}_4$  with  $2 \cos \omega t$ , as one could easily determine from Equations (3.34).

In anticipation of what is to come, we define the substitutions (not yet approximations):

$$\langle \mathbf{J}_z \rangle = \langle \tilde{\mathbf{J}}_z \rangle, \quad \langle \mathbf{J}_+ \rangle = \langle \tilde{\mathbf{J}}_+ \rangle e^{i\omega t}, \quad \langle \mathbf{T}_2^{(2)} \rangle = \langle \tilde{\mathbf{T}}_2^{(2)} \rangle e^{2i\omega t}, \quad \langle \mathbf{T}_1^{(2)} \rangle = \langle \tilde{\mathbf{T}}_1^{(2)} \rangle e^{i\omega t}, \quad \langle \mathbf{T}_0^{(2)} \rangle = \langle \tilde{\mathbf{T}}_0^{(2)} \rangle \quad (3.36)$$

By the properties of the angular momentum operators, we can also deduce that:

$$\langle \mathbf{J}_- \rangle = \langle \tilde{\mathbf{J}}_- \rangle e^{-i\omega t}, \quad \langle \mathbf{T}_{-2}^{(2)} \rangle = \langle \tilde{\mathbf{T}}_{-2}^{(2)} \rangle e^{-2i\omega t}, \quad \langle \mathbf{T}_{-1}^{(2)} \rangle = \langle \tilde{\mathbf{T}}_{-1}^{(2)} \rangle e^{-i\omega t}. \quad (3.37)$$

Substituting these, we obtain:

$$\left( \frac{d\vec{\mathbf{v}}'}{dt} \right)_M = \left[ i(\gamma H_0 - \omega + 2H_1 \gamma H'_z \cos \omega t) \mathbf{A}_3 + \frac{i\gamma H_1}{2} \mathbf{A}_{4'} \right] \vec{\mathbf{v}}', \quad (3.38)$$

$$\text{where } \vec{\mathbf{v}}' \equiv \begin{bmatrix} \langle \tilde{\mathbf{J}}_+ \rangle \\ \langle \tilde{\mathbf{J}}_z \rangle \\ \langle \tilde{\mathbf{J}}_- \rangle \\ \langle \tilde{\mathbf{T}}_2^{(2)} \rangle \\ \langle \tilde{\mathbf{T}}_1^{(2)} \rangle \\ \langle \tilde{\mathbf{T}}_0^{(2)} \rangle \\ \langle \tilde{\mathbf{T}}_{-1}^{(2)} \rangle \\ \langle \tilde{\mathbf{T}}_{-2}^{(2)} \rangle \end{bmatrix}, \quad \mathbf{A}_{4'}^{(2)} = \begin{bmatrix} 0 & 2(H'_x + iH'_y) & 0 & 0 & 0 \\ 2(H'_x - iH'_y) & 0 & \sqrt{6}(H'_x + iH'_y) & 0 & 0 \\ 0 & \sqrt{6}(H'_x - iH'_y) & 0 & \sqrt{6}(H'_x + iH'_y) & 0 \\ 0 & 0 & \sqrt{6}(H'_x - iH'_y) & 0 & 2(H'_x + iH'_y) \\ 0 & 0 & 0 & 2(H'_x - iH'_y) & 0 \end{bmatrix},$$

$$\mathbf{A}_{4'}^{(1)} = \begin{bmatrix} 0 & 2(-H'_x - iH'_y) & 0 \\ -H'_x + iH'_y & 0 & H'_x + iH'_y \\ 0 & 2(H'_x - iH'_y) & 0 \end{bmatrix}, \quad \text{and } \mathbf{A}_{4'} \equiv \left[ \begin{array}{c|c} \mathbf{A}_{4'}^{(1)} & \mathbf{0} \\ \mathbf{0} & \mathbf{A}_{4'}^{(2)} \end{array} \right].$$

It is possible to assign different  $\omega$ 's to the two different ranks, but it can be shown that resonance occurs at  $\omega \sim \gamma H_0$  in both cases, so such a generalization has no benefit. Note that  $\mathbf{A}_3$  is invariant under this transformation, and that  $\mathbf{A}_4 \rightarrow \mathbf{A}_{4'}$  is a simplification. Unfortunately,  $\mathbf{A}_1$  and  $\mathbf{A}_2$  would not be simplified, but the transformation is all or nothing, and the transformation will be beneficial if the hypothesis that  $\langle \tilde{\mathbf{T}}_0^{(2)} \rangle$  and  $\langle \tilde{\mathbf{J}}_z \rangle$  are quasistatic holds up, the latter of which is assumed in [34].

$\mathbf{A}_{4'}$  is displayed here without taking into account the Bloch-Siegert shift, but the shift can be dealt with by multiplying the superdiagonal elements by  $1 + e^{-2i\omega t}$ , and multiplying the subdiagonal elements by  $1 + e^{2i\omega t}$ . Again, doing this precludes an analytical solution.

## 3.9 Doppler Broadening

Table 3.7. Symbols Introduced In Section 3.9

Symbol	Units	Description
$G(\omega')$	—	Doppler-broadened $F(\omega')$
$G'(\omega')$	—	Doppler-broadened $F'(\omega')$
$\Omega'_{0d}, \omega'_{0d}$	rad/s	Random variable and outcome representing apparent transition frequency at a given velocity
$\mathcal{V}, v$	cm/s	Random variable and outcome for atomic velocity, projected on $\hat{\mathbf{z}}$
$\sigma_\omega$	rad/s	Standard deviation of doppler shift
$\sigma_v$	cm/s	Standard deviation of projection of atomic velocity
$k_B T$	erg	Boltzmann constant times absolute temperature
$\delta$	rad/s	$\sigma_\omega \sqrt{2}$ (following convention of [34])

Many texts, e.g., [38], present derivations of Doppler broadening kernels, and describe the required process of convolving with the original distribution function. We are interested in both initial distributions  $F(\omega')$  and  $F'(\omega')$ , where the former is Lorentzian. The convolution of the Gaussian kernel with a Lorentzian is the Voigt profile, but the convolution integral cannot be evaluated in closed form. A similar consideration applies to the dispersive counterpart  $F'(\omega')$ . The lifetime of the  $2^3P_j$  states is sufficiently long that, for the entire temperature range where helium remains a gas, one can make good approximations for the Doppler broadening of the  $D_{0,1,2}$  lines of  $^4\text{He}$ . This section elaborates on some notes from Douglas D. McGregor [36], and plots the quality of the approximations at a few temperatures.

In order to account for atomic velocity, we begin by rewriting Equation (3.23) with an *effective* center frequency  $\omega_{0d}$ :

$$F(\omega') = \frac{2}{1 + \tau^2 (\omega' - \omega'_{0d})^2} \quad F'(\omega') = \frac{2i\tau (\omega' - \omega'_{0d})}{1 + \tau^2 (\omega' - \omega'_{0d})^2}$$

where the random variable  $\Omega_{0d} \sim \mathcal{N}(\omega'_0, \sigma_\omega^2)$ , with the mean taken as the point of zero velocity by symmetry considerations. There is a one-to-one relationship between  $\omega_{0d}$  and the  $\hat{\mathbf{z}}$  projection of the velocity of a particular atom, given by  $v$ , where this velocity is a random variable  $\mathcal{V} \sim \mathcal{N}(0, \sigma_v^2)$ , with  $\sigma_v^2 = k_B T / M$ , as given in [38]. The doppler shift is given by the linear transformation of

random variables  $(\Omega'_{0d} - \omega'_0)c = \omega'_0\mathcal{V}$ , which allows us to trivially relate the standard deviations:  $\sigma_{\omega c} = \omega'_0\sigma_v$ .

Over the entire range of atomic velocities, and therefore apparent transition frequencies  $\omega'_{0d}$ , we can find the expectation value of the lineshape factor  $F(\omega')$ :

$$\begin{aligned} E[F(\omega')] &= \int_0^\infty f_{\Omega'_{0d}}(\omega'_{0d}) \frac{2}{1 + \tau^2 (\omega' - \omega'_{0d})^2} d\omega'_{0d} \approx \int_0^\infty f_{\Omega'_{0d}}(\omega'_{0d}) \frac{2\pi}{\tau} \delta(\omega' - \omega'_{0d}) d\omega'_{0d} \\ &= \frac{2\pi}{\tau} f_{\Omega'_{0d}}(\omega') = \frac{\sqrt{2\pi}}{\tau\sigma_\omega} \exp\left[-\frac{(\omega' - \omega'_0)^2}{2\sigma_\omega^2}\right] = \frac{2\sqrt{\pi}}{\tau\delta} \exp\left[-\frac{(\omega' - \omega'_0)^2}{2\sigma_\omega^2}\right], \quad \delta \equiv \sigma_\omega \sqrt{2} \end{aligned}$$

where the definition of the constant  $\delta$  follows [34]. The approximation is justified since the HWHM of the Lorentzian  $F(\omega')$  is about  $10^7$  rad/s, and the HWHM of the Gaussian is  $\delta\sqrt{\ln 2} \approx 5.4 \times 10^9$  at 300 K, almost three orders of magnitude wider. At this temperature, the approximation yields linewidths accurate to about a tenth of a percent, and, at the boiling point of helium, the approximation is still better than one percent. We define  $G(\omega') \equiv E[F(\omega')]$ , as given. Note that a closed form of the integral is unavailable.

Likewise, we find that:

$$E[F'(\omega')] = \int_0^\infty f_{\Omega'_{0d}}(\omega'_{0d}) F'(\omega'_{0d}) = \frac{i\sqrt{2}}{\tau\sigma_\omega\sqrt{\pi}} \int_0^\infty \frac{\tau^2 (\omega' - \omega'_{0d})}{1 + \tau^2 (\omega' - \omega'_{0d})^2} \exp\left[-\frac{(\omega'_{0d} - \omega'_0)^2}{2\sigma_\omega^2}\right] d\omega'_{0d}$$

Now [1] gives on pages 303 and 297, respectively:

$$\begin{aligned} \int_{-\infty}^\infty \frac{(x-t)e^{-t^2}}{(x-t)^2 + y^2} dt &= \pi \operatorname{Im}\{w(x+iy)\} \quad x \text{ real, } y > 0 \\ w(z) &= e^{-z^2} \operatorname{erfc}(-iz) \end{aligned}$$

If we identify:

$$x = \frac{\omega' - \omega'_0}{\sigma_\omega \sqrt{2}} \quad t = \frac{\omega'_{0d} - \omega'_0}{\sigma_\omega \sqrt{2}} \quad y = \frac{1}{\sigma_\omega \tau \sqrt{2}} \quad \frac{d\omega'_{0d}}{\sigma_\omega \sqrt{2}} = dt,$$

then the integrals match, other than the question of limits. It is somewhat absurd to think that the Doppler effect will cause any noticeable contributions at *negative* frequencies, so it is reasonable to extend the limits and equate the two:

$$\begin{aligned} E[F'(\omega')] &= \left[ \frac{i\sqrt{2}}{\tau\sigma_\omega\sqrt{\pi}} \right] [\pi \operatorname{Im}\{w(x+iy)\}] = \frac{i2\sqrt{\pi}}{\tau\delta} \operatorname{Im}\left\{ \operatorname{erfc}(y-ix) e^{y^2-x^2-2ixy} \right\} \\ &= \frac{i2\sqrt{\pi}}{\tau\delta} e^{-y^2-x^2} [\cos 2xy \operatorname{Im}\{\operatorname{erf}(ix-y)\} - \sin 2xy (1 + \operatorname{Re}\{\operatorname{erf}(ix-y)\})] \end{aligned}$$

For very small  $y$  (measured absolutely, not relative to  $x$ ), it is reasonable to take  $y = 0$ . The relative error involved in doing this is about a quarter of a percent, at worst, given that  $y \approx 1.54 \times 10^{-3}$ . Therefore:

$$G'(\omega') \equiv E[F'(\omega')] \approx \frac{i2\sqrt{\pi}}{\tau\delta} e^{-x^2} \text{Im}\{\text{erf}(ix)\} = \frac{2\sqrt{\pi}}{\tau\delta} \exp\left[-\frac{(\omega' - \omega'_0)^2}{\delta^2}\right] \text{erf}\left[\frac{i(\omega' - \omega'_0)}{\delta}\right]$$

Replacing  $F'(\omega')$  and  $F(\omega')$  by their expectation values is equivalent to replacing them by  $G'(\omega')$  and  $G(\omega')$ , respectively, everywhere they occur in this document, save this section.

$G(\omega')$  and  $G'(\omega')$  are plotted in Figures 3.21 and 3.23, respectively. Note that  $F'(\omega')$  and  $G'(\omega')$  are odd and pure imaginary, while  $F(\omega')$  and  $G(\omega')$  are even and real. Note also that the “tails” of  $G'(\omega')$  contribute far beyond where  $G(\omega')$  ceases to contribute; this means that cross sections involving the former, but on distant spectral lines, often contribute. This is the case with the virtual light shift, which is not quite zero on the center of the  $D_0$  line, due to contributions from the other two lines. An idea of the error introduced with our approximations can be seen in Figures 3.22 and 3.24. It is very small, as mentioned earlier. The temperatures were chosen to be related by a factor of 4, with 300 K being approximately room temperature.

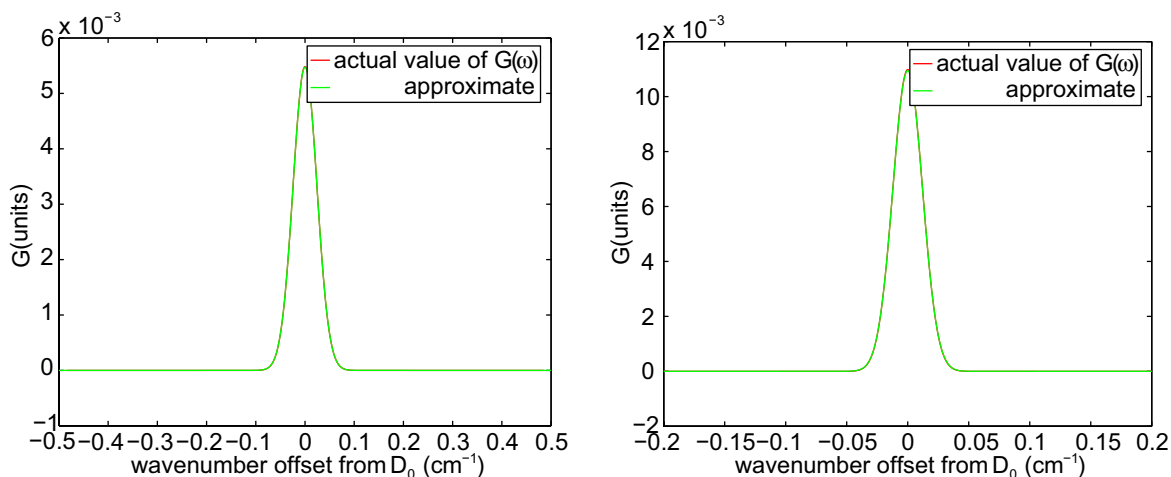


Figure 3.21.  $G(\omega')$  Approximation Comparison, Overlay. The left figure is at 300 K, and the right figure is at 75 K.

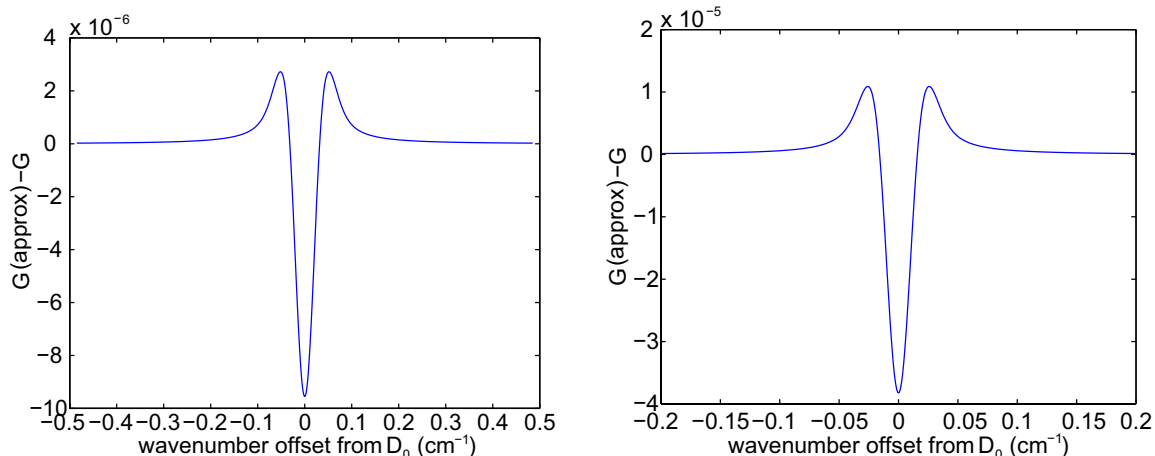


Figure 3.22.  $G(\omega')$  Approximation Comparison, Difference. The left figure is at 300 K, and the right figure is at 75 K.

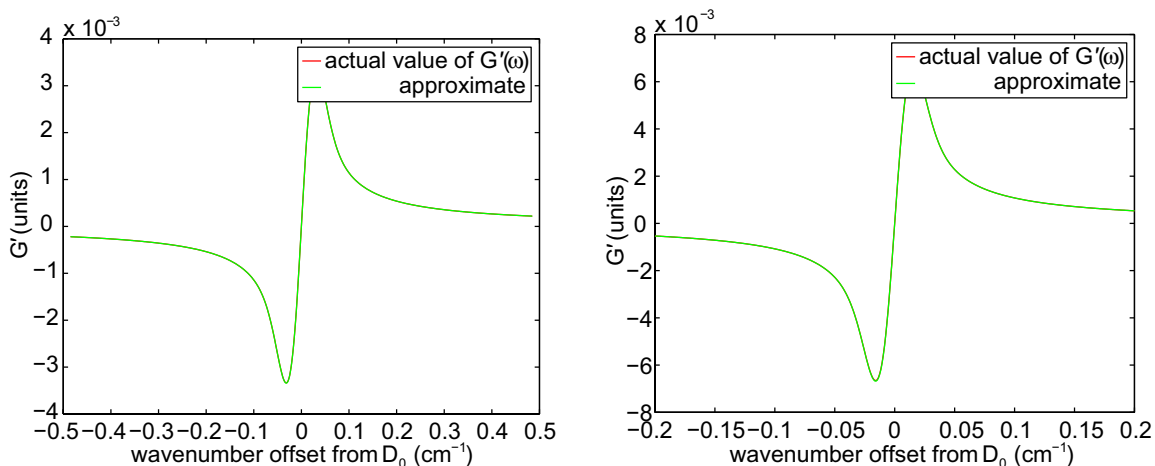


Figure 3.23.  $G'(\omega')$  Approximation Comparison, Overlay. The left figure is at 300 K, and the right figure is at 75 K.

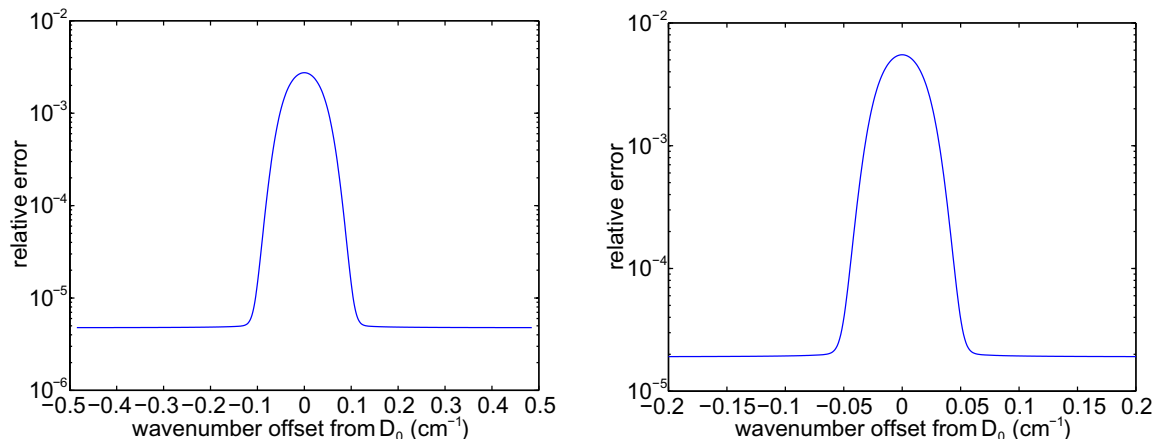


Figure 3.24.  $G'(\omega')$  Approximation Comparison, Relative Error. The left figure is at 300 K, and the right figure is at 75 K.

## 3.10 State Space Form

Table 3.8. Symbols Introduced In Section 3.10

Symbol	Units	Description
$\tau_c$	s	Polarization relaxation time constant
$\alpha'(z)$	$\text{cm}^{-1}\text{rad}^{-1}\text{s}$	Photons gained per length per optical angular frequency
$\Phi_{\text{IN}}$	$\text{cm}^{-2}\text{s}^{-1}$	Photon flux density at input to cell, $\Phi(0)$
$\mathbf{A}_{1'}, \mathbf{A}_{2'}, \mathbf{C}_{1'}, \mathbf{C}_{p'}, \vec{\mathbf{a}}_{p'}$	$\text{erg}^2\text{cm}^3\text{s}^2$	Rotating-system versions, and summed over $D_0, D_1, D_2$

This section adds all previous terms in a digestible form and completes the transformation to a rotating coordinate system, in preparation for solution.

Combining Equations (3.28) and (3.35) with a polarization relaxation term [34], followed by the substitutions of Section 3.9 ( $F \rightarrow G$  and  $F' \rightarrow G'$ ), gives the following:

$$\begin{aligned} \frac{d\vec{\mathbf{v}}}{dt} = & \frac{\pi\Phi\omega'}{24c\hbar^2} \sum_{\omega'_0} [\tau G(\omega' - \omega'_0) \mathbf{A}_1 + \tau G'(\omega' - \omega'_0) \mathbf{A}_2] \vec{\mathbf{v}} - \frac{2\pi\Phi\omega'}{3c\hbar} \sum_{\omega'_0} \tau G(\omega' - \omega'_0) \vec{\mathbf{a}}_p \\ & + \left[ i(\gamma H_0 + 2H_1\gamma H'_z \cos \omega t) \mathbf{A}_3 + \frac{i\gamma H_1}{2} \mathbf{A}_4(e^{i\omega t}) - \frac{\mathbf{I}_{8 \times 8}}{\tau_c} \right] \vec{\mathbf{v}} \end{aligned} \quad (3.39)$$

where  $\mathbf{I}_{8 \times 8}$  is the  $8 \times 8$  identity matrix.

Here,  $\mathbf{A}_1$  and  $\mathbf{A}_2$  are polarization-dependent,  $\mathbf{A}_3$  is constant, and  $\mathbf{A}_4$  is a function of small integer powers of  $e^{i\omega t}$ , as partially indicated. The precise treatment of  $\tau_c$  warrants further thought, however it is beyond the scope of this research. To date, the discharge model<sup>8</sup> that gives  $\tau_c$  depends on metastable density, overall pressure, and cell dimensions, giving an “average” value of  $\tau_c$  that includes the effects of diffusion, electron temperature, radiation trapping, and various rate equations for excited atoms, ionized atoms, electrons, and ionized diatomic species. It assumes homogeneous time-invariant discharge populations and a noiseless electrical stimulus from the RF exciter.  $\Phi\omega'$  is related to light intensity (but not wavelength, in spite of the appearance of  $\omega'$ ). It remains to be determined whether it makes sense to convert some of the  $\mathbf{A}$  matrices into nonlinear exogenous inputs  $\mathbf{B}$ 's, primarily as functions of  $\Phi(0)$ ,  $\omega'$ , and  $\omega$ .

<sup>8</sup>Douglas D. McGregor, source code, September 19, 2007

The justification for  $\tau_c$  being the same for every component is that relaxations are thought to simply remove metastables entirely, without regard to polarization of the atoms. Two significant relaxation effects that contribute to  $\tau_c$  are an electron striking a  $2^3S_1$  atom and exciting it to a random  $2^3P_J$  state, destroying any polarization [37], and diffusion of  $2^3S_1$  atoms into the walls [24]. Penning ionization is an atomic polarization-dependent process [24, 33] where two  $2^3S_1$  atoms collide yielding a ground-state  $1^1S_0$  atom, a singly-ionized atom, and an electron, and is considered in the calculation of  $\tau_c$  primarily because it affects the electron density. However, the polarization dependence of Penning ionization is ignored, partly because the polarization is small, and partly because the model would need a feedback between the discharge calculations and the optical pumping calculations. Such a modification, even if tractable, is not worth the difficulty, since the contribution is often considered weak compared to the other relaxation effects.

The virtual light shift (on the diagonal of  $\mathbf{A}_2$ ) has measurable effects far beyond the absorption line, as illustrated in Figure 3.23, so we must keep the summation, even though  $\omega'$  is only near the  $D_0$  value of  $\omega'_0$  in practice.

While solving this equation, it will be assumed  $H_0$  is a constant (in a constant direction), but it is conceivable that the simplistic direction assumption necessitated by perturbation theory might be tested by comparing a slowly oscillating coordinate system solution under this assumption with a fixed coordinate-system solution where the effective AC component of  $H_0$  is added as an additional term in a similar fashion to how  $H_1$  is handled. If this is feasible, the comparison will likely give two results that diverge as the frequency of the test-vector  $H_0$  grows, validating the adiabatic assumption for some low frequency range (likely  $\ll \omega$ ), up to some specification on tolerable model error. This is not to suggest that motion of  $H_0$  will usually be sinusoidal, but is a convenient test of accuracy, nevertheless.

The output equation can be obtained by taking Equation (3.29) and also applying the substitutions of Section 3.9:

$$\alpha(z) = \alpha'(z) \Phi \omega' = -\frac{\pi \Phi \omega'}{6c\hbar^3} n_S \sum_{\omega'_0} \tau G(\omega' - \omega'_0) (\mathbf{C}_1 \vec{\mathbf{v}} + \hbar \mathbf{C}_p), \quad \Phi(z) = \Phi_{\text{IN}} e^{\alpha'(z) \omega' z} \quad (3.40)$$

Note that this explicitly includes the frequency of the light. This appears unavoidable. At absorption levels of interest (15%-20%), we may choose to approximate the exponential with

a line [34]. At the opposite extreme, one accounts for the fact that light intensity, polarization and light broadening vary along the length of the cell, and one could consider treating the cell as several shorter cylinders stacked end-to-end, with the output of one feeding the input of the next. We elaborate on this “cell slicing” procedure in Section 3.11. Because the vapor is optically-thin under typical operating conditions, not many slices are needed, and neglecting to follow this procedure still yields results with the proper qualitative features.

### 3.10.1 Rotating Coordinates

One approach that at least sometimes causes the DC component of the solution to dominate  $\omega$  and its harmonics is to make a mathematical transformation to rotating coordinates. This is, in itself, not an approximation, but the approximations we eventually make will generally rely on this. Transforming Equation (3.39) to rotating coordinates, we obtain:

$$\frac{d\vec{v}'}{dt} = \left[ \frac{\pi\Phi\omega'}{24c\hbar^2} (\mathbf{A}_{1'} + \mathbf{A}_{2'}) + i(\gamma H_0 - \omega + 2H_1\gamma H'_z \cos \omega t) \mathbf{A}_3 + \frac{i\gamma H_1}{2} \mathbf{A}_{4'} - \frac{\mathbf{I}_{8 \times 8}}{\tau_c} \right] \vec{v}' - \frac{2\pi\Phi\omega'}{3c\hbar} \vec{a}_{p'}, \quad (3.41)$$

where

$$\vec{a}_{p'} = \sum_{\omega'_0} \tau G(\omega' - \omega'_0) \left[ \begin{array}{ccc|ccc} Q_+ e^{-i\omega t} & Q_z & Q_- e^{i\omega t} & Q_2 e^{-2i\omega t} & Q_1 e^{-i\omega t} & Q_0 & Q_{-1} e^{i\omega t} & Q_{-2} e^{2i\omega t} \end{array} \right]^T.$$

Note that the transpose in the definition of  $\vec{a}_{p'}$  is merely a page space saving device to change a row vector to a column vector; the component operators themselves are not transposed. For the same page size limit reasons, we define

$$\mathbf{A}_{12} \equiv \left[ \begin{array}{ccc|ccc} 1 & e^{-i\omega t} & e^{-2i\omega t} & e^{i\omega t} & 1 & e^{-i\omega t} & e^{-2i\omega t} & 0 \\ e^{i\omega t} & 1 & e^{-i\omega t} & e^{2i\omega t} & e^{i\omega t} & 1 & e^{-i\omega t} & e^{-2i\omega t} \\ e^{2i\omega t} & e^{i\omega t} & 1 & 0 & e^{2i\omega t} & e^{i\omega t} & 1 & e^{-i\omega t} \\ \hline e^{-i\omega t} & e^{-2i\omega t} & 0 & 1 & e^{-i\omega t} & e^{-2i\omega t} & 0 & 0 \\ 1 & e^{-i\omega t} & e^{-2i\omega t} & e^{i\omega t} & 1 & e^{-i\omega t} & e^{-2i\omega t} & 0 \\ e^{i\omega t} & 1 & e^{-i\omega t} & e^{2i\omega t} & e^{i\omega t} & 1 & e^{-i\omega t} & e^{-2i\omega t} \\ e^{2i\omega t} & e^{i\omega t} & 1 & 0 & e^{2i\omega t} & e^{i\omega t} & 1 & e^{-i\omega t} \\ 0 & e^{2i\omega t} & e^{i\omega t} & 0 & 0 & e^{2i\omega t} & e^{i\omega t} & 1 \end{array} \right],$$

and use this to specify

$$\begin{aligned}\mathbf{A}_{1'} &= \sum_{\omega'_0} \tau G(\omega' - \omega'_0) [\mathbf{A}_{12} (.*) \mathbf{A}_1] \quad \text{and} \\ \mathbf{A}_{2'} &= \sum_{\omega'_0} \tau G'(\omega' - \omega'_0) [\mathbf{A}_{12} (.*) \mathbf{A}_2],\end{aligned}$$

where  $(.*)$  is element-by-element matrix multiplication.

Finally, one can also transform the output equation, Equation (3.40), to rotating coordinates:

$$\alpha(z) = -\frac{\pi\Phi\omega'}{6c\hbar^3} n_S (\mathbf{C}_{1'} \vec{\mathbf{v}}' + \hbar C_{p'}), \quad (3.42)$$

where

$$\begin{aligned}\mathbf{C}_{1'} &= \sum_{\omega'_0} \tau G(\omega' - \omega'_0) \\ &\times \begin{bmatrix} 3Q_- e^{i\omega t} & 6Q_z & 3Q_+ e^{-i\omega t} & | & 12Q_{-2} e^{2i\omega t} & -12Q_{-1} e^{i\omega t} & 12Q_0 & -12Q_1 e^{-i\omega t} & 12Q_2 e^{-2i\omega t} \end{bmatrix},\end{aligned}$$

and  $C_{p'} = \sum_{\omega'_0} 4Q_I \tau G(\omega' - \omega'_0)$ .

### 3.11 Cell Slicing

This section presents details of an approach briefly mentioned in [34] for handling longitudinal variation of light intensity in the cell and compares the quality of the theoretical results, depending on how many slices the cell is conceptually divided into.

It was mentioned in the explanation of Equation (3.27) that optical pumping causes the ensemble statistics to vary along the length of the cell. The variation is not very large, so it makes sense to treat the problem as a number of shorter cells stacked end-to-end, each solved with the previous cell's output power becoming the new input power. The choice of the number of slices has an impact on the amount of error. In this section, we will illustrate a quantitative example of the effect of this choice for the configuration described in Section 4.1, which should also be similar to the results one would obtain with the solution given in [34]. The code used is based on the solution in Chapter 5. The results here are assumed to be representative of those in other configurations.

Perhaps most simple is the case when  $H_1 = 0$ , or, equivalently,  $|\gamma H_0 - \omega| \rightarrow \infty$ . In this case, shown in Figure 3.25, we are looking at the off-resonance transmitted light, and the effect of optical

pumping on the transparency of the cell is highlighted. The computational time is proportional to the number of sub-cells, or “slices,” used. Use of only 1 slice is sometimes referred to here as “unsliced,” since it is the result one would obtain if this section had not been included. The plots in this section use 1.5 torr, 1.805 cm inside-radius, 4.88 cm inside-length cells, and the results are representative of other sizes.

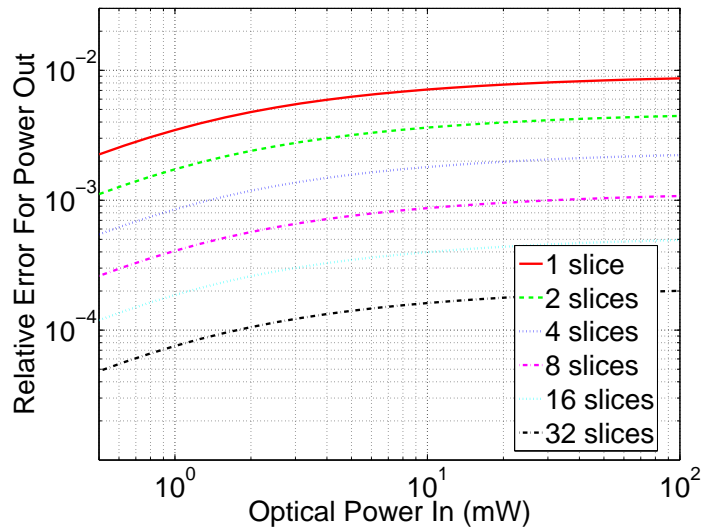


Figure 3.25. Effect of Slice Count, Off-Resonance ( $H_1 = 0$ ).

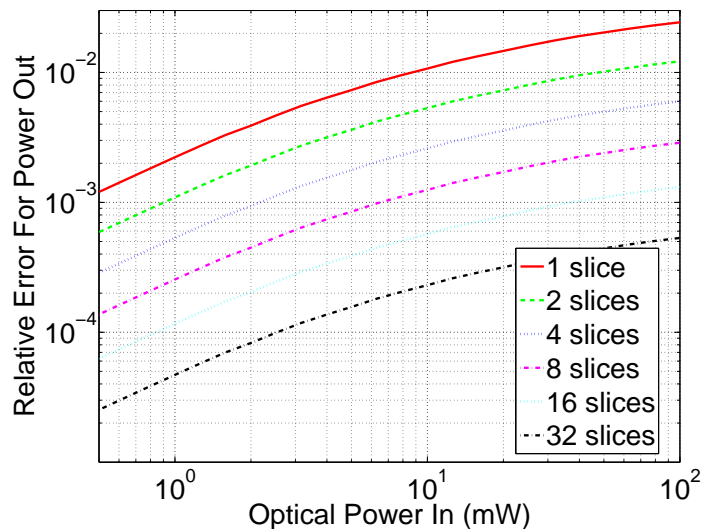


Figure 3.26. Effect of Slice Count,  $\gamma H_0 = \omega$ ,  $H_1$  Optimized for Each Power.

When  $H_1$  is optimized for each power level, and  $\omega = \gamma H_0$ , we have the on-resonance case shown in Figure 3.26. Note that the error continues to increase as power increases, rather

than the apparent leveling-off displayed in Figure 3.25. Note that, in both figures, the traces are approximately equally spaced on a logarithmic vertical scale, and that the number of traces has been chosen to increase exponentially. Both figures use 100 slices (not shown, as it would simply be a flat line at an ordinate of 0) as the “true” solution against which each option is compared, since an analytic solution to the slicing problem is not readily available.

Next, the resonance curve for a given metastable density (chosen to give 15% absorption with 100 slices) is shown in Figure 3.27. There is clearly a noticeable difference between these traces. One of the cases considered is five slices, as that is the number most frequently used in much of this document.

However, most of the error of Figure 3.27 can be attributed to improper absorption level, or, equivalently, failing to adjust the metastable density. If we instead allow each trace to have its own metastable density, thereby *constructing* solutions that each work out to 15% absorption, the difference is much smaller, as shown in Figure 3.28. The difference between 5 and 32 slices is unnoticeable on the scale of Figure 3.28. Since we generally use the absorption level to determine the metastable density, Figure 3.28 is most representative of the errors we expect to see in the remainder of this document, thus justifying the common choice of 5 slices. The input power was 1 mW in both figures.

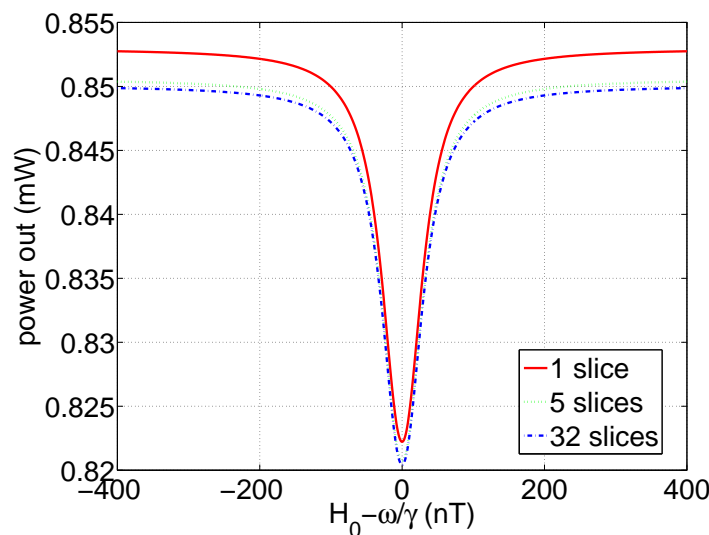


Figure 3.27. Effect of Slice Count, Resonance Curve,  $n_s$  Chosen to give 15% in One Case.

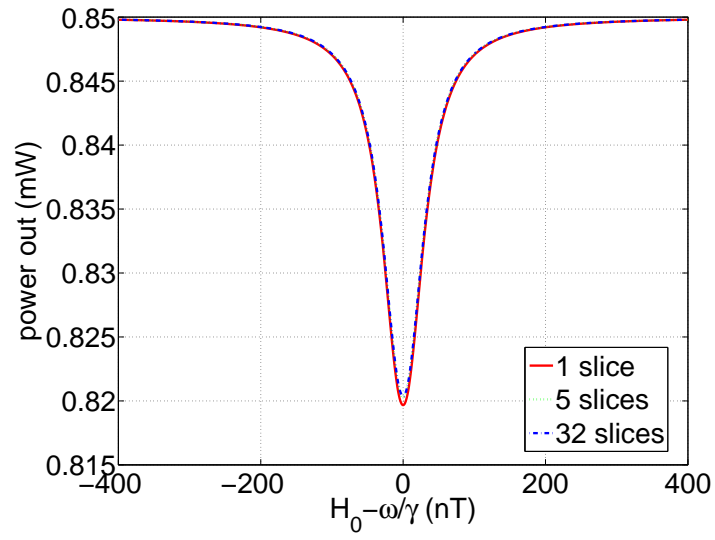


Figure 3.28. Effect of Slice Count, Resonance Curve,  $n_s$  Chosen to give 15% in Each Case

CHAPTER 4  
SPECIAL-CASE SOLUTIONS

Table 4.1. Symbols Introduced In Chapter 4 (Intro Only)

Symbol	Units	Description
$k_1, k_2$	$\text{erg}^{-2}\text{cm}^{-3}\text{s}^{-3}$	coefficients of $\mathbf{A}_{1'}$ , $\mathbf{A}_{2'}$ in state equation (identical values)
$k_3$	rad/s	coefficient of $\mathbf{A}_3$ ; detuning of $H_1$ frequency from $\gamma H_0$
$k_4$	rad/s	coefficient of $\mathbf{A}_{4'}$ in state equation; proportional to $H_1$ amplitude
$Q_{B1}$	$\text{cm}^2$	longitudinal light broadening cross section
$Q_{B2}$	$\text{cm}^2$	transverse light broadening cross section
$Q_P$	$\text{cm}^2$	rank-one polarization cross section
$Q_P^{(20)}, Q_P^{(22)}$	$\text{cm}^2$	polarization cross sections for $\langle \tilde{\mathbf{T}}_0^{(2)} \rangle$ and $\langle \tilde{\mathbf{T}}_{\pm 2}^{(2)} \rangle$ , respectively
$Q_S$	$\text{cm}^2$	virtual light shift cross section
$Q_{C0}$	$\text{cm}^2$	dispersive coupling cross section between rank one and rank two
$Q_M^{(20)}$	$\text{cm}^2$	dichroic monitoring cross section for $\langle \tilde{\mathbf{T}}_0^{(2)} \rangle$
$Q_A$	$\text{cm}^2$	absorption cross section

This section solves the state equations for a few of the orientations and optical polarizations of interest in practical magnetometers and describes a useful approximation for parameterizing resonance curves.

To allow the following to fit better onto the page, we define the coefficients of  $\mathbf{A}_{1'}$  through  $\mathbf{A}_{4'}$  to be  $k_1$  through  $k_4$ , respectively. For the purposes of the special-case solutions, we also neglect the  $\cos \omega t$  term of Equation (3.41) (by assuming  $H'_z = 0$ , or, equivalently,  $H_1 \perp H_0$ ), and we neglect the Bloch-Siegert shift (by assuming we have a true rotating  $H_1$  field, rather than the experimentally-convenient oscillating field). Then  $k_1 = k_2 = \frac{\pi\Phi\omega'}{24c\hbar^2}$ ,  $k_3 = i(\gamma H_0 - \omega)$ , and  $k_4 = \frac{i\gamma H_1}{2}$ . Then Equation (3.41) becomes:

$$\frac{d\vec{\mathbf{v}}'}{dt} = \left[ k_1\mathbf{A}_{1'} + k_2\mathbf{A}_{2'} + k_3\mathbf{A}_3 + k_4\mathbf{A}_{4'} - \tau_c^{-1}\mathbf{I}_{8 \times 8} \right] \vec{\mathbf{v}}' - 16\hbar k_1 \vec{\mathbf{a}}_{p'}$$

It is helpful to define some cross sections in a manner consistent with [34], but in terms of the quantities used in this document:

$$\begin{aligned}
-\Phi Q_{B2} &= k_1 \sum_{\omega'_0} \tau G(\omega' - \omega'_0) (-6Q_{+-}) , & -\Phi Q_{B1} &= k_1 \sum_{\omega'_0} \tau G(\omega' - \omega'_0) (-24Q_{zz}) , \\
\Phi Q_P &= k_1 \sum_{\omega'_0} \tau G(\omega' - \omega'_0) (-16Q_z) , & \Phi Q_P^{(20)} &= k_1 \sum_{\omega'_0} \tau G(\omega' - \omega'_0) (-16Q_0) , \\
\Phi Q_P^{(22)} &= k_1 \sum_{\omega'_0} \tau G(\omega' - \omega'_0) (-16Q_2) , & i\Phi Q_S &= k_2 \sum_{\omega'_0} \tau G'(\omega' - \omega'_0) (12Q_z) , \\
\Phi Q_{C0} &= k_2 \sum_{\omega'_0} \tau G'(\omega' - \omega'_0) (-6\sqrt{6}Q_0) , & -\Phi Q_M^{(20)} &= k_1 \sum_{\omega'_0} \tau G(\omega' - \omega'_0) (48Q_0) , \text{ and} \\
\Phi Q_A &= k_1 \sum_{\omega'_0} \tau G(\omega' - \omega'_0) (16Q_I) , & &
\end{aligned}$$

where the  $Q$ 's are, in order of introduction, the transverse light broadening cross section<sup>9</sup>, the longitudinal light broadening cross section, the rank-one polarization cross section, two different rank-two polarization cross sections, the virtual light shift cross section, a cross section for the coupling of the rank one and rank two portions, the dichroic monitoring cross section for the rank two longitudinal polarization, and the absorption cross section (which is independent of atomic polarization). Note that  $Q_S$  is real because  $G'(\omega' - \omega'_0)$  is imaginary.

#### 4.1 Z-Aligned LCP ( $\sigma$ )

Table 4.2. Symbols Introduced In Section 4.1

Symbol	Units	Description
$k'_3$	rad/s	detuning of $H_1$ frequency from magnetic line center
$\tau_1, \tau_2$	s	rank-one longitudinal and transverse relaxation times, respectively
$\tau_0$	s	rank-two longitudinal relaxation time
$J_0, J_{20}$	erg s	off-resonance longitudinal polarization, rank-one and rank-two, respectively

This section solves the state equations for the case considered in [34], but presents the solutions to all three rank-one components, rather than just the longitudinal polarization. Additionally, we provide justification for considering only a steady-state solution when all parameters are constant.

<sup>9</sup>Note that, because of a typographical error, this is half as large as the definition of  $Q_{B2}$  in [34]. It is believed that the present work is correct.

When  $\epsilon = -\frac{\pi}{4}$ ,  $\phi = \theta = \xi = 0$ , and  $\eta = \frac{\pi}{2}$ , the reduced cross sections become:

$$\begin{aligned} Q_z &= \frac{D_0^2 \hbar}{6} \begin{bmatrix} -2 & -3 & 5 \end{bmatrix} & Q_l &= \frac{D_0^2 \hbar}{3} \begin{bmatrix} 1 & 3 & 5 \end{bmatrix} & Q_0 &= \frac{D_0^2 \hbar}{6\sqrt{6}} \begin{bmatrix} 2 & -3 & 1 \end{bmatrix} \\ -4Q_{11} \equiv Q_{+-} &= \frac{D_0^2 \hbar}{3} \begin{bmatrix} 2 & 9 & 13 \end{bmatrix} & Q_{zz} \equiv Q_{22} &= \frac{D_0^2 \hbar}{6} \begin{bmatrix} 2 & 3 & 7 \end{bmatrix} & Q_{00} &= \frac{D_0^2 \hbar}{36} \begin{bmatrix} 2 & 15 & 19 \end{bmatrix} \\ Q_+, Q_-, Q_2, Q_{-2}, Q_1, Q_{-1} & \text{are all } 0 \end{aligned}$$

Note that the time-dependent elements of  $\mathbf{A}_{12}$  each multiply zeros, so the rotating system works out cleanly. Reference [34] also defines  $\tau_1^{-1} \equiv \tau_c^{-1} + \Phi Q_{B1}$ ,  $\tau_2^{-1} \equiv \tau_c^{-1} + \Phi Q_{B2}$ , and  $J_0 \equiv \hbar \Phi \tau_1 Q_P$ , with the former two being time constants, and the latter being the off-resonance longitudinal polarization (exactly when we only consider the rank one portion, otherwise approximately). We now roll the virtual light shift in by defining  $k'_3 \equiv k_3 + i\Phi Q_S$ , where  $k'_3$  is purely imaginary. We also define a similar time constant,  $\tau_0^{-1} \equiv \tau_c^{-1} + \frac{\Phi}{3}(4Q_{B2} - Q_{B1})$ , where it can easily be shown that the parenthesized quantity is strictly positive. Using this, we can similarly assign a symbol to the rank-two-only off-resonance  $\langle \mathbf{T}_0^{(2)} \rangle$  polarization as  $J_{20} \equiv \hbar \Phi \tau_0 Q_P^{(20)}$ . Then:

$$\begin{aligned} \frac{d\vec{v}}{dt} &= \begin{bmatrix} k'_3 - \tau_2^{-1} & -2k_4 & 0 \\ -k_4 & -\tau_1^{-1} & k_4 \\ 0 & 2k_4 & -\tau_2^{-1} - k'_3 \\ 0 & 0 & 0 \\ \Phi Q_{C0} - 3/8 J_0 \tau_1^{-1} \hbar^{-1} & 0 & 0 \\ 0 & \sqrt{3/8} J_0 \tau_1^{-1} \hbar^{-1} & 0 \\ 0 & 0 & \Phi Q_{C0} + 3/8 J_0 \tau_1^{-1} \hbar^{-1} \\ 0 & 0 & 0 \end{bmatrix} \begin{bmatrix} \langle \tilde{J}_+ \rangle \\ \langle \tilde{J}_z \rangle \\ \langle \tilde{J}_- \rangle \end{bmatrix} + \begin{bmatrix} 0 \\ J_0 \tau_1^{-1} \\ 0 \\ 0 \\ 0 \\ 0 \\ J_{20} \tau_0^{-1} \\ 0 \\ 0 \end{bmatrix} \\ + & \begin{bmatrix} 0 & 4\Phi Q_{C0} - 3/2 J_0 \tau_1^{-1} \hbar^{-1} & 0 & 0 & 0 \\ 0 & 0 & \sqrt{3/2} J_0 \tau_1^{-1} \hbar^{-1} & 0 & 0 \\ 0 & 0 & 0 & 4\Phi Q_{C0} + 3/2 J_0 \tau_1^{-1} \hbar^{-1} & 0 \\ 2k'_3 - \tau_1^{-1} & 2k_4 & 0 & 0 & 0 \\ 2k_4 & k'_3 - \tau_2^{-1} & \sqrt{6}k_4 & 0 & 0 \\ 0 & \sqrt{6}k_4 & -\tau_0^{-1} & \sqrt{6}k_4 & 0 \\ 0 & 0 & \sqrt{6}k_4 & -k'_3 - \tau_2^{-1} & 2k_4 \\ 0 & 0 & 0 & 2k_4 & -2k'_3 - \tau_1^{-1} \end{bmatrix} \begin{bmatrix} \langle \tilde{T}_2^{(2)} \rangle \\ \langle \tilde{T}_1^{(2)} \rangle \\ \langle \tilde{T}_0^{(2)} \rangle \\ \langle \tilde{T}_{-1}^{(2)} \rangle \\ \langle \tilde{T}_{-2}^{(2)} \rangle \end{bmatrix} \end{aligned}$$

Because the homogeneous solution dies out at least as fast as  $\tau_c$ , we are, at this point, only interested in the particular solution. The particular solution can be obtained by undetermined coefficients, and is some nonnegative power of  $t$  times a constant vector. Clearly, a solution growing

linearly, quadratically, etc. in time is nonphysical, so we only consider  $t^0$ , i.e., a constant (steady-state) solution. This is equivalent to saying that no component of the homogeneous solution is constant, or saying that the homogeneous part of the transition matrix (the matrix that would have resulted if I could have concatenated the  $3 \times 8$  and  $5 \times 8$  matrices on one page) is nonsingular.

Since the desired solution is constant, we set the derivative vector to zero and solve an algebraic matrix equation. This is available in closed form, but is so unwieldy as to fail to yield any insight. Therefore, we instead work only with the rank one portion at this point, since this is known to dominate in this particular case, although we also present numerical solutions that include both portions. Solving the rank one portion, we obtain the solution of [34], except also including the virtual light shift:

$$\frac{\langle J_z \rangle}{J_0} = 1 - \frac{\gamma^2 H_1^2 \tau_1 \tau_2}{1 + \gamma^2 H_1^2 \tau_1 \tau_2 + (\gamma H_0 - \omega + \Phi Q_S)^2 \tau_2^2}$$

We also find the rest of the solution, while we're at it:

$$\frac{\langle J_+ \rangle}{\langle J_z \rangle} = e^{i\omega t} \frac{\gamma H_1 \tau_2}{i + (\gamma H_0 - \omega + \Phi Q_S) \tau_2}$$

Now the homogeneous solution to the rank-one portion involves the roots of an arbitrary cubic polynomial, so it is more difficult to describe in closed form. The transition matrix is not Hermitian, but it is nevertheless normal, so it has a complete set of linearly-independent eigenvectors. The characteristic polynomial is, in terms of a dummy variable  $\lambda$ :

$$\lambda^3 + \lambda^2 (\tau_1^{-1} + 2\tau_2^{-1}) + \lambda (\tau_2^{-2} + 2\tau_1^{-1} \tau_2^{-1} - k_3'^2 - 4k_4^2) + (\tau_1^{-1} \tau_2^{-2} - 4k_4^2 \tau_2^{-1} - k_3'^2 \tau_1^{-1}) = 0$$

All coefficients are positive (recall  $k_3'$  and  $k_4$  are imaginary), so we can use the Routh array:

$\lambda^3$ :	1	$\tau_2^{-2} + 2\tau_1^{-1} \tau_2^{-1} - k_3'^2 - 4k_4^2$
$\lambda^2$ :	$\tau_1^{-1} + 2\tau_2^{-1}$	$\tau_1^{-1} \tau_2^{-2} - 4k_4^2 \tau_2^{-1} - k_3'^2 \tau_1^{-1}$
$\lambda$ :	$-4k_4^2 + \tau_2^{-2} + \frac{3}{2} \tau_1^{-1} \tau_2^{-1} + \frac{1-4k_3'^2 \tau_1^2 + 8k_4^2 \tau_1^2}{4\tau_1^2 + 2\tau_1 \tau_2}$	
1:	$-k_3'^2 \tau_1^{-1} + \tau_1^{-1} \tau_2^{-2} - 4k_4^2 \tau_2^{-1}$	

Clearly, all cells of the first column are positive, so all poles are in the open left half-plane and transients die out as expected.

One can find comparisons of the prior theory, containing only rank-one terms, with the new model, including both ranks, in Figures 5.2, 5.3, 5.4, 5.7, and 5.8.

4.2 Z-Linearly-Polarized ( $\pi$ -Parallel)

Table 4.3. Symbols Introduced In Section 4.2

Symbol	Units	Description
$\alpha_1, \alpha_2, \alpha_3, \beta_1, \beta_2$	rad/s	intermediate calculation in closed-form solution
$\gamma_2$	—	intermediate calculation in closed-form solution
$a_2, b_2, d_2$	(rad/s) <sup>2</sup>	coefficients in rational function approximation
$a_0, b_0, d_0$	(rad/s) <sup>4</sup>	coefficients in rational function approximation

This section takes the case of pumping with linearly-polarized light, with polarization azimuth parallel to  $H_0$ , and elaborates on the notes of [35], in the process converting to the more organized matrix form used in the rest of the present document. Additionally, we have extended the solution to include both ranks and derived an approximation that will be used in Sections 6.1 and 6.2 for analyzing experimental data.

In the  $\pi$ -parallel case, where  $\epsilon = 0$ ,  $\phi = \theta = \eta = \frac{\pi}{2}$ , and  $\xi = \frac{-\pi}{2}$ , the reduced cross sections become:

$$\begin{aligned}
 Q_0 &= \frac{-D_0^2 \hbar}{3\sqrt{6}} \begin{bmatrix} 2 & -3 & 1 \end{bmatrix} & Q_I &= \frac{D_0^2 \hbar}{3} \begin{bmatrix} 1 & 3 & 5 \end{bmatrix} \\
 Q_{00} &= \frac{D_0^2 \hbar}{18} \begin{bmatrix} 4 & 3 & 11 \end{bmatrix} & -4Q_{11} = Q_{+-} &= \frac{2D_0^2 \hbar}{3} \begin{bmatrix} 2 & 3 & 7 \end{bmatrix} & Q_{zz} = Q_{22} &= D_0^2 \hbar \begin{bmatrix} 0 & 1 & 1 \end{bmatrix} \\
 Q_z, Q_+, Q_-, Q_2, Q_{-2}, Q_1, Q_{-1} & \text{ are all } 0
 \end{aligned}$$

Note that, as in Section 4.1, the time-varying components of  $\mathbf{A}_{12}$  all multiply zeros. The present case, the case considered in Section 4.1, and certain reflections of these cases are the only cases where the time-varying portions disappear, and therefore the only cases where the closed form solution is straightforward to obtain. And recall that this only occurs if we make the assumptions in the introduction to Chapter 4.

The state equation is nearly identical to that of Section 4.1, but with several terms zeroed out, including the rank-one pumping cross section:

$$\begin{aligned}
 \frac{d\vec{v}'}{dt} = & \begin{bmatrix} k_3 - \tau_2^{-1} & -2k_4 & 0 \\ -k_4 & -\tau_1^{-1} & k_4 \\ 0 & 2k_4 & -k_3 - \tau_2^{-1} \\ 0 & 0 & 0 \\ \Phi Q_{C0} & 0 & 0 \\ 0 & 0 & 0 \\ 0 & 0 & \Phi Q_{C0} \\ 0 & 0 & 0 \end{bmatrix} \begin{bmatrix} \langle \tilde{J}_+ \rangle \\ \langle \tilde{J}_z \rangle \\ \langle \tilde{J}_- \rangle \end{bmatrix} + \begin{bmatrix} 0 \\ 0 \\ 0 \\ 0 \\ 0 \\ 0 \\ 0 \\ J_{20}\tau_0^{-1} \\ 0 \\ 0 \end{bmatrix} \\
 & + \begin{bmatrix} 0 & 4\Phi Q_{C0} & 0 & 0 & 0 \\ 0 & 0 & 0 & 0 & 0 \\ 0 & 0 & 0 & 4\Phi Q_{C0} & 0 \\ 2k_3 - \tau_1^{-1} & 2k_4 & 0 & 0 & 0 \\ 2k_4 & k_3 - \tau_2^{-1} & \sqrt{6}k_4 & 0 & 0 \\ 0 & \sqrt{6}k_4 & -\tau_0^{-1} & \sqrt{6}k_4 & 0 \\ 0 & 0 & \sqrt{6}k_4 & -k_3 - \tau_2^{-1} & 2k_4 \\ 0 & 0 & 0 & 2k_4 & -2k_3 - \tau_1^{-1} \end{bmatrix} \begin{bmatrix} \langle \tilde{T}_2^{(2)} \rangle \\ \langle \tilde{T}_1^{(2)} \rangle \\ \langle \tilde{T}_0^{(2)} \rangle \\ \langle \tilde{T}_{-1}^{(2)} \rangle \\ \langle \tilde{T}_{-2}^{(2)} \rangle \end{bmatrix} \quad (4.1)
 \end{aligned}$$

Now some of the *values* for the symbols in here are different, but the system takes a similar *form*.

In Chapter 5, we will consider a Fourier series steady-state solution for each state element, but this reduces to a constant for each element in this section because the transition matrix is constant. Upon zeroing the state vector derivative, the state vector can be obtained from the algebraic matrix equation:

$$\begin{bmatrix} 0 \\ 0 \\ 0 \\ 0 \\ 0 \\ -J_{20}\tau_0^{-1} \\ 0 \\ 0 \end{bmatrix} = \begin{bmatrix} k_3 - \tau_2^{-1} & -2k_4 & 0 & 0 & 4\Phi Q_{C0} & 0 & 0 & 0 \\ -k_4 & -\tau_1^{-1} & k_4 & 0 & 0 & 0 & 0 & 0 \\ 0 & 2k_4 & -k_3 - \tau_2^{-1} & 0 & 0 & 0 & 4\Phi Q_{C0} & 0 \\ 0 & 0 & 0 & 2k_3 - \tau_1^{-1} & 2k_4 & 0 & 0 & 0 \\ \Phi Q_{C0} & 0 & 0 & 2k_4 & k_3 - \tau_2^{-1} & \sqrt{6}k_4 & 0 & 0 \\ 0 & 0 & 0 & 0 & \sqrt{6}k_4 & -\tau_0^{-1} & \sqrt{6}k_4 & 0 \\ 0 & 0 & \Phi Q_{C0} & 0 & 0 & \sqrt{6}k_4 & -k_3 - \tau_2^{-1} & 2k_4 \\ 0 & 0 & 0 & 0 & 0 & 0 & 2k_4 & -2k_3 - \tau_1^{-1} \end{bmatrix} \begin{bmatrix} \langle \tilde{J}_+ \rangle \\ \langle \tilde{J}_z \rangle \\ \langle \tilde{J}_- \rangle \\ \langle \tilde{T}_2^{(2)} \rangle \\ \langle \tilde{T}_1^{(2)} \rangle \\ \langle \tilde{T}_0^{(2)} \rangle \\ \langle \tilde{T}_{-1}^{(2)} \rangle \\ \langle \tilde{T}_{-2}^{(2)} \rangle \end{bmatrix}$$

Because the  $Q_{C0}$  term coupling the rank-one and rank-two portions is nominally zero close to the  $D_0$  line center, and because the rank-one portion is neither pumped nor directly observed, it would be a very good approximation to neglect the rank-one portion. The solution if one neglects that portion is [35]:

$$\alpha_1 \equiv -k_3 + \tau_2^{-1} - \frac{4k_4^2}{\tau_1^{-1} - 2k_3} \quad \langle \tilde{T}_0^{(2)} \rangle = \frac{J_{20}\tau_0^{-1}}{\tau_0^{-1} - 12k_4^2 \text{Re}\left\{\frac{1}{\alpha_1}\right\}}$$

Here, we will derive a result similar to this, but keeping the terms from both ranks. First, we use  $\alpha_1$  to eliminate  $\langle \tilde{T}_{\pm 2}^{(2)} \rangle$ :

$$\begin{bmatrix} 0 \\ 0 \\ 0 \\ 0 \\ -J_{20}\tau_0^{-1} \\ 0 \end{bmatrix} = \begin{bmatrix} k_3 - \tau_2^{-1} & -2k_4 & 0 & 4\Phi Q_{C0} & 0 & 0 \\ -k_4 & -\tau_1^{-1} & k_4 & 0 & 0 & 0 \\ 0 & 2k_4 & -k_3 - \tau_2^{-1} & 0 & 0 & 4\Phi Q_{C0} \\ \Phi Q_{C0} & 0 & 0 & -\alpha_1 & \sqrt{6}k_4 & 0 \\ 0 & 0 & 0 & \sqrt{6}k_4 & -\tau_0^{-1} & \sqrt{6}k_4 \\ 0 & 0 & \Phi Q_{C0} & 0 & \sqrt{6}k_4 & -\alpha_1^* \end{bmatrix} \begin{bmatrix} \langle \tilde{J}_+ \rangle \\ \langle \tilde{J}_z \rangle \\ \langle \tilde{J}_- \rangle \\ \langle \tilde{T}_1^{(2)} \rangle \\ \langle \tilde{T}_0^{(2)} \rangle \\ \langle \tilde{T}_{-1}^{(2)} \rangle \end{bmatrix}$$

To make the steps a bit clearer, we use the scale factors of Equations (3.21) to make the transition matrix more symmetric:

$$\begin{bmatrix} 0 \\ 0 \\ 0 \\ 0 \\ -J_{20}\tau_0^{-1} \\ 0 \end{bmatrix} = \begin{bmatrix} k_3 - \tau_2^{-1} & -\sqrt{2}k_4 & 0 & 2\Phi Q_{C0} & 0 & 0 \\ -\sqrt{2}k_4 & -\tau_1^{-1} & \sqrt{2}k_4 & 0 & 0 & 0 \\ 0 & \sqrt{2}k_4 & -k_3 - \tau_2^{-1} & 0 & 0 & 2\Phi Q_{C0} \\ 2\Phi Q_{C0} & 0 & 0 & -\alpha_1 & \sqrt{6}k_4 & 0 \\ 0 & 0 & 0 & \sqrt{6}k_4 & -\tau_0^{-1} & \sqrt{6}k_4 \\ 0 & 0 & 2\Phi Q_{C0} & 0 & \sqrt{6}k_4 & -\alpha_1^* \end{bmatrix} \begin{bmatrix} \langle \tilde{J}_+ \rangle / 2 \\ \langle \tilde{J}_z \rangle / \sqrt{2} \\ \langle \tilde{J}_- \rangle / 2 \\ \langle \tilde{T}_1^{(2)} \rangle \\ \langle \tilde{T}_0^{(2)} \rangle \\ \langle \tilde{T}_{-1}^{(2)} \rangle \end{bmatrix}$$

Now we define:

$$\beta_1 \equiv 2\tau_1 k_4^2 + k_3 - \tau_2^{-1}$$

and eliminate  $\langle \tilde{J}_z \rangle$ , while changing notation for the remaining two rank-one tensors, as explained in Equations (3.21):

$$\begin{bmatrix} 0 \\ 0 \\ 0 \\ -J_{20}\tau_0^{-1} \\ 0 \end{bmatrix} = \begin{bmatrix} \beta_1 & -2\tau_1 k_4^2 & 2\Phi Q_{C0} & 0 & 0 \\ -2\tau_1 k_4^2 & \beta_1^* & 0 & 0 & 2\Phi Q_{C0} \\ 2\Phi Q_{C0} & 0 & -\alpha_1 & \sqrt{6}k_4 & 0 \\ 0 & 0 & \sqrt{6}k_4 & -\tau_0^{-1} & \sqrt{6}k_4 \\ 0 & 2\Phi Q_{C0} & 0 & \sqrt{6}k_4 & -\alpha_1^* \end{bmatrix} \begin{bmatrix} \langle \tilde{T}_1^{(1)} \rangle \\ \langle \tilde{T}_{-1}^{(1)} \rangle \\ \langle \tilde{T}_1^{(2)} \rangle \\ \langle \tilde{T}_0^{(2)} \rangle \\ \langle \tilde{T}_{-1}^{(2)} \rangle \end{bmatrix}$$

Next, we define:

$$\gamma_2 \equiv \frac{4\Phi^2 Q_{C0}^2}{4k_4^4 \tau_1^2 - |\beta_1|^2} \quad \alpha_2 \equiv \alpha_1 - \beta_1^* \gamma_2 \quad \beta_2 \equiv 2k_4^2 \tau_1 \gamma_2$$

and use them to eliminate the rank-one portion entirely, but at the cost of making the remaining matrix full:

$$\begin{bmatrix} 0 \\ -J_{20}\tau_0^{-1} \\ 0 \end{bmatrix} = \begin{bmatrix} -\alpha_2 & \sqrt{6}k_4 & \beta_2 \\ \sqrt{6}k_4 & -\tau_0^{-1} & \sqrt{6}k_4 \\ \beta_2 & \sqrt{6}k_4 & -\alpha_2^* \end{bmatrix} \begin{bmatrix} \langle \tilde{\mathbf{T}}_1^{(2)} \rangle \\ \langle \tilde{\mathbf{T}}_0^{(2)} \rangle \\ \langle \tilde{\mathbf{T}}_{-1}^{(2)} \rangle \end{bmatrix}$$

We can, however, define:

$$\alpha_3 \equiv \frac{|\alpha_2|^2 - \beta_2^2}{\alpha_2^* + \beta_2} = \frac{\text{Re}\{\alpha_2\} + \beta_2}{|\alpha_2|^2 - \beta_2^2} = \frac{-4k_4^4\tau_1^2\gamma_2^2 + |\alpha_1^* - \beta_1\gamma_2|^2}{2k_4^4\tau_1\gamma_2 + \alpha_1^* - \beta_1\gamma_2}$$

which is completely analogous to  $\alpha_1$ , in the sense that use of  $\alpha_1$  in place of  $\alpha_3$  is equivalent to only solving the rank-two portion.

Using this, we recover the desired sparsity pattern:

$$\begin{bmatrix} 0 \\ -J_{20}\tau_0^{-1} \\ 0 \end{bmatrix} = \begin{bmatrix} -\alpha_3 & \sqrt{6}k_4 & 0 \\ \sqrt{6}k_4 & -\tau_0^{-1} & \sqrt{6}k_4 \\ 0 & \sqrt{6}k_4 & -\alpha_3^* \end{bmatrix} \begin{bmatrix} \langle \tilde{\mathbf{T}}_1^{(2)} \rangle \\ \langle \tilde{\mathbf{T}}_0^{(2)} \rangle \\ \langle \tilde{\mathbf{T}}_{-1}^{(2)} \rangle \end{bmatrix}$$

Finally, we can directly obtain the solution for the observable component:

$$\langle \tilde{\mathbf{T}}_0^{(2)} \rangle = \frac{J_{20}\tau_0^{-1}}{\tau_0^{-1} - 12k_4^2 \text{Re}\left\{\frac{1}{\alpha_3}\right\}}$$

As mentioned, the rank-one portion contributes very little, and results in a ratio of even sixth-order polynomials in  $k_3$ , as opposed to the ratio of even fourth-order polynomials one obtains if one lets  $\alpha_3 \rightarrow \alpha_1$ :

$$\frac{\langle \tilde{\mathbf{T}}_0^{(2)} \rangle}{J_{20}} \approx \frac{[4\tau_1^2\tau_2^2]k_3^4 + [-\tau_2^2 - 4\tau_1^2(1 + 4k_4^2\tau_2^2)]k_3^2 + [1 - 4k_4^2\tau_1\tau_2]^2}{[4\tau_1^2\tau_2^2]k_3^4 + [-\tau_2^2 + 4\tau_1^2(-1 + 4k_4^2(3\tau_0 - \tau_2)\tau_2)]k_3^2 + [(-1 + 4k_4^2\tau_1\tau_2)(-1 + 4k_4^2(3\tau_0 + \tau_1)\tau_2)]} \quad (4.2)$$

One sees in an experimental resonance curve for this configuration, such as that in Figure 6.1, that a ratio of two even quartics makes some sense in analogy with a transfer function having two poles and two zeros, outlined in Equation (4.4), particularly since  $k_3$  is proportional

(by *i*) to a frequency detuning. The only possible difficulty is the observation equations, Equations (3.40) and (3.42), which, for the case considered in this section, become:

$$\alpha'(z) = -\frac{2\pi n_S}{3c\hbar^3} \left[ \langle \tilde{T}_0^{(2)} \rangle \left( \sum_{\omega'_0} \tau G(\omega' - \omega'_0) 3Q_0 \right) + \hbar \left( \sum_{\omega'_0} \tau G(\omega' - \omega'_0) Q_I \right) \right], \quad \Phi(z) = \Phi_{\text{IN}} e^{\alpha'(z)\omega'z},$$

or, in terms of the appropriate cross sections:

$$\Phi(z) = \Phi_{\text{IN}} e^{-z n_S Q_A} \exp \left[ \frac{z n_S}{\hbar} \langle \tilde{T}_0^{(2)} \rangle Q_M^{(20)} \right] = \Phi_{\text{IN}} e^{-z n_S Q_A} \exp \left[ 3z \left( Q_P^{(20)} \right)^2 (n_S \tau_0 \Phi) \frac{\langle \tilde{T}_0^{(2)} \rangle}{J_{20}} \right]. \quad (4.3)$$

Because the latter exponential (involving  $\langle \tilde{T}_0^{(2)} \rangle$ ) is generally much smaller than the first (involving  $Q_A$ ), and the  $Q_A$  exponential factor is fixed for constant metastable density, [34] indicates a first-order Taylor series expansion of the exponential in the longitudinal polarization is somewhat appropriate. Under this assumption, and taking  $\langle \tilde{T}_0^{(2)} \rangle$  to be a ratio of even quartics in  $k_3$ ,  $\Phi(z)$  is also a ratio of even quartics in  $k_3$ . This suggests that a  $4 \times 4$  Padé approximant (which happens to remain even) to  $\Phi(z)$  in  $k_3$  would work *at least* as well. Keep in mind that the experimental data of Section 6.1 actually supports the ratio of even-order quartics for  $\Phi(z)$  directly, rather than for  $\langle \tilde{T}_0^{(2)} \rangle$ , so the reasoning here was somewhat backwards.

The fit of  $\Phi(z)$  to an arbitrary ratio of even quartics is so good that it makes sense to use the Padé approximant to go back to a ratio of even quartics for  $\langle \tilde{T}_0^{(2)} \rangle$  and solve for five independent parameters. Since  $k_3$  is the independent variable, there *are* only five parameters remaining to solve for:  $J_{20}$ ,  $\tau_{0,1,2}$ , and  $k_4$ . Actually,  $\tau_0$  is not independent in the theory, a fact that may serve as a partial check of the impact of the various approximations we've made. Note that these parameters are unlikely to be simultaneously accurate at any one point in the cell, since they are all some sort of spatial average. The exception is that, by design,  $k_4$  is expected to be reasonably uniform. It is expected that, at least with only one resonance curve, we will not be able to solve independently for  $n_S$  and  $J_{20}$ , since the absorption level is typically used as a measure of  $n_S$ . Thus, the theoretical model will provide the distinction between the two, and should not be considered an independent verification of  $J_{20}$ .

The output photon flux density  $\Phi(L)$  is proportional to the photocurrent by factors involving beam cross-sectional area, photodiode sensitivity, and some unknown amount of back-reflection

from optical surfaces. Only the photodiode sensitivity is known, but, from a data fitting perspective, the back-reflection can be considered a reduction in the *effective* photodiode sensitivity, since photocurrent is measured and the back-reflection percentage, like photodiode sensitivity, is a multiplicative factor used to determine the actual optical power in the cell. Since the photocurrent at large magnetic detunings  $\omega - \gamma H_0$  is easily determined from collected data, we can consider all of these to form a baseline and primarily examine the remaining multiplicative factor:

$$(\text{photocurrent}) = (\text{baseline}) \frac{[k_3^2 - \gamma^2 (\text{first zero, in nT})^2][k_3^2 - \gamma^2 (\text{second zero, in nT})^2]}{[k_3^2 - \gamma^2 (\text{first pole, in nT})^2][k_3^2 - \gamma^2 (\text{second pole, in nT})^2]} . \quad (4.4)$$

Using a  $4 \times 4$  Padé approximant at the origin, this can be expressed in the form:

$$(\text{photocurrent}) = (\text{baseline}) e^{-1} \exp \frac{k_3^4 + b_2 k_3^2 + b_0}{k_3^4 + a_2 k_3^2 + a_0} . \quad (4.5)$$

The expressions used to perform this conversion are lengthy, but may be determined in closed form if desired. The worst-case relative error introduced through the Padé approximation is about  $10^{-5}$  for the data considered in Section 6.1. It is then straightforward to convert this to the form required by Equations (4.2) and (4.3):

$$\begin{aligned} (\text{photocurrent}) &= (\text{baseline}) \exp \left[ -3n_S \tau_0 (Q_P^{(20)})^2 \Phi L \right] \exp \left[ \left( 3n_S \tau_0 (Q_P^{(20)})^2 \Phi L \right) \frac{k_3^4 + d_2 k_3^2 + d_0}{k_3^4 + a_2 k_3^2 + a_0} \right] \\ &= (\text{baseline}) \exp \left[ -3n_S \tau_0 (Q_P^{(20)})^2 \Phi L \right] \exp \left[ \left( 3n_S \tau_0 (Q_P^{(20)})^2 \Phi L \right) \frac{\langle T_0^{(2)} \rangle}{J_{20}} \right] , \\ d_2 &= a_2 + (b_2 - a_2) \left( 3n_S \tau_0 (Q_P^{(20)})^2 \Phi L \right)^{-1} , \text{ and} \\ d_0 &= a_0 + (b_0 - a_0) \left( 3n_S \tau_0 (Q_P^{(20)})^2 \Phi L \right)^{-1} . \end{aligned} \quad (4.6)$$

We will consider the calculation of the cross section  $Q_P^{(20)}$  to be comparatively well established<sup>10</sup>, but note that there is a choice in the value of  $n_S \tau_0 \Phi$ . It turns out that this value will have a significant impact on the fit theoretical parameters, although, if one ignores the constraint on the relationship between  $\tau_0$ ,  $\tau_1$ , and  $\tau_2$ , an excellent fit may always be obtained at the expense of

---

<sup>10</sup>However, it is acceptable if it is not, provided one is only concerned about the transformation into the form of Equation (4.6), and not the interpretation of the fit value of  $n_S \tau_0 \Phi$ .

any physical meaning. Such a fit is useful as a reference point for fitting more meaningful curves, rather than (initially) attempting to fit straight to noisy data.

While the code for the model can determine  $\tau_c$  (closely related to  $\tau_0$ ) and  $n_S$  as a function of  $\Phi$ , the beam radius, and a set of better-known experimental parameters, to date it is not clear if we can satisfactorily extract the individual values of  $n_S$ ,  $\tau_0$  and  $\Phi$  from the product  $n_S \tau_0 \Phi$ , because the data may not be sufficiently sensitive to the individual variables. It is possible that a future extension may accomplish this extraction.

One can solve for the parameters used in Equation 4.2 such that Equation (4.6) is satisfied:

$$\begin{aligned} \tau_2^{-1} &= \frac{|a_2 - d_2| \sqrt{d_0} \sqrt{2 \sqrt{d_0} - d_2}}{\left| a_0 - \sqrt{d_0} (a_2 - d_2 + \sqrt{d_0}) \right|} & \tau_1^{-1} &= 2\tau_2^{-1} \frac{d_0 - a_0}{\sqrt{d_0} (a_2 - d_2)} \\ \tau_0^{-1} &= 3\tau_2^{-1} \frac{\tau_1^{-1} \tau_2^{-1} - 2 \sqrt{d_0}}{a_2 - d_2} & k_4^2 &= -\frac{d_2 + \tau_2^{-2}}{4} - \frac{\tau_1^{-2}}{16} = -\frac{\gamma H_1}{2} \end{aligned} \quad (4.7)$$

Note that while it is desirable for  $3\tau_0^{-1} = 4\tau_2^{-1} - \tau_1^{-1}$ , this cannot be used to solve for  $n_S \tau_0 \Phi$  in closed form. The constraint on  $\tau_0$  is certainly one possible source of a merit function for numerical optimization, however. It should be reiterated that, if one ignores this constraint, then Equation (4.2) will fit for any choice of  $n_S \tau_0 \Phi$ , and that Equation (4.4) is fit without even choosing a value for  $n_S \tau_0 \Phi$  at all. The latter case is useful for extracting slopes and linewidths from noisy measurement data, where one cannot ordinarily take the derivative.

Presently three ranges of inputs are used to determine the range of allowable values of  $n_S \tau_0 \Phi$  to test for agreement between the model and data. In particular, we vary the effective light beam radius, the input optical power, and a multiplicative factor applied to  $\tau_c$ , where the value of  $\tau_c$  is obtained from the discharge model. This latter multiplicative factor was introduced because there is some experimental evidence that the theoretically-calculated value of  $\tau_c$  may be too low.

The input power is allowed to be larger than the experimentally-determined value due to the unknown level of back-reflections. This hypothesis for power variation does not affect the accuracy of the measured ratio of input power at large detunings  $\omega - \gamma H_0$  to input power with the discharge extinguished. Reference to an ‘‘absorption level,’’ such as 15%, with no further

qualification, may be used to describe the complement of this ratio; in that example, 85% of the input light is transmitted when off-resonance.

#### 4.3 Linearly-polarized against $Z$ ( $\pi$ -Perpendicular)

Table 4.4. Symbols Introduced In Section 4.3

Symbol	Units	Description
$u_{\xi,n}$	erg · s	Fourier series coefficients for state vector components, frequency $n\omega$

This section presents a solution to the rank-two portion of the state equation for the case where linearly polarized light ( $\epsilon = 0$ ) has its polarization azimuth perpendicular to the  $H_0$  field. This is referred to as  $\pi$ -perpendicular, and is further specified in this case by  $\phi = 0$ ,  $-\xi = \eta = \frac{\pi}{2}$ . The work of this section can also be seen to motivate the results in Chapter 5, since the method here is similar, but specialized.

The reduced cross sections become:

$$\begin{aligned}
 Q_0 &= \frac{D_0^2 \hbar}{6\sqrt{6}} \begin{bmatrix} 2 & -3 & 1 \end{bmatrix} & Q_I &= \frac{D_0^2 \hbar}{3} \begin{bmatrix} 1 & 3 & 5 \end{bmatrix} \\
 Q_{-2}^* &= Q_2 = \frac{D_0^2 \hbar}{12} (-e^{2i\theta}) \begin{bmatrix} 2 & -3 & 1 \end{bmatrix} \\
 Q_z, Q_+, Q_-, Q_1, Q_{-1} & \text{ are all } 0 \\
 Q_{00} &= \frac{D_0^2 \hbar}{36} \begin{bmatrix} 2 & 15 & 19 \end{bmatrix} & -4Q_{11} = Q_{+-} &= \frac{D_0^2 \hbar}{3} \begin{bmatrix} 2 & 9 & 13 \end{bmatrix} & Q_{zz} = Q_{22} &= \frac{D_0^2 \hbar}{6} \begin{bmatrix} 2 & 3 & 7 \end{bmatrix}
 \end{aligned}$$

At first glance, the dependence of  $Q_{\pm 2}$  on  $\theta$  is interesting, since the value of  $\theta$  should be indeterminate for  $\phi = 0$ , given the fact that the orientation of the  $\hat{X}$  and  $\hat{Y}$  axes does not figure into the problem formulation. The choice of coordinate system may be what leads to the curious phase factor in the evaluation of  $Q_{\pm 2}$  in this situation. Numerical work based on the method of Chapter 5 indicates that the choice of  $\theta$  does not make a difference in the observed transmitted light, so, in this section, we will assume  $\theta = \frac{\pi}{2}$  to make  $Q_{-2}^* = Q_2 = \frac{\hbar D_0^2}{12} \begin{bmatrix} 2 & -3 & 1 \end{bmatrix}$  real.

As in Section 4.2, the rank-one portion is not directly pumped, not directly observed, and only weakly coupled to the rank-two portion. This time we will neglect it. The arbitrary choice to set  $H_1$  perpendicular to the light polarization is likely immaterial, up to a possible phase, since we have assumed a rotating  $H_1$ . Unlike Sections 4.1 and 4.2, this case is complicated by the fact that the transition matrix has time-varying components. The state equation is:

$$\frac{d}{dt} \begin{bmatrix} \langle \tilde{T}_2^{(2)} \rangle \\ \langle \tilde{T}_1^{(2)} \rangle \\ \langle \tilde{T}_0^{(2)} \rangle \\ \langle \tilde{T}_{-1}^{(2)} \rangle \\ \langle \tilde{T}_{-2}^{(2)} \rangle \end{bmatrix} = \begin{bmatrix} \Phi Q_P^{(22)} e^{-2i\omega t} \\ 0 \\ J_{20} \tau_0^{-1} \\ 0 \\ \Phi Q_P^{(22)} e^{2i\omega t} \end{bmatrix} + \begin{bmatrix} 2k_3 - \tau_1^{-1} & 2k_4 & \sqrt{3/2} \Phi Q_P^{(22)} e^{-2i\omega t} & 0 & 0 \\ 2k_4 & k_3 - \tau_2^{-1} & \sqrt{6} k_4 & 3/2 \Phi Q_P^{(22)} e^{-2i\omega t} & 0 \\ \sqrt{3/2} \Phi Q_P^{(22)} e^{2i\omega t} & \sqrt{6} k_4 & -\tau_0^{-1} & \sqrt{6} k_4 & \sqrt{3/2} \Phi Q_P^{(22)} e^{-2i\omega t} \\ 0 & 3/2 \Phi Q_P^{(22)} e^{2i\omega t} & \sqrt{6} k_4 & -k_3 - \tau_2^{-1} & 2k_4 \\ 0 & 0 & \sqrt{3/2} \Phi Q_P^{(22)} e^{2i\omega t} & 2k_4 & -2k_3 - \tau_1^{-1} \end{bmatrix} \begin{bmatrix} \langle \tilde{T}_2^{(2)} \rangle \\ \langle \tilde{T}_1^{(2)} \rangle \\ \langle \tilde{T}_0^{(2)} \rangle \\ \langle \tilde{T}_{-1}^{(2)} \rangle \\ \langle \tilde{T}_{-2}^{(2)} \rangle \end{bmatrix}$$

If we neglect the time-varying components of the transition matrix, we wind up with the same solution as in Section 4.2, although, of course, the symbols have substantially different numerical values. Therefore, it makes sense to either stop here, or try to keep some or all of these terms. If we did neglect the time-varying components, the interpretation of  $J_{20}$  would remain the same as before, but keeping the time-varying components introduces a small change in the DC off-resonance polarization, compared to  $J_{20}$ .

Now, the only way the elements are related is by integer powers of  $e^{2i\omega t}$ , and the system is linear, but time-varying. It is reasonable to conclude that, whatever the time dependence of  $\langle \tilde{T}_0^{(2)} \rangle$ , the other components follow it, modified, at most, by a Fourier series with fundamental  $2\omega$ .

A seemingly-reasonable simplification is to assume the driving terms set the time dependence of the states, particularly since the observation equation brings those particular frequencies back to DC in each case. Unfortunately, doing so leaves inconsistencies that, while perhaps acceptable, are difficult to justify. So we instead try a Fourier series solution. This approach is similar to what we will do in Chapter 5, but with fewer terms. Let

$$\langle \tilde{T}_\xi^{(2)} \rangle = \sum_{n=-\infty}^{\infty} u_{\xi,2n} e^{2ni\omega t}, \text{ which implies } \frac{d}{dt} \langle \tilde{T}_\xi^{(2)} \rangle = \sum_{n=-\infty}^{\infty} [u_{\xi,2n} + 2ni\omega u_{\xi,2n}] e^{2ni\omega t}$$

We have assumed that  $\omega$  is constant here, like every other parameter; attention is called to this since such an assumption is only reasonable in some experiments (such as those in Chapter 6), and not in an actual magnetometer system. At this point, we approximate by neglecting  $\dot{u}_{\xi,2n}$ , i.e., taking the steady-state solution as we have been doing previously. Then we obtain a system of equations:

$$2ni\omega \begin{bmatrix} u_{2,2n} \\ u_{1,2n} \\ u_{0,2n} \\ u_{-1,2n} \\ u_{-2,2n} \end{bmatrix} = \begin{bmatrix} \Phi Q_P^{(22)} \delta_{2n+2} \\ 0 \\ J_{20} \tau_0^{-1} \delta_n \\ 0 \\ \Phi Q_P^{(22)} \delta_{2n-2} \end{bmatrix} + \begin{bmatrix} (2k_3 - \tau_1^{-1}) u_{2,2n} + 2k_4 u_{1,2n} + \sqrt{3/2} \Phi Q_P^{(22)} u_{0,2n+2} \\ 2k_4 u_{2,2n} + (k_3 - \tau_2^{-1}) u_{1,2n} + \sqrt{6} k_4 u_{0,2n} + {}^{3/2} \Phi Q_P^{(22)} u_{-1,2n+2} \\ \sqrt{3/2} \Phi Q_P^{(22)} (u_{2,2n-2} + u_{-2,2n+2}) + \sqrt{6} k_4 (u_{1,2n} + u_{-1,2n}) - \tau_0^{-1} u_{0,2n} \\ 2k_4 u_{-2,2n} + (-k_3 - \tau_2^{-1}) u_{-1,2n} + \sqrt{6} k_4 u_{0,2n} + {}^{3/2} \Phi Q_P^{(22)} u_{1,2n-2} \\ (-2k_3 - \tau_1^{-1}) u_{-2,2n} + 2k_4 u_{-1,2n} + \sqrt{3/2} \Phi Q_P^{(22)} u_{0,2n-2} \end{bmatrix}$$

Clearly, this system is (countably) infinite, since  $n$  is any integer. However, it is only excited in the near vicinity of  $n = 0$ , and, physically, one does not expect harmonics too far above  $\omega$ , so the coupling must be such that they eventually die out. That said, no statement has been made about the relative magnitude of DC and the first few harmonics of  $\omega$ . We might, at this point, assume we know the magnitude of terms with  $n \neq 0$ , and solve for the other components. Then perhaps we can return and see what the impact of varying those unknowns is, ideally setting them to zero. So:

$$\begin{bmatrix} 0 \\ 0 \\ -J_{20} \tau_0^{-1} \\ 0 \\ 0 \end{bmatrix} = \Phi Q_P^{(22)} \begin{bmatrix} \sqrt{3/2} u_{0,2} \\ {}^{3/2} u_{-1,2} \\ \sqrt{3/2} (u_{2,-2} + u_{-2,2}) \\ {}^{3/2} u_{1,-2} \\ \sqrt{3/2} u_{0,-2} \end{bmatrix} + \begin{bmatrix} 2k_3 - \tau_1^{-1} & 2k_4 & 0 & 0 & 0 \\ 2k_4 & k_3 - \tau_2^{-1} & \sqrt{6} k_4 & 0 & 0 \\ 0 & \sqrt{6} k_4 & -\tau_0^{-1} & \sqrt{6} k_4 & 0 \\ 0 & 0 & \sqrt{6} k_4 & -k_3 - \tau_2^{-1} & 2k_4 \\ 0 & 0 & 0 & 2k_4 & -2k_3 - \tau_1^{-1} \end{bmatrix} \begin{bmatrix} u_{2,0} \\ u_{1,0} \\ u_{0,0} \\ u_{-1,0} \\ u_{-2,0} \end{bmatrix}$$

We can simplify in a manner similar to Section 4.2:

$$\alpha_1 \equiv -k_3 + \tau_2^{-1} - \frac{4k_4^2}{\tau_1^{-1} - 2k_3}$$

$$\begin{bmatrix} 0 \\ -J_{20} \tau_0^{-1} \\ 0 \end{bmatrix} = \Phi Q_P^{(22)} \begin{bmatrix} {}^{3/2} u_{-1,2} + \sqrt{3/2} \frac{2k_4}{\tau_1^{-1} - 2k_3} u_{0,2} \\ \sqrt{3/2} (u_{2,-2} + u_{-2,2}) \\ {}^{3/2} u_{1,-2} + \sqrt{3/2} \frac{2k_4}{\tau_1^{-1} + 2k_3} u_{0,-2} \end{bmatrix} + \begin{bmatrix} -\alpha_1 & \sqrt{6} k_4 & 0 \\ \sqrt{6} k_4 & -\tau_0^{-1} & \sqrt{6} k_4 \\ 0 & \sqrt{6} k_4 & -\alpha_1^* \end{bmatrix} \begin{bmatrix} u_{1,0} \\ u_{0,0} \\ u_{-1,0} \end{bmatrix}$$

The solution is then:

$$u_{0,0} = \frac{J_{20}\tau_0^{-1} + \Phi Q_P^{(22)} \sqrt{3/2} (u_{2,-2} + u_{-2,2})}{\tau_0^{-1} - 12k_4^2 \text{Re} \left\{ \frac{1}{\alpha_1} \right\}} + \Phi Q_P^{(22)} 3k_4 \frac{\frac{1}{\alpha_1} \left( \sqrt{3/2} u_{-1,2} + \frac{2k_4}{\tau_1^{-1} - 2k_3} u_{0,2} \right) + \frac{1}{\alpha_1^*} \left( \sqrt{3/2} u_{1,-2} + \frac{2k_4}{\tau_1^{-1} + 2k_3} u_{0,-2} \right)}{\tau_0^{-1} - 12k_4^2 \text{Re} \left\{ \frac{1}{\alpha_1} \right\}}$$

Note that the longitudinal polarization when  $H_1$  is deactivated has moved from  $J_{20}$  to

$$J_{20} + \tau_0 \Phi Q_P^{(22)} \sqrt{3/2} (u_{2,-2} + u_{-2,2}) .$$

In terms of  $u_{0,0}$ , we obtain the other solutions:

$$u_{1,0} = \frac{\sqrt{6}k_4 u_{0,0} + \Phi Q_P^{(22)} \left( 3/2 u_{-1,2} + \sqrt{3/2} \frac{2k_4}{\tau_1^{-1} - 2k_3} u_{0,2} \right)}{\alpha_1},$$

$$u_{-1,0} = \frac{\sqrt{6}k_4 u_{0,0} + \Phi Q_P^{(22)} \left( 3/2 u_{1,-2} + \sqrt{3/2} \frac{2k_4}{\tau_1^{-1} + 2k_3} u_{0,-2} \right)}{\alpha_1^*}$$

But because  $u_{1,0}^* = -u_{-1,0}$ , we can simplify the solution for  $u_{0,0}$ :

$$u_{0,0} = \frac{J_{20}\tau_0^{-1} + \Phi Q_P^{(22)} \sqrt{3/2} (u_{2,-2} + u_{-2,2})}{\tau_0^{-1} - 12k_4^2 \text{Re} \left\{ \frac{1}{\alpha_1} \right\}} + \frac{\text{Im} \left\{ \frac{1}{\alpha_1} \left( \sqrt{3/2} u_{-1,2} + \frac{2k_4}{\tau_1^{-1} - 2k_3} u_{0,2} \right) \right\}}{\tau_0^{-1} - 12k_4^2 \text{Re} \left\{ \frac{1}{\alpha_1} \right\}}$$

Finally,

$$u_{\pm 2,0} = \frac{\Phi Q_P^{(22)} \sqrt{3/2} u_{0,\pm 2} + 2k_4 u_{\pm 1,0}}{\tau_1^{-1} \mp 2k_3}$$

Note that, since  $u_{2,0}^* = u_{-2,0}$ , we can conclude<sup>11</sup> that  $u_{0,2}^* = u_{0,-2}$ . This then implies that  $u_{-1,2}^* = -u_{1,-2}$ . Now only the  $u_{2n,-2n}$  terms can be observed at DC, and of the terms of that form, we have only solved for  $u_{0,0}$ , and, even then, only in terms of higher-order sets of coefficients. While it is completely reasonable to expect these coefficients to be small for very large values of  $|n|$ , one cannot justifiably claim  $|n| > 0$  satisfies that criterion. It is desirable to obtain a recurrence relation

<sup>11</sup>This would not be appropriate if  $Q_P^{(22)}$  had not been chosen to be real.

from one order to the next, and to evaluate the sensitivity of  $u_{0,0}$  to changes in initial estimates of the higher-order terms. The first few equations in that process can be found in Appendix E.

In passing, it should be mentioned that the case of off-axis  $\sigma$ -pumping, where  $\epsilon = \pm\pi/4$ ,  $\theta = \phi = \eta = \xi = \pi/2$ , gives results that, at least at DC, are very similar to the solution to the problem in this section. The off-axis  $\sigma$ -pumping case is more complex, since the  $Q_{\pm}$  values are then also nonzero, so both ranks are forced and observed. Some examples of the off-axis  $\sigma$ -pumping case can be found in Figures 6.24 and 6.25. Off-axis  $\sigma$ -pumping, even more so than the case presented in this section, yields a weak signal, but it is nevertheless a case of interest, since most  $^4\text{He}$  magnetometers are used in applications where they can be rotated. Much of the theory of this section (although, to better effect, the theory of Chapter 5) can also be applied to the off-axis  $\sigma$ -pumping case.

CHAPTER 5  
GENERAL STEADY-STATE SOLUTION

Table 5.1. Symbols Introduced In Chapter 5

Symbol	Units	Description
$\mathbf{A}'_a$	$s^{-1}$	general transition matrix
$\vec{\mathbf{a}}_{p''}$	erg	general inhomogeneous term of state equation
$\eta_{\square}^{\square}$	$s^{-1}$	general transition term; superscript for LHS term, subscript for RHS term
$\zeta_{\square}^{\square}$	$s^{-1}$	general transition term; superscript for LHS term, subscript for RHS term
$\zeta_h^{\square}$	erg	coefficients of forcing term; superscript for LHS term
$\vec{\zeta}_{h,n}$	erg	forcing vector, frequency $n\omega$
$\vec{\mathbf{u}}_n$	erg · s	Fourier series coefficients for state vector, frequency $n\omega$

This section generalizes the special cases presented in Chapter 4 to provide a complete, albeit numerical and steady-state, solution to the equations of Section 3.10.1 over the entire parameter space. We no longer neglect the Bloch-Siegert shift introduced in Equation (3.34) and described at the end of Section 3.8. The notation and approach are somewhat similar to that of Section 4.3, since the situation considered in that section also needed to account for time-dependent elements in the state transition matrix. Plots are presented for a variety of situations, with interesting effects identified and improvements suggested.

### 5.1 General Concerns

Begin by rewriting Equation (3.41) as:

$$\frac{d\vec{\mathbf{v}}'}{dt} = \mathbf{A}'_a \vec{\mathbf{v}}' + \vec{\mathbf{a}}_{p''}, \quad \vec{\mathbf{a}}_{p''} \equiv -\frac{2\pi\Phi\omega'}{3c\hbar} \vec{\mathbf{a}}_{p'} \equiv \begin{bmatrix} \zeta_h^+ e^{-i\omega t} \\ \zeta_h^z \\ \zeta_h^- e^{i\omega t} \\ \zeta_h^2 e^{-2i\omega t} \\ \zeta_h^1 e^{-i\omega t} \\ \zeta_h^0 \\ \zeta_h^{-1} e^{i\omega t} \\ \zeta_h^{-2} e^{2i\omega t} \end{bmatrix}$$

Then:

$$\mathbf{A}'_a \equiv \left[ \begin{array}{ccc|ccc}
 \zeta_+^+ & \zeta_z^+ e^{-i\omega t} & \zeta_-^+ e^{-2i\omega t} & \zeta_2^+ e^{i\omega t} & \zeta_1^+ & \zeta_0^+ e^{-i\omega t} & \zeta_{-1}^+ e^{-2i\omega t} & 0 \\
 \zeta_+^z e^{i\omega t} & \zeta_z^z & \zeta_-^z e^{-i\omega t} & \zeta_2^z e^{2i\omega t} & \zeta_1^z e^{i\omega t} & \zeta_0^z & \zeta_{-1}^z e^{-i\omega t} & \zeta_{-2}^z e^{-2i\omega t} \\
 \zeta_+^- e^{2i\omega t} & \zeta_z^- e^{i\omega t} & \zeta_-^- & 0 & \zeta_1^- e^{2i\omega t} & \zeta_0^- e^{i\omega t} & \zeta_{-1}^- & \zeta_{-2}^- e^{-i\omega t} \\
 \zeta_+^2 e^{-i\omega t} & \zeta_z^2 e^{-2i\omega t} & 0 & \zeta_2^2 & \zeta_1^2 e^{-i\omega t} & \zeta_0^2 e^{-2i\omega t} & 0 & 0 \\
 \zeta_+^1 & \zeta_z^1 e^{-i\omega t} & \zeta_-^1 e^{-2i\omega t} & \zeta_2^1 e^{i\omega t} & \zeta_1^1 & \zeta_0^1 e^{-i\omega t} & \zeta_{-1}^1 e^{-2i\omega t} & 0 \\
 \zeta_+^0 e^{i\omega t} & \zeta_z^0 & \zeta_-^0 e^{-i\omega t} & \zeta_2^0 e^{2i\omega t} & \zeta_1^0 e^{i\omega t} & \zeta_0^0 & \zeta_{-1}^0 e^{-i\omega t} & \zeta_{-2}^0 e^{-2i\omega t} \\
 \zeta_+^{-1} e^{2i\omega t} & \zeta_z^{-1} e^{i\omega t} & \zeta_-^{-1} & 0 & \zeta_1^{-1} e^{2i\omega t} & \zeta_0^{-1} e^{i\omega t} & \zeta_{-1}^{-1} & \zeta_{-2}^{-1} e^{-i\omega t} \\
 0 & \zeta_z^{-2} e^{2i\omega t} & \zeta_-^{-2} e^{i\omega t} & 0 & 0 & \zeta_0^{-2} e^{2i\omega t} & \zeta_{-1}^{-2} e^{i\omega t} & \zeta_{-2}^{-2}
 \end{array} \right]$$

$$+ \left[ \begin{array}{ccc|ccc}
 \eta_+^+ & \eta_z^+ e^{-i\omega t} & 0 & 0 & 0 & 0 & 0 & 0 \\
 \eta_+^z e^{i\omega t} & \eta_z^z & \eta_-^z e^{-i\omega t} & 0 & 0 & 0 & 0 & 0 \\
 0 & \eta_z^- e^{i\omega t} & \eta_-^- & 0 & 0 & 0 & 0 & 0 \\
 0 & 0 & 0 & \eta_2^2 & \eta_1^2 e^{-i\omega t} & 0 & 0 & 0 \\
 0 & 0 & 0 & \eta_2^1 e^{i\omega t} & \eta_1^1 & \eta_0^1 e^{-i\omega t} & 0 & 0 \\
 0 & 0 & 0 & 0 & \eta_1^0 e^{i\omega t} & \eta_0^0 & \eta_{-1}^0 e^{-i\omega t} & 0 \\
 0 & 0 & 0 & 0 & 0 & \eta_0^{-1} e^{i\omega t} & \eta_{-1}^{-1} & \eta_{-2}^{-1} e^{-i\omega t} \\
 0 & 0 & 0 & 0 & 0 & 0 & \eta_{-1}^{-2} e^{i\omega t} & \eta_{-2}^{-2}
 \end{array} \right] (e^{i\omega t} + e^{-i\omega t})$$

The cosine terms on the main diagonal are from  $H'_z$ , and the trick on the super/subdiagonal is for the Bloch-Siegert shift. For the latter case, neglecting the component that gives the second harmonic and keeping the constant is equivalent to neglecting this shift and assuming an actual rotating field.

Let:

$$\langle \tilde{\mathbf{T}}_\xi^{(2)} \rangle = \sum_{n=-\infty}^{\infty} u_{\xi,n} e^{ni\omega t}, \quad \xi \in \{-2, \dots, 2\} \quad \langle \tilde{\mathbf{J}}_\pm \rangle = \sum_{n=-\infty}^{\infty} u_{\pm,n} e^{ni\omega t} \quad \langle \tilde{\mathbf{J}}_z \rangle = \sum_{n=-\infty}^{\infty} u_{z,n} e^{ni\omega t} \quad (5.1)$$

If

$$\vec{\mathbf{u}}_n \equiv \left[ u_{+,n} \quad u_{z,n} \quad u_{-,n} \mid u_{2,n} \quad u_{1,n} \quad u_{0,n} \quad u_{-1,n} \quad u_{-2,n} \right]^T,$$

and

$$\vec{\zeta}_{h,n} \equiv \left[ \zeta_h^+ \delta_{n,-1} \quad \zeta_h^z \delta_{n,0} \quad \zeta_h^- \delta_{n,1} \mid \zeta_h^2 \delta_{n,-2} \quad \zeta_h^1 \delta_{n,-1} \quad \zeta_h^0 \delta_{n,0} \quad \zeta_h^{-1} \delta_{n,1} \quad \zeta_h^{-2} \delta_{n,2} \right]^T,$$

then we have the following system:

$$\begin{aligned}
-\vec{\zeta}_{h,n} = & \left[ \begin{array}{ccc|cccc} \zeta_+^+ - ni\omega & \eta_z^+ & 0 & 0 & \zeta_1^+ & 0 & 0 & 0 \\ \eta_z^+ & \zeta_z^- - ni\omega & \eta_z^- & 0 & 0 & \zeta_0^z & 0 & 0 \\ 0 & \eta_z^- & \zeta_-^- - ni\omega & 0 & 0 & 0 & \zeta_{-1}^- & 0 \\ \hline 0 & 0 & 0 & \zeta_2^2 - ni\omega & \eta_1^2 & 0 & 0 & 0 \\ \zeta_+^1 & 0 & 0 & \eta_2^1 & \zeta_1^1 - ni\omega & \eta_0^1 & 0 & 0 \\ 0 & \zeta_z^0 & 0 & 0 & \eta_1^0 & \zeta_0^0 - ni\omega & \eta_{-1}^0 & 0 \\ 0 & 0 & \zeta_-^{-1} & 0 & 0 & \eta_0^{-1} & \zeta_{-1}^{-1} - ni\omega & \eta_{-2}^{-1} \\ 0 & 0 & 0 & 0 & 0 & 0 & \eta_{-1}^{-2} & \zeta_{-2}^{-2} - ni\omega \end{array} \right] \vec{\mathbf{u}}_n \\
+ & \left[ \begin{array}{ccc|cccc} \eta_+^+ & 0 & 0 & \zeta_2^+ & 0 & 0 & 0 & 0 \\ \zeta_+^z & \eta_z^- & 0 & 0 & \zeta_1^z & 0 & 0 & 0 \\ 0 & \zeta_z^- & \eta_-^- & 0 & 0 & \zeta_0^- & 0 & 0 \\ \hline 0 & 0 & 0 & \eta_2^2 & 0 & 0 & 0 & 0 \\ 0 & 0 & 0 & \zeta_2^1 & \eta_1^1 & 0 & 0 & 0 \\ \zeta_+^0 & 0 & 0 & 0 & \zeta_1^0 & \eta_0^0 & 0 & 0 \\ 0 & \zeta_z^{-1} & 0 & 0 & 0 & \zeta_0^{-1} & \eta_{-1}^{-1} & 0 \\ 0 & 0 & \zeta_-^{-2} & 0 & 0 & 0 & \zeta_{-1}^{-2} & \eta_{-2}^{-2} \end{array} \right] \vec{\mathbf{u}}_{n-1} + \left[ \begin{array}{ccc|cccc} 0 & \eta_z^+ & \zeta_+^+ & 0 & 0 & 0 & \zeta_{-1}^+ & 0 \\ 0 & 0 & \eta_z^- & 0 & 0 & 0 & 0 & \zeta_{-2}^z \\ 0 & 0 & 0 & 0 & 0 & 0 & 0 & 0 \\ \hline 0 & \zeta_z^2 & 0 & 0 & \eta_1^2 & \zeta_0^2 & 0 & 0 \\ 0 & 0 & \zeta_-^{-1} & 0 & 0 & \eta_0^1 & \zeta_{-1}^1 & 0 \\ 0 & 0 & 0 & 0 & 0 & 0 & \eta_{-1}^0 & \zeta_{-2}^0 \\ 0 & 0 & 0 & 0 & 0 & 0 & 0 & \eta_{-2}^{-1} \\ 0 & 0 & 0 & 0 & 0 & 0 & 0 & 0 \end{array} \right] \vec{\mathbf{u}}_{n+2} \\
+ & \left[ \begin{array}{ccc|cccc} \eta_+^+ & \zeta_z^+ & 0 & 0 & 0 & \zeta_0^+ & 0 & 0 \\ 0 & \eta_z^- & \zeta_-^z & 0 & 0 & 0 & \zeta_{-1}^- & 0 \\ 0 & 0 & \eta_-^- & 0 & 0 & 0 & 0 & \zeta_{-2}^- \\ \hline \zeta_+^2 & 0 & 0 & \eta_2^2 & \zeta_1^2 & 0 & 0 & 0 \\ 0 & \zeta_z^1 & 0 & 0 & \eta_1^1 & \zeta_0^1 & 0 & 0 \\ 0 & 0 & \zeta_-^0 & 0 & 0 & \eta_0^0 & \zeta_{-1}^0 & 0 \\ 0 & 0 & 0 & 0 & 0 & \eta_{-1}^{-1} & \zeta_{-2}^{-1} & 0 \\ 0 & 0 & 0 & 0 & 0 & 0 & 0 & \eta_{-2}^{-2} \end{array} \right] \vec{\mathbf{u}}_{n+1} + \left[ \begin{array}{ccc|cccc} 0 & 0 & 0 & 0 & 0 & 0 & 0 & 0 \\ \eta_z^- & 0 & 0 & \zeta_2^z & 0 & 0 & 0 & 0 \\ \zeta_+^- & \eta_z^- & 0 & 0 & \zeta_1^- & 0 & 0 & 0 \\ \hline 0 & 0 & 0 & 0 & 0 & 0 & 0 & 0 \\ 0 & 0 & 0 & \eta_2^1 & 0 & 0 & 0 & 0 \\ 0 & 0 & 0 & \zeta_2^0 & \eta_1^0 & 0 & 0 & 0 \\ \zeta_+^{-1} & 0 & 0 & 0 & \zeta_1^{-1} & \eta_0^{-1} & 0 & 0 \\ 0 & \zeta_z^{-2} & 0 & 0 & 0 & \zeta_0^{-2} & \eta_{-1}^{-2} & 0 \end{array} \right] \vec{\mathbf{u}}_{n-2} \quad (5.2)
\end{aligned}$$

Clearly this is one block-row of an infinite-dimensional block-diagonal system, with block size 8. If one only looks at the equations, it is not obvious how to solve it. Note that  $\vec{\zeta}_{h,n} \neq \mathbf{0}_{8 \times 1}$  iff  $|n| \leq 2$ ; this corresponds to the fact that only DC through the second harmonic actually appears in the inhomogeneous portion. Appealing again to the argument that we cannot physically expect significant contributions for high harmonics, we can choose to solve for some subset of the  $\vec{\mathbf{u}}_n$ 's, where  $|n| \leq m_o$ . When combined with Equation (3.42), we find that  $\alpha(z)$  formally has Fourier components up to  $e^{\pm(m_o+2)i\omega t}$ .

Intuitively, one might expect Fourier components with  $|n| \ll m_o$  (where  $\ll$  is intentionally vague) to be more accurate than the rest. However, for every case tested, solutions of this system seem to yield  $\vec{\mathbf{u}}_n$  components that are numerically indistinguishable for two different values of

$m_o$ , provided both values of  $m_o$  are  $\geq |n|$ . This is some indication that the solution procedure is even more solid than one would expect; i.e., it leads one to suspect that the postulated condition  $|n| \ll m_o$  may be disregarded. When in doubt, however, one can always increase  $m_o$ , where the cost is that of solving a dimension- $(16m_o + 8)$  linear system, a procedure that is usually asymptotically cubic in the matrix dimension.

A diagram for the case of  $m_o = 3$  is shown in Figure 5.1. Note that all blocks on the first superdiagonal are the same, and, similarly, on the second superdiagonal. This is also true of the two subdiagonal rows. However, there are slight differences (due to the  $ni\omega$  terms) in the on-diagonal blocks. Additionally, the right-hand side has been set separately, and the state variables are not shown.

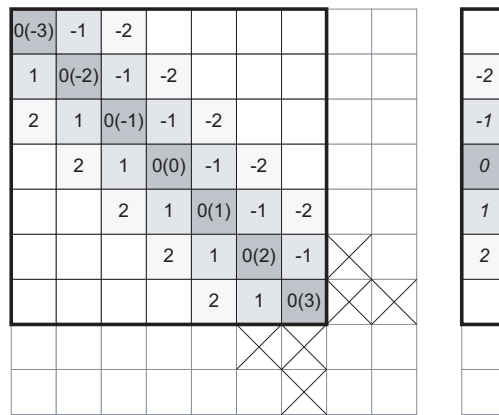


Figure 5.1. Diagram of Matrix Equation Layout for  $m_o = 3$ .

The basic idea is that each additional order introduces two new L-shaped pieces, but then the matrix is truncated on the lower-right to ensure it remains square. For  $m_o = 1$  and  $m_o = 0$ , this reduces conveniently to a  $3 \times 3$  full block diagonal matrix, and a  $1 \times 1$  block diagonal matrix, respectively. In other words, Equation (5.2) corresponds to any one row of Figure 5.1 (or of a similar figure for some other  $m_o$ ).

## 5.2 Examples – Pumping with LCP Light ( $\sigma$ )

This section presents plots, comparisons, and optimizations for the case of circularly-polarized light. Some comparisons are made with the theory of [34].

### 5.2.1 Comparisons With Prior $\sigma$ Theory<sup>12</sup>

In this section, Section 5.2.2, Section 5.3, and Section 5.4, the laser wavelength is assumed to be on (and substantially narrower than) the  $D_0$  line center, and to uniformly fill a 3.61 cm inside diameter, 4.88 cm inside length cell filled with  $^4\text{He}$  to 1.5 Torr. The metastable level is chosen in each case such that, at any large magnetic detuning  $|\gamma H_0 - \omega| \gg 2\pi\tau_c^{-1}$ , 15% of the light is absorbed. In the plots where  $H_1$  strength and/or optical power are independent variables (Figures 5.5, 5.6, 5.7, and 5.8), the metastable density is changed, as described, at every point. In the other plots, both the  $H_1$  amplitude and the metastable density are held fixed, with  $H_1$  always chosen optimally for one orientation, and the metastable density chosen using the same orientation. In this section only, optimization occurs for  $\theta = \phi = \xi = 0^\circ$ , and  $\eta = 90^\circ$ .

Some checks were made to ensure the present model reduces to the previous model, given in [34], where experimental measurements were compared to theory on the basis of the shot noise sensitivity limit. This limit is the photodiode shot noise in  $\text{A}/\sqrt{\text{Hz}}$ , divided by the slope of the magnetic resonance curve, in  $\text{A}/\text{T}$ , at the inflection point. Figure 5.2 illustrates relative transmission in the two cases as a function of detuning in nT; this is a typical  $\sigma$ -pumping magnetic resonance curve. The light intensity into the cell is effectively multiplied by a point on this curve, and the product is measured on the photodiode. Figure 5.3 is simply the slope of the curves shown in Figure 5.2, but is an important intermediate step.

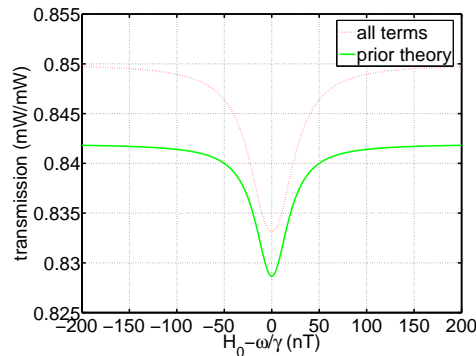


Figure 5.2. Resonance curve for typical circularly-polarized configuration at 0.5 mW input power, divided by the input power. The metastable densities, rather than the nominal absorptions, are equal.

<sup>12</sup>A significant portion of the text of this section is based on [43], © 2010 American Physical Society.

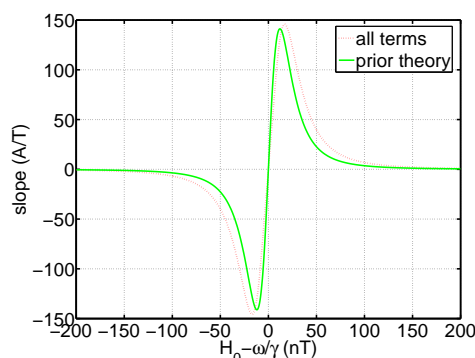


Figure 5.3. Slope of resonance curve for typical circularly-polarized configuration at 0.5 mW input power. The metastable densities, rather than the nominal absorptions, are equal. Note that this is the slope of Figure 5.2, *times* the input power of 0.5 mW, since 0.5 mW had been divided out of Figure 5.2. The sensitivity of the photodiode, assumed to be about 0.68 A/W, is also included.

Figure 5.4 shows the shot noise sensitivity limit as a function of the detuning of the  $H_1$  frequency  $\omega$  from the precession frequency in the ambient field, but later plots will only display the sensitivity at a minimum of such a curve, or at the maximum of a curve like those in Figure 5.3, since this is the optimum operating point. To the printed precision, the curves are symmetric, so we will always display whichever inflection point gives a positive slope. Note that the shot noise sensitivity limit is simply the shot noise divided by the slope, so we will usually only show one or the other. Observe in Figure 5.4 that the optimum sensitivity prediction for a typical configuration agrees to about 3%, although the required detuning predicted in order to achieve this differs by closer to 25%.

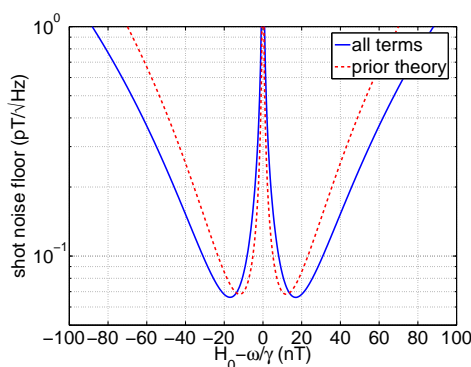


Figure 5.4. Shot-noise sensitivity limit for typical circularly-polarized configuration at 0.5 mW input power. The metastable densities, rather than the nominal absorptions, are equal. (from [43], © 2010, American Physical Society)

Figure 5.5 shows the dependence of sensitivity on laser power and  $H_1$  amplitude. Each grid point has a corresponding point in Figure 5.6 showing the frequency detuning at the positive inflection point. Each power level has a separate metastable density chosen to ensure 15% nominal absorption. One sees in Figure 5.5 that there is an optimal  $H_1$  amplitude for each power, displayed separately in Figure 5.7. If this optimal  $H_1$  amplitude is overlaid across Figure 5.5, a simpler plot of sensitivity as a function of power results, shown in Figure 5.8. The prior results of [34] are shown on this plot, as well.

Figure 5.4 corresponds to a point at the far left of Figure 5.8. The models agree less at higher powers, and this is relevant in light of recent advances in high-power 1083 nm lasers. Figures 5.7 and 5.8 are important from an instrument design perspective, since the former allows one to quickly determine how accurately the laser power must be adjusted for a given sensitivity tolerance, and the latter is a guide to choosing the  $H_1$  amplitude afterwards. It is interesting to note that, at low power, a vertical slice of Figure 5.6 shows optimal detuning is approximately a linear function of  $H_1$  amplitude, but at the upper end of the displayed power scale, the optimal detuning is not even a monotonic function of  $H_1$  amplitude. This gives an indication of the value of this rigorous theoretical analysis in designing magnetometer instruments.

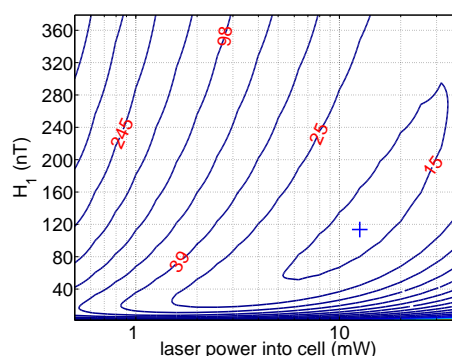


Figure 5.5. Shot-noise floor ( $\text{fT}/\sqrt{\text{Hz}}$ ) for typical circularly-polarized configuration over laser power and  $H_1$  strength. The cross marks the optimum. (from [43], © 2010, American Physical Society)

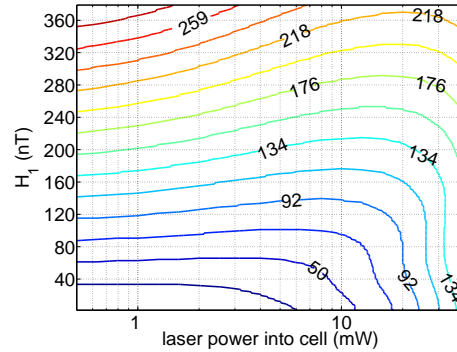


Figure 5.6. Detuning of magnetic ( $H_0 - \omega/\gamma$ ) inflection point (nT), circularly-polarized light, over laser power and  $H_1$  strength. (from [43], © 2010, American Physical Society)

In Figures 5.7 and 5.8, the metastable densities are chosen identically to those in Figures 5.5 and 5.6, which, in turn, use all the terms added to the model presented here. This means that the “prior theory” traces have the same metastable density for a given power level as the “all terms” traces, but not the same absorption level. The metastable density is a more fundamental quantity, since the optical absorption depends not only on the metastable density  $n_S$ , but also, indirectly through the metastable polarization  $\vec{V}$ , on the photon flux density  $\Phi$ .

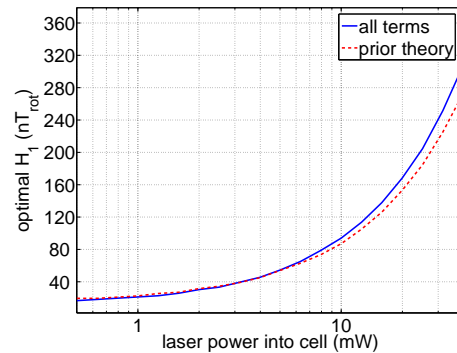


Figure 5.7. Optimal  $H_1$  amplitude as a function of laser power, circularly-polarized light. (from [43], © 2010, American Physical Society)

Figure 5.8 has an optimum (and would even if  $H_1$  had been constant for the entire plot) because of two competing effects. Since rms shot noise increases as the square root of power, but signal strength increases proportionally to the power, higher powers tend to improve the signal-to-noise ratio; this effect dominates in the left half of the plot. However, at higher power levels, the longitudinal and transverse relaxation time constants  $\tau_1$  and  $\tau_2$  (see Section 4.1) become shorter

and the metastable polarization is degraded, causing the slopes of the magnetic resonance curves to decrease and the linewidth to increase; this latter effect is referred to as light broadening. Note that shot noise is not the only source of noise, and some experimental fine-tuning is required to find the optimal power, but such a figure provides a good initial estimate, reducing the effort and allowing the choice of an appropriate *range* of tuning for the electronics design.

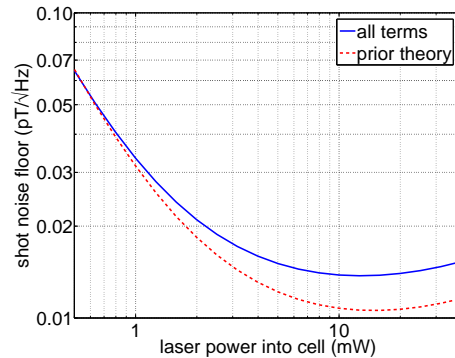


Figure 5.8. Shot-noise sensitivity limit for typical circularly-polarized configuration over laser power, with  $H_1$  amplitude picked optimally as a function of laser power. (from [43], © 2010, American Physical Society)

### 5.2.2 Three Cells

One of the principal advantages of a scalar sensor (as most optically-pumped magnetometers, helium and otherwise<sup>13</sup>, are) is that there is no need to combine several vector component sensors with an estimate of the system orientation [17]. Because the signal slope in a  $^4\text{He}$  double-resonance magnetometer using circularly-polarized light follows an approximate dependence of  $\cos^2 \phi$ , the natural way to achieve isotropic sensitivity is to simply add the signals from three orthogonal cells [23].

However, we now show that such an approach is only approximate, as the relation  $\cos^2 \phi$  is less accurate for  $\phi \sim \pi/2$ : there is nonzero signal at this angle, as illustrated experimentally in Section 6.3. Therefore, it is desirable to know exactly how much such a configuration deviates from isotropic sensitivity. Figure 5.9 shows the optimum slope of the sum of the 3 cells' magnetic resonance curves over all orientations, where each cell receives 0.5 mW of optical power and runs

<sup>13</sup>Note, though, that because  $^4\text{He}$  lacks a nuclear spin,  $^4\text{He}$  is the only practical pumping medium the author is aware of where angular velocity of the magnetometer is not a significant source of error.

at 15% absorption. While the slopes are relatively consistent, ranging from about 164–184 A/T, they are not uniform. The conversion to a shot noise floor can be found by dividing the slope into  $17 \text{ pA}/\sqrt{\text{Hz}}$ , giving about  $\sim 100 \text{ fT}/\sqrt{\text{Hz}}$ . The optimal detuning corresponding to each orientation is displayed in Figure 5.10, and ranges from about 14–20 nT.

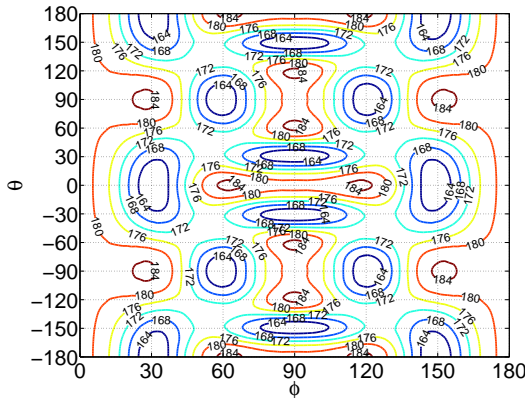


Figure 5.9. Slope of sum of 3 photodiodes' signals (A/T).

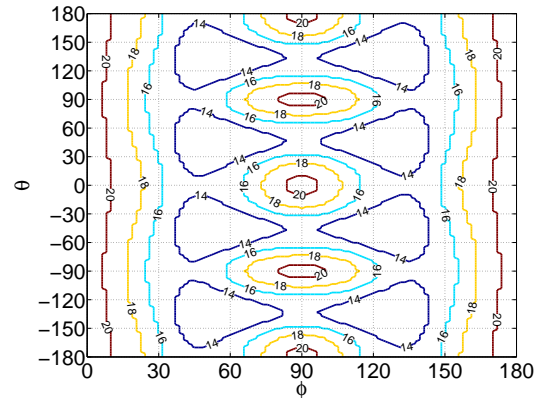


Figure 5.10. Optimal detuning (nT) for sum of 3 photodiode signals.

Corresponding curves for the individual cells are shown in Figures 5.11–5.16. In these cases, the conversion factor to shot noise is  $\sqrt{3}$  smaller, giving an optimum of about  $64 \text{ fT}/\sqrt{\text{Hz}}$ , at the expense of having some orientations where the sensitivity is nonexistent. These latter regions are where  $H_1$  is parallel to  $H_0$ , where  $|\theta| = \phi = \pi/2$ . Prior theory lacked the constraint on  $\theta$ . Since the slope ranges from about 0–10 A/T in the new model, some orientations with  $\phi = \pi/2$  achieve shot noise floors as low as about  $1 \text{ pT}/\sqrt{\text{Hz}}$ . Note also that the optimal detunings vary considerably more, as well, from about 9–27 nT.

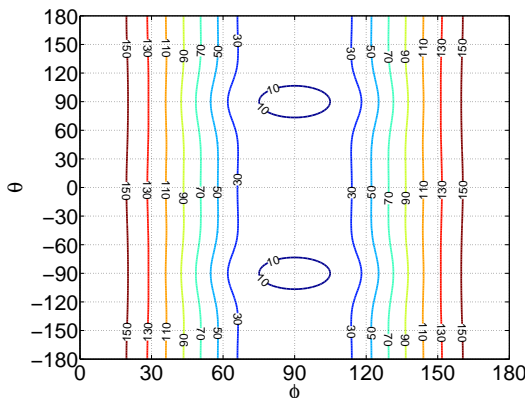


Figure 5.11. Slope of signal from cell 1 (A/T).

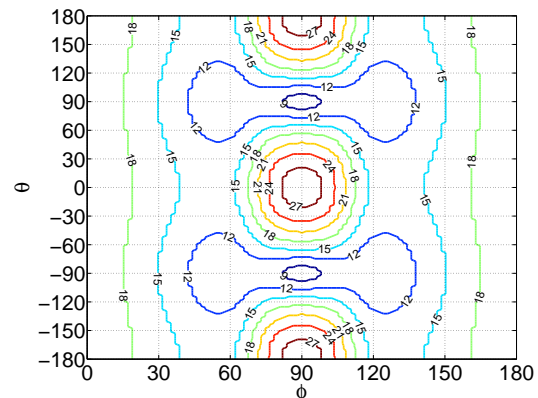


Figure 5.12. Optimal detuning (nT) when using only cell 1.

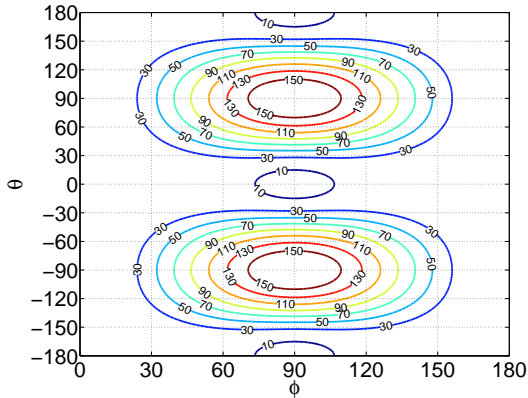


Figure 5.13. Slope of signal from cell 2 (A/T).

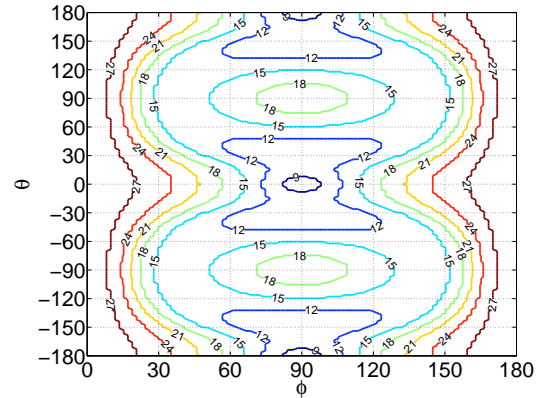


Figure 5.14. Optimal detuning (nT) when using only cell 2.

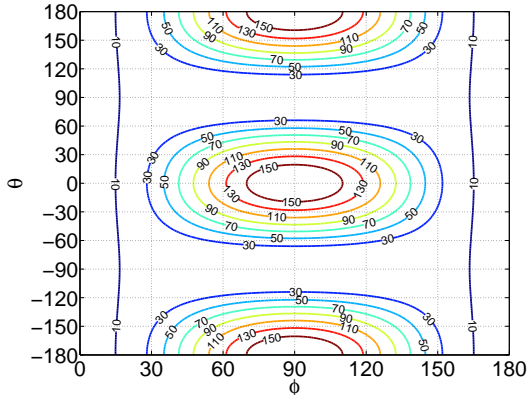


Figure 5.15. Slope of signal from cell 3 (A/T).

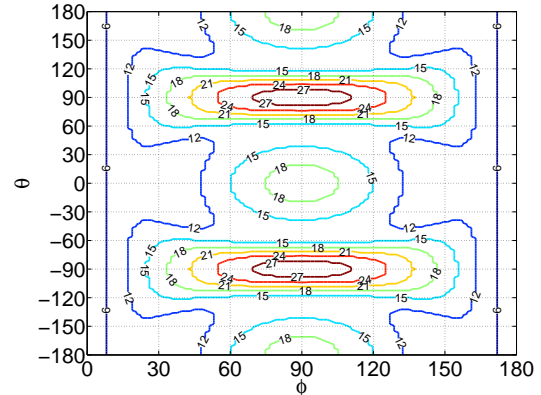


Figure 5.16. Optimal detuning (nT) when using only cell 3.

### 5.3 Examples – $H_1$ Improvements for Linearly-Polarized Pumping Light<sup>14</sup>

In this section, the metastable density and optimal  $H_1$  amplitude are chosen for  $\theta = \phi = \eta = 90^\circ$ .  $\eta$  and  $\xi$  do not affect the choice of metastable density, but they do affect the optimal  $H_1$  amplitude, so plots with  $\xi = 90^\circ$  have a different optimal  $H_1$  amplitude than plots with  $\xi \approx 54.7^\circ$ . This is reasonable for the particular orientation in question, since, to a first approximation (ignoring the  $H'_z$  component in Equation (3.38)), the effective  $H_1$  amplitude is the amount of  $H_1$  perpendicular to  $H_0$ , and so the actual  $H_1$  amplitude must be increased for the latter choice of  $\xi$ .

<sup>14</sup>A significant portion of the text of this section is based on [43], © 2010 American Physical Society.



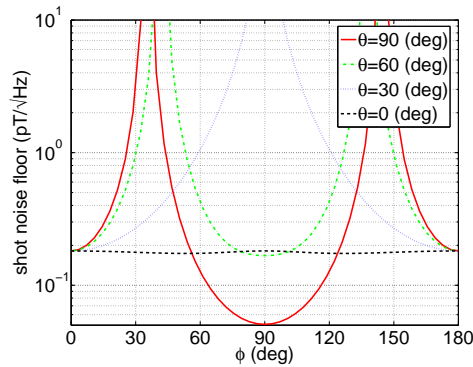


Figure 5.19. Shot-noise floor for selected values of  $\theta$ , at 0.5 mW optical power, linearly-polarized light,  $\xi \approx 54.7^\circ$ . (from [43], © 2010, American Physical Society)

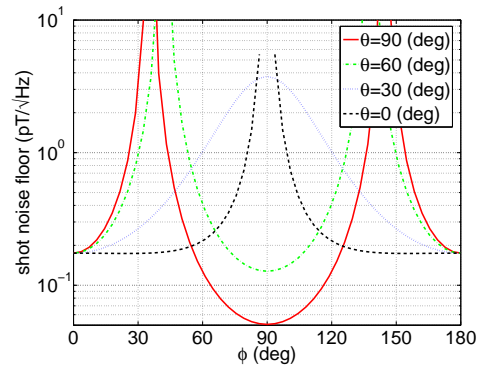


Figure 5.20. Shot-noise floor for selected values of  $\theta$ , at 0.5 mW optical power, linearly-polarized light,  $\xi = 90^\circ$ . (from [43], © 2010, American Physical Society)

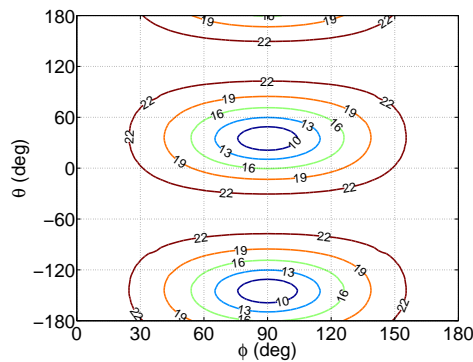


Figure 5.21. Detuning of magnetic ( $H_0 - \omega/\gamma$ ) inflection point (nT), at 0.5 mW optical power, linearly-polarized light,  $\xi \approx 54.7^\circ$ . (from [43], © 2010, American Physical Society)

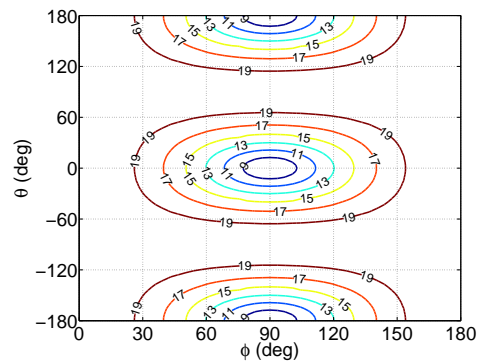


Figure 5.22. Detuning of magnetic ( $H_0 - \omega/\gamma$ ) inflection point (nT), at 0.5 mW optical power, linearly-polarized light,  $\xi = 90^\circ$ . (from [43], © 2010, American Physical Society)

The most sensitive area for linearly-polarized light is with  $\phi = 90^\circ$  and  $\theta = \pm 90^\circ$ , where the light polarization vector is along  $H_0$ , as shown in Figures 5.17 and 5.18. However, a reasonably sensitive region of operation is also available with  $\phi = 0$  or  $180^\circ$ , and, at least in the  $\xi \approx 54.7^\circ$  case, the  $\theta = 0, 180^\circ$  slices also remain flat and sensitive. The comparison of Figures 5.19 and 5.20 illustrates even better that much stays the same with the change in  $\xi$ , but that the  $\theta = 0$  slice

becomes rather flat in the former. In contrast, comparing the region from  $\phi \approx 60^\circ$  to  $120^\circ$  in Figures 5.19 and 5.20 merely indicates a further degradation in performance for  $\theta = 30^\circ$ .

Finally, the levels of magnetic detuning required to achieve the best sensitivity in each orientation appear in Figures 5.21 and 5.22. Note that the “low detuning” areas shift with the orientation of  $H_1$ , rather than with the orientation of the optical polarization, unlike the areas of high sensitivity, shown previously, which remained aligned with the optical polarization. Figures 5.21 and 5.22 also show that the resonance is slightly broader in the  $\xi \approx 54.7^\circ$  case, but, from Figures 5.17 and 5.18, one finds that the sensitivity is nevertheless similar. Many omnidirectional designs require multiple cells, and these curves argue that using  $\xi \approx 54.7^\circ$  will facilitate the development of an omnidirectional sensor design using linearly polarized light.

#### 5.4 Examples – Bloch-Siegert and Virtual Light Shifts<sup>15</sup>

A common technique [58] in magnetic resonance is to treat the experimental oscillating field as a rotating field, which is mathematically equivalent to only keeping the constant terms of  $\mathbf{A}_4$ . The magnitude [8] of the first-order apparent shift for a spin-1/2 system is  $H_1^2/(4H_0)$ , in our notation. Applying this to typical values of  $H_1 \approx 17$  nT and  $H_0 \approx 50$   $\mu$ T, the calculations in Figure 5.23 show good agreement.

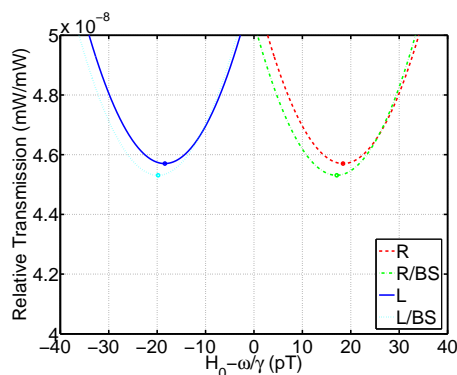


Figure 5.23. Virtual light shift and Bloch-Siegert (BS) shift, at 0.5 mW optical power. The shifts are about 18.5 pT and 1.4 pT, respectively. The vertical scale is the transmission ratio minus 0.8322443, chosen to make the scale legible. “L” indicates left-circular polarization, and “R” indicates right-circular polarization. The traces labeled (BS) assume the more realistic oscillating field, rather than a rotating field. (from [43], © 2010, American Physical Society)

<sup>15</sup>A significant portion of the text of this section is based on [43], © 2010 American Physical Society.

Shown in Figure 5.23 are the troughs of the four magnetic resonance curves for the two circular polarizations, with and without accounting for the Bloch-Siegert shift. Comparing the curves with and without the Bloch-Siegert shift gives an estimate of 1.4 pT for that effect. For terrestrial applications, the Bloch-Siegert shift is small. However, the Bloch-Siegert shift is of interest in space applications, where the  $H_0$  field is low enough for the effect to have a greater impact on absolute magnetometer accuracy than in Figure 5.23.

Also shown in Figure 5.23 is the virtual light shift. The numerical value of the virtual light shift can be calculated from this plot because the sign of the light shift reverses when the direction of the circular polarization reverses [50]. The minimum of the resonance curve for right-handed polarization is at  $-19.8$  pT. Similarly, the minimum of the resonance curve for left-handed polarization is at  $17.1$  pT. Thus, the virtual light shift in this example is  $\approx 18.5$  pT.

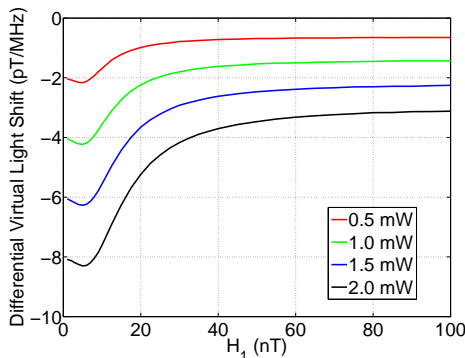


Figure 5.24. Derivative of virtual light shift with respect to laser frequency  $\omega'$ , as a function of  $H_1$  strength. Each trace was evaluated at a different input laser power level. (from [43], © 2010, American Physical Society)

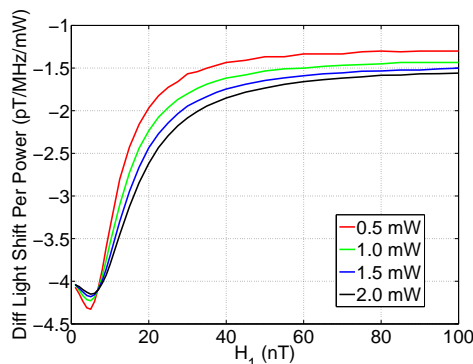


Figure 5.25. Derivative of virtual light shift with respect to laser frequency  $\omega'$ , divided by input optical power. Computed as a function of  $H_1$  strength. Each trace was evaluated at a different input laser power level.

The virtual light shift is important in any system pumped with circularly-polarized laser light, because it transforms laser relative intensity noise (RIN) into a magnetic noise that slightly degrades magnetometer sensitivity. Often, in the case of circularly-polarized pumping light, a larger contribution to magnetometer sensitivity degradation results from the conversion of laser frequency noise by the virtual light shift into a transmitted optical amplitude noise.

Figure 5.24 shows this conversion factor for several input optical powers. Figure 5.25 shows the same data with the input power level divided out, and illustrates that, for most  $H_1$  amplitudes, the conversion factor grows in strength slightly sublinearly with respect to input laser power. Figure 5.24 illustrates that, in order to yield an acceptably-low virtual light shift noise, it is desirable to choose an  $H_1$  amplitude above the value that optimizes other constraints, such as shot noise sensitivity. This tradeoff is more important in magnetometers where the light shift noise plays a more dominant role, such as when magnetometers are miniaturized.

## CHAPTER 6

### EXPERIMENTAL DATA

This section presents experimental data for pumping with linearly-polarized light and circularly-polarized light in several orientations. Theoretical comparisons to the data are also made, without fitting in both cases (Sections 6.1 and 6.3), as well as with fitting in the linearly-polarized case (Section 6.2).

#### 6.1 Linearly-Polarized ( $\pi$ -Parallel Pumping) Data From 4-12-2010<sup>16</sup>

Resonance curves from a 2.44 cm inside diameter, 7.52 cm inside length Pyrex cell filled to 1.5 Torr were collected using the  $\theta = \phi = \eta = \xi = \pi/2$ ,  $\epsilon = 0$  configuration. The measurements took place in a nonmagnetic test facility operated by Polatomic, Inc. and routinely used for the characterization of commercial and advanced magnetometers. The apparatus was arranged such that the error in declination was below 4 deg, and the error in the dip angle was less than 1 deg. The 4.05 mW laser light was swept in a  $\sim 10$  kHz triangle wave across the  $D_0$  absorption line and locked to the line center, and the photodiode data was logged at a 1 kHz sampling rate using a custom preamplifier with a 2000 V/A transimpedance. The photodiode sensitivity was 0.815 A/W.

The experimental configuration follows Figure 2.1, and the measurements were taken with the coil control open loop. The  $H_1$  frequency  $\omega$  was swept linearly across the Larmor frequency  $\gamma H_0$  at a rate of 2 kHz/s. One of the measured resonance curves is shown in Figure 6.1. The “cell off” trace comes from a DC voltmeter measurement of the photodiode preamp output while the cell is extinguished; the actual AC signal (not shown) is significantly shorter than the vertical deviation on the measured resonance curve. The “exper” trace was logged in LabView as a voltage measurement out of the photodiode preamp.

---

<sup>16</sup>A significant portion of the text of this section is based on [43], © 2010 American Physical Society.

Also shown in Figure 6.1 is the theoretical calculation of the magnetic resonance curve based on the treatment presented in Section 5.1. In calculating the theoretical curve in Figure 6.1, we have used our best independent estimates of the experimental values for the parameters required by the model.

Of particular note in this comparison of theory to experiment is the treatment of the laser beam shape and size. The laser beam has an uncorrected astigmatism that, after passing through the various beamsplitters, waveplates, and lenses, causes the profile entering the cell to resemble a capital letter “I.” This is partially corrected for in the model by assuming a fill factor, or effective beam radius, where only the atoms within that cylindrical cross section are assumed to be pumped. A previous experiment has been used to estimate the effective beam radius by measuring the light broadening of the magnetic resonance line as the laser intensity was varied, and we found an approximate beam radius of 1.3 cm. This 53% fill has been used in the plots below, and was not fit to the logged data set shown here. We have used our best experimental estimates of the various model parameters, known to have substantial uncertainty in some cases, to generate the theoretical curves in Figures 6.1 and 6.2.

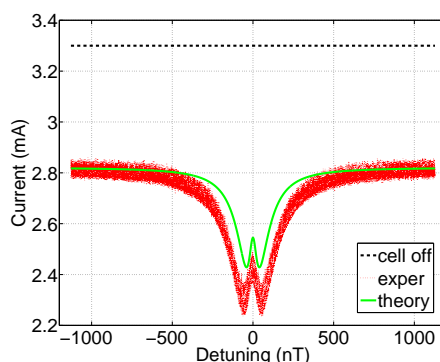


Figure 6.1. Comparison of theoretical and experimental magnetic resonance curves at  $H_1 \approx 52$  nT. The photocurrent with no RF excitation is shown as a reference. (from [43], © 2010, American Physical Society)

The experiment was repeated for 19 different  $H_1$  amplitudes in the range 12–237 nT. In Figure 6.2 are plotted the slopes at the inner and outer inflection points of the experimental magnetic resonance curves. The theoretical calculation of the slopes versus  $H_1$  amplitude is also plotted in Figure 6.2, again using the best independent estimate of the experimental values for the parameters

required by the model. In this light, the agreement between theory and experiment is reasonable, given the uncertainty in the experimental conditions.

From this data, approximate shot noise sensitivities can be obtained by dividing the photocurrent shot noise ( $30 \text{ pA}/\sqrt{\text{Hz}}$ ) by each slope. This suggests an experimental optimum shot noise contribution to sensitivity of around  $6 \text{ fT}/\sqrt{\text{Hz}}$ , which is within 1% of the theoretical optimum.

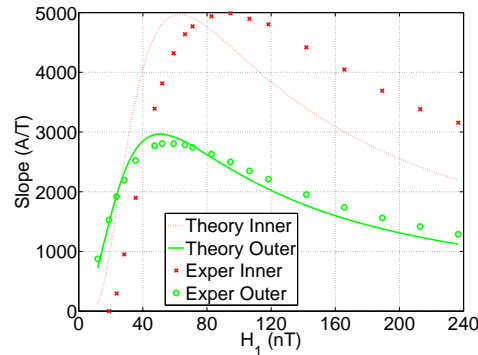


Figure 6.2. Comparison of theoretical and experimental slopes at the inflection points of magnetic resonance curves with varying  $H_1$  amplitude. (from [43], © 2010, American Physical Society)

The large ripple on the experimental trace in Figure 6.1 is likely due to the laser wavelength modulation, and is, in any case, representative of the level measured on the other 18 recorded traces. Even with a heavy amount of smoothing (not shown), it is not possible to directly extract the slopes at the inflection points. However, Equation (4.4) fits both the data and a heavily smoothed version of the data extremely well, to the point that it is likely there is not a function that could visibly improve the fit.

With this in mind, the procedure for extracting the slopes proceeded as follows. Data was cropped to one half cycle of the  $H_1$  detuning triangle wave, and an auto-convolution procedure was used to remove a coarse estimate of the magnetic resonance line center, to an accuracy typically better than about 4 nT. A modified form of Equation (4.4) was fit twice, once to Savitzky-Golay [45] smoothed data, and once to the original data, using the first fit as initial conditions to the second. The modification to Equation (4.4) was simply to allow for an additional fine offset in the resonance center frequency that could not be removed by the initial auto-convolution procedure. The fit was to the ratio of two even quartics, but with an offset in the horizontal direction. One

realizes that the even order is dictated by the axis of symmetry on the data, and that the choice of order four is simply a sufficiently-large choice to support the number the peaks and troughs in the data. Therefore, while the form of the curve used to extract the slopes was inspired by theoretical considerations, it is nevertheless a neutral mathematical device for parametric approximation of functions. Note also that the extraction of the slopes does *not* use the transformation of Equation (4.6), since the model parameters are not necessary to determine slopes and linewidths, and such a transformation could possibly bias the results.

It is important to reiterate that the results of this fit were used only to estimate the *experimental* slope of each resonance curve, and that the fit itself is not shown in this section. *Theoretical* curves based on the new model were generated independently, and without any fitting in this section. To emphasize this independence, a separate section, Section 6.2, describes theoretical fits.

## 6.2 Fits to Data with Linearly-Polarized Light

This section describes the results of fitting the models of Section 4.2 and Chapter 4.3 to the data of Section 6.1, rather than using independent experimental estimates of the parameters.

Figures 6.3–6.21 show data and fits for the experiment described in Section 6.1. Each plot is for a different  $H_1$  amplitude. The data traces have been cropped, centered, and had their units converted. The ripple is of approximately the same magnitude in all plots, but the resonance curve grows deeper and broader as  $H_1$  increases. Note that these two effects combine to give an optimum slope at interior  $H_1$  values, as shown in Figure 6.2. More traces were collected in the vicinity of the two optimum  $H_1$  values than in other areas.

The fitting procedure is as follows: first the procedure in Section 4.2 is followed to obtain a rational function inside an exponential, in the form described in Equation (4.5). Then, a range of values for the beam radius, optical power input, and augmentation factor for the discharge model's  $\tau_c$  are chosen, and used to calculate the metastable density  $n_S$ , the actual value of  $\tau_c$ , the photon flux density  $\Phi$ , and the value of the relaxation time constant  $\tau_0$  for the  $\langle T_0^{(2)} \rangle$  state. The minimum and maximum values of  $n_S \tau_0 \Phi$  obtained were used to seed the following iterative procedure.

Several values in the chosen range were used to carry out the transformation of Equation (4.6), and Equations (4.7) were solved for each value. Because, for this procedure, the theoretically-required equation  $3\tau_0^{-1} = 4\tau_2^{-1} - \tau_1^{-1}$  seems to always have a single well-defined root, a bracketing and iterative refinement procedure was used to narrow the appropriate value of  $n_S\tau_0\Phi$  down until the relative discrepancy in  $\tau_0$  was better than  $10^{-13}$ ; note that this is really not the dominant source of any discrepancies, and that the tight tolerance was used simply because it ran fast enough and so there was no need to loosen it. The best value of  $n_S\tau_0\Phi$  was used to calculate the metastable density  $n_S$  from knowledge of the absorption percentage, about 15% in the data considered here. Using  $n_S$  and the fit  $\tau_0$ , simple division returns the photon flux density  $\Phi$ .

Next, a range of optical power levels is compared against the photon flux density to determine a self-consistent range of beam radii. A bracketing algorithm, using linear interpolation to subdivide the interval on each iteration, was used to optimize the value of  $\tau_c$  such that the absorption level would be correct. This algorithm was repeated for each power level considered until the relative error in absorption was under  $10^{-6}$ . No single beam-radius/power-level pair performed noticeably better than another according to this error metric, so we are limited to specifying results in terms of photon flux density, which neatly consolidates the dependence of the two values.

The “trivial fit” trace in Figures 6.3–6.21 shows the results when the  $H_1, \tau_0, \tau_1$ , and  $\tau_2$  values obtained above via Equations (4.7) are directly substituted into the other resonance curve formulas of Section 4.2. Note that it appears to bisect the ripple on the data in some sense. The values for the “model” trace come from the formulas  $\tau_{0,1,2}^{-1} = \tau_c^{-1} + \Phi Q_{B0,B1,B2}$ , where  $\tau_c$  and  $\Phi$  are the results of the postprocessing just described. These values seem to have an additional constraint not yet identified, so, while the fit is acceptable, it is not as close as the “trivial fit” plots. The fit is a clear improvement over the results of Figure 6.1, where experimental parameters were not fit. The “model” traces based on Section 4.2 indistinguishably overlaid the results based on the model of Chapter 5, so only one “model” is shown. Because a value needed to be chosen from the list of power levels and beam radii, we chose the pair closest to the value of beam radius used in Section 6.1.

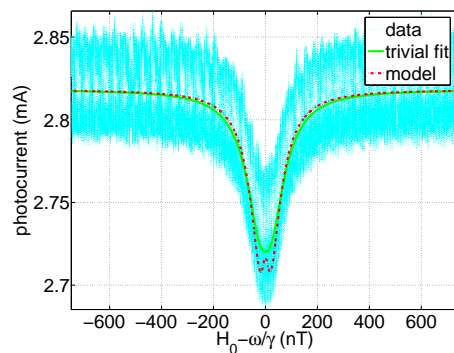


Figure 6.3. Comparison of theoretical fit to experimental magnetic resonance curves, for  $H_1 \approx 11.8$  nT.

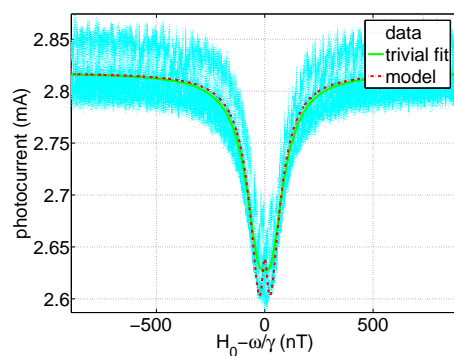


Figure 6.4. Comparison of theoretical fit to experimental magnetic resonance curves, for  $H_1 \approx 18.9$  nT.

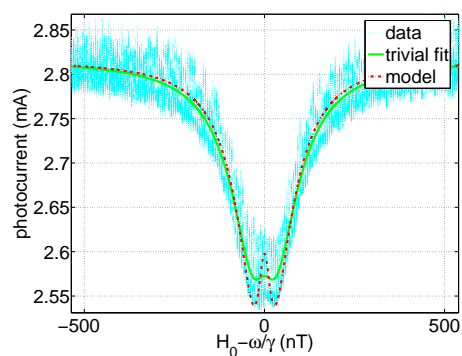


Figure 6.5. Comparison of theoretical fit to experimental magnetic resonance curves, for  $H_1 \approx 23.7$  nT.

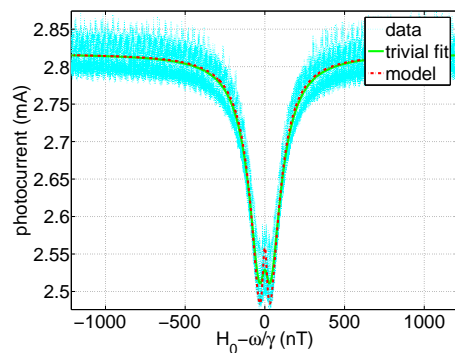


Figure 6.6. Comparison of theoretical fit to experimental magnetic resonance curves, for  $H_1 \approx 28.4$  nT.

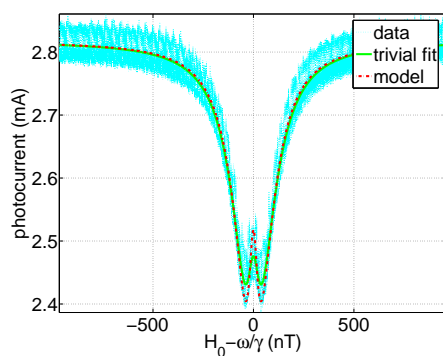


Figure 6.7. Comparison of theoretical fit to experimental magnetic resonance curves, for  $H_1 \approx 35.5$  nT.

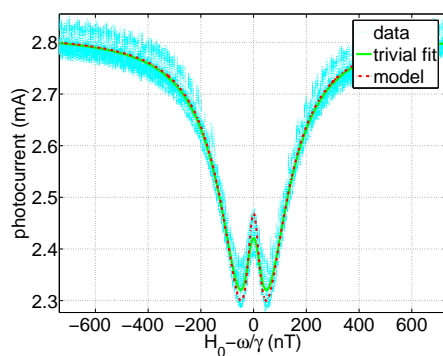


Figure 6.8. Comparison of theoretical fit to experimental magnetic resonance curves, for  $H_1 \approx 47.3$  nT.

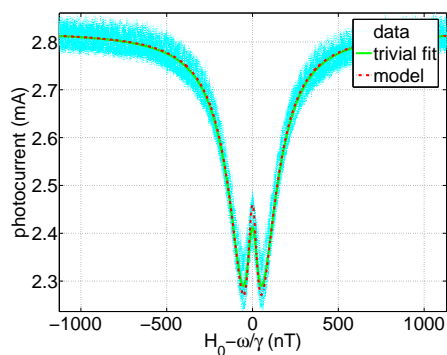


Figure 6.9. Comparison of theoretical fit to experimental magnetic resonance curves, for  $H_1 \approx 52.1$  nT.

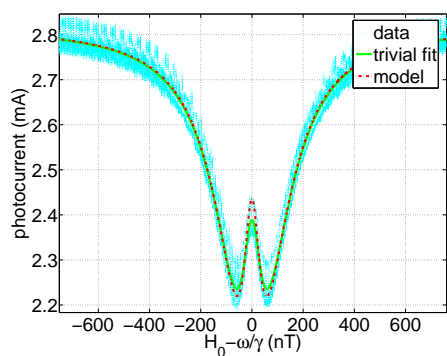


Figure 6.10. Comparison of theoretical fit to experimental magnetic resonance curves, for  $H_1 \approx 59.2$  nT.

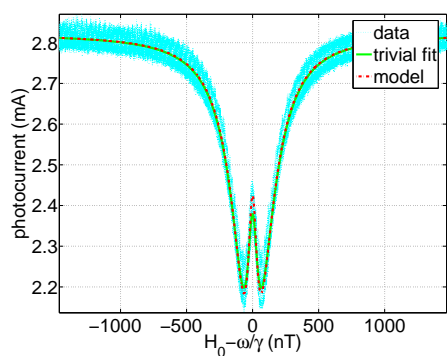


Figure 6.11. Comparison of theoretical fit to experimental magnetic resonance curves, for  $H_1 \approx 66.3$  nT.

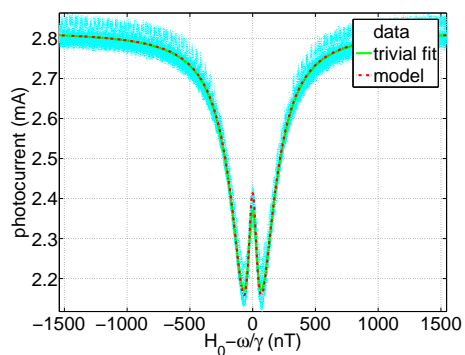


Figure 6.12. Comparison of theoretical fit to experimental magnetic resonance curves, for  $H_1 \approx 71.0$  nT.

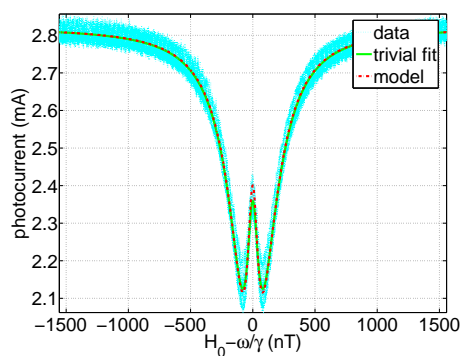


Figure 6.13. Comparison of theoretical fit to experimental magnetic resonance curves, for  $H_1 \approx 82.8$  nT.

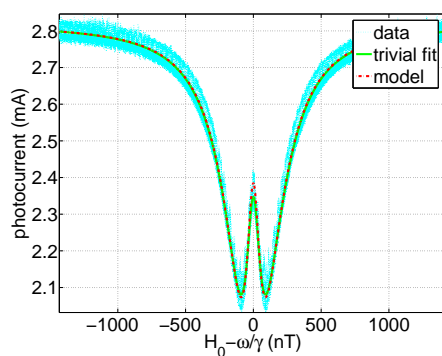


Figure 6.14. Comparison of theoretical fit to experimental magnetic resonance curves, for  $H_1 \approx 94.6$  nT.

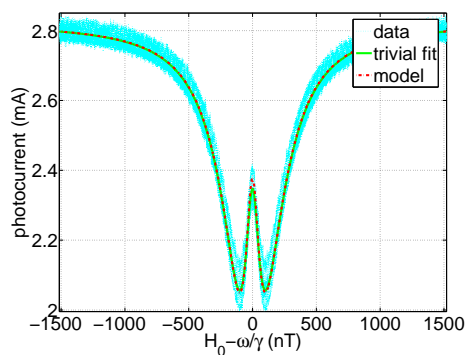


Figure 6.15. Comparison of theoretical fit to experimental magnetic resonance curves, for  $H_1 \approx 106.5$  nT.

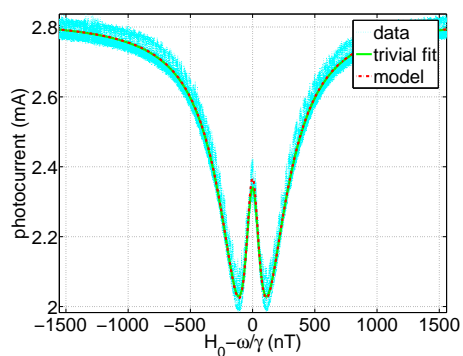


Figure 6.16. Comparison of theoretical fit to experimental magnetic resonance curves, for  $H_1 \approx 118.3$  nT.

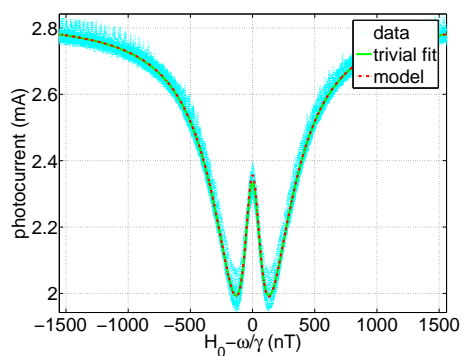


Figure 6.17. Comparison of theoretical fit to experimental magnetic resonance curves, for  $H_1 \approx 142.0$  nT.

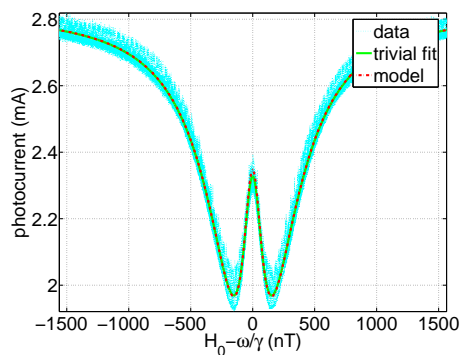


Figure 6.18. Comparison of theoretical fit to experimental magnetic resonance curves, for  $H_1 \approx 165.6$  nT.

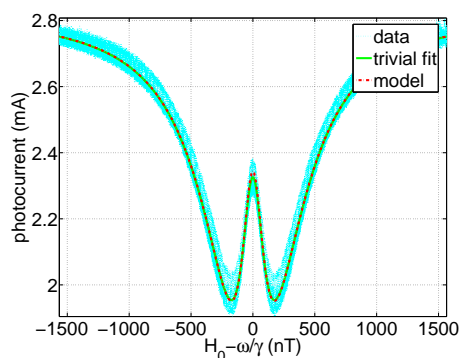


Figure 6.19. Comparison of theoretical fit to experimental magnetic resonance curves, for  $H_1 \approx 189.3$  nT.

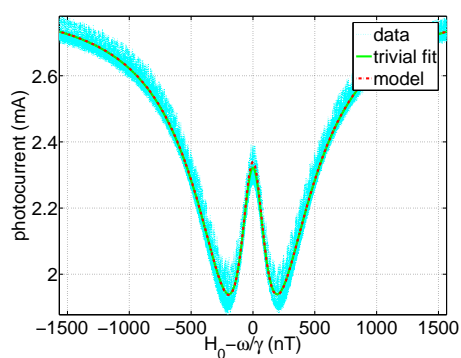


Figure 6.20. Comparison of theoretical fit to experimental magnetic resonance curves, for  $H_1 \approx 213.0$  nT.

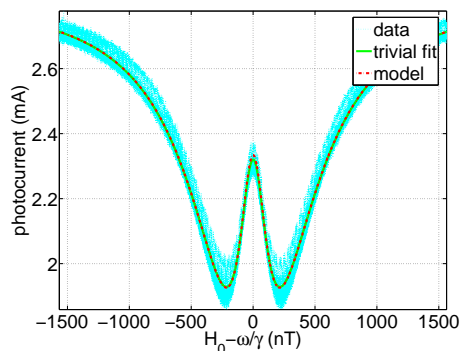


Figure 6.21. Comparison of theoretical fit to experimental magnetic resonance curves, for  $H_1 \approx 236.6$  nT.

The values of the  $H_1$  field are subject to some experimental uncertainty. A function generator drove a 1.4 MHz signal over terminated coaxial cable in excess of a hundred feet to a pair of Helmholtz coils. Measurements of the dimensions of the coils yielded an approximate conversion factor from the voltage to the field in nT, ignoring small gradients in the field. The ordinate of Figure 6.22 shows the fit values of the  $H_1$  field, obtained as a by-product of the fitting procedure above. Except at the lowest couple points, there is a clean proportionality between the two traces, so it is possible that some properties of the coil setup were not modeled properly in the conversion factor we determined. The captions for Figures 6.3–6.21 use the experimentally-inferred  $H_1$  value as their distinctive label, rather than the fit value.

Because  $\tau_c$  and  $\Phi$  are not expected to be a function of  $H_1$  amplitude, nor are the cross sections  $Q_{B1}$  or  $Q_{B2}$ , the theory predicts the value of  $\tau_{0,1,2}$  to be constant, as well. That said, the implications of an effective beam radius are poorly-understood, and so it is certainly possible that it may vary, causing  $\Phi$  to also vary. Additionally, Slichter [58] describes the phenomenon of  $H_1$  broadening. All three traces in Figure 6.23, showing fit values of  $\tau_0^{-1}$ ,  $\tau_1^{-1}$ , and  $\tau_2^{-1}$ , show linewidth broadening as  $H_1$  increases. The (constant) predicted values of these three quantities are also shown in the figure.

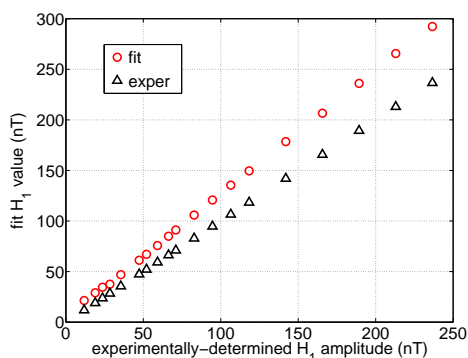


Figure 6.22. Fit of  $H_1$ , compared to the value of  $H_1$  inferred from measurements of coil voltage, termination, shape, and size.

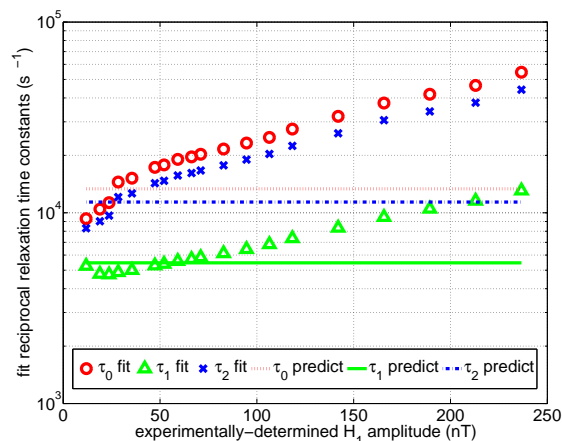


Figure 6.23. Fit of  $\tau_0^{-1}$ ,  $\tau_1^{-1}$ , and  $\tau_2^{-1}$ , as a function of  $H_1$  field amplitude inferred from experimental setup, compared with theory.

### 6.3 LCP ( $\sigma$ -pumping) Data From 5-5-2010

Data was collected in two different orientations from a set of four 0.79 cm inside-radius by 1.8 cm inside-length cells (cells A, C, D, and F) at a pressure of 9 torr, each of which received circularly-polarized light. The four cells all received the same  $H_1$  amplitude and  $H_1$  frequency at any given moment. The  $H_1$  frequency was swept sinusoidally in time, unlike in the experiment of Section 6.1, where the frequency had been modulated by a triangle wave. The effective beam radius is estimated to be near 51% of the cell radius, and the input optical power, ignoring back-reflections, can be estimated to be around 0.5 mW, although there was some uncertainty in photodiode sensitivity due to permutation of the labels attached to the photodiodes. The off-resonance absorption level for cells with their axes parallel to the  $H_0$  field was configured to be close to 15%.

One orientation had the axes of cells A and D parallel to the  $H_0$  field, and the other had the axes of cells C and F parallel to the  $H_0$  field. In the former case, cells C and F had their axes perpendicular to the attached  $H_1$  field axes, while, in the latter case, cells A and D had their axes parallel to their theoretical  $H_1$  axes. “Theoretical” orientation is stipulated since this configuration should yield no signal, so any residual field from nearby cells (which are in a different orientation that *will* produce a signal) may quite plausibly be detected at very low levels. For each of the four cells of interest, we take  $\xi = \eta = \pi/2$ .

For the first orientation, cells A and D had  $\theta = \pi$  and  $\phi = 0$ , while cells C and F had  $\theta = \phi = \pi/2$ . In the second orientation, cells A and D had  $\theta = 0$  and  $\phi = \pi/2$ , and cells C and F had  $\theta = -\pi/2$  and  $\phi = 0$ . Note that this parameterization of coordinates is not unique. Note also that, when  $\phi = 0$ , values for  $\theta$  were parameterized primarily to give particular values for  $\Theta$  to properly describe the  $H_1$  orientation. Three different  $H_1$  amplitudes were used in each case, where our best experimental estimate places these values at 39, 78, and 117 nT<sub>rot</sub>. The resulting magnetic resonance curves are shown in Figures 6.24–6.31.

Figures 6.26 and 6.27 illustrate standard approximately-Lorentzian magnetic resonance lineshapes for cells C and F in the second orientation described, while Figures 6.28 and 6.29 correspond to the other two cells in the opposite orientation. In Figures 6.30 and 6.31, the  $H_1$  axes of cells A and D were parallel to the  $H_0$  field, so both the prior theory and the new model both predict an absence of signal. The existence of a small variation in output current near resonance line center can be attributed to two factors: stray  $H_1$  field from adjacent cells, and a solely-apparent difference due to the fact that the data is not sampled evenly on the horizontal axis in time. The latter factor also explains why the frequency of the interference signal appears to be lower near the center of the resonance: the interpolation to the proper grid spacing necessarily changed the apparent frequency of the interference, which is around 0.3 Hz throughout. It is not clear why there appears to be a decrease in amplitude of interference near resonance on these six plots.

In Figures 6.24 and 6.25, we see there is a small resonance signal when the cell axes,  $H_0$ , and  $H_1$  are all mutually orthogonal. This contradicts prior theory, which indicates there should simply be a flat line like there was in Figures 6.30 and 6.31. The new theory, however, plotted on the same axes, predicts a signal level in reasonable agreement with the data in both shape and magnitude. The theoretical traces in the eight plots in this section involved no fitting. The results in Figures 6.24 and 6.25, in spite of the interference, lend credibility to the new theory.

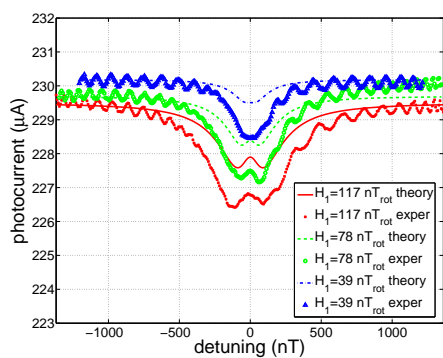


Figure 6.24.  $\sigma$ -pumping data, cell C, AD in field. This is a new effect.

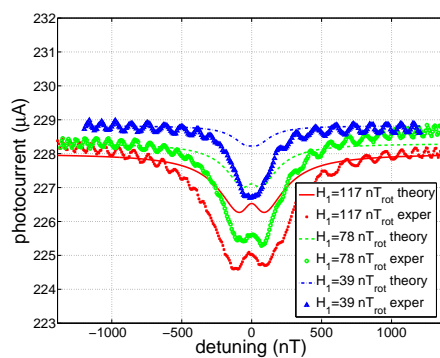


Figure 6.25.  $\sigma$ -pumping data, cell F, AD in field. This is a new effect.

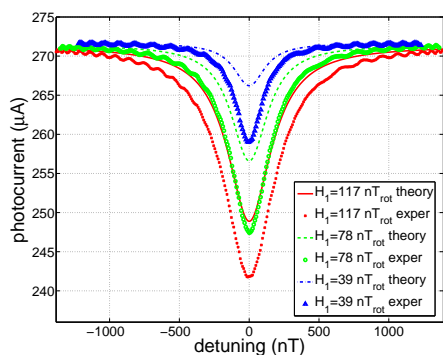


Figure 6.26.  $\sigma$ -pumping data, cell C, CF in field. Standard.

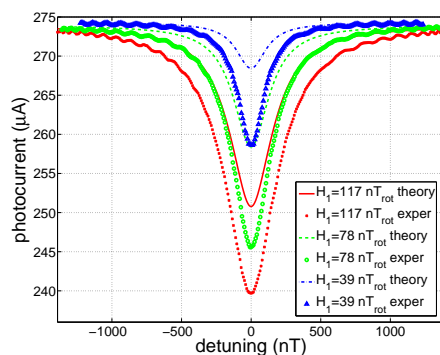


Figure 6.27.  $\sigma$ -pumping data, cell F, CF in field. Standard.

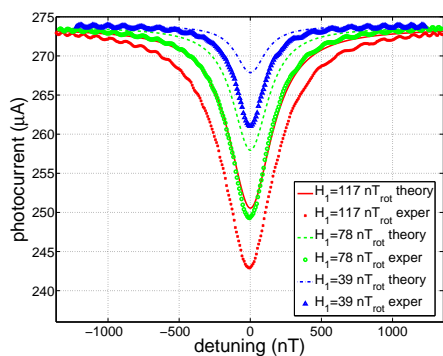


Figure 6.28.  $\sigma$ -pumping data, cell A, AD in field. Standard.

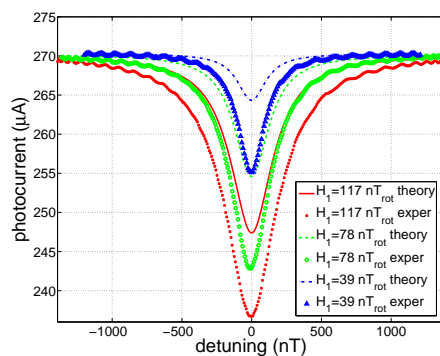


Figure 6.29.  $\sigma$ -pumping data, cell D, AD in field. Standard.

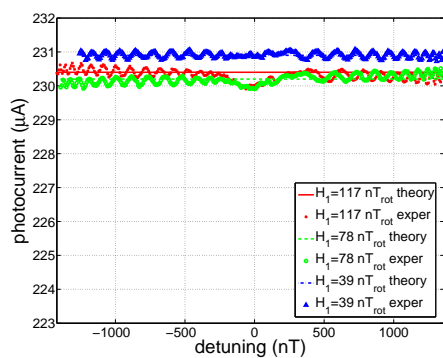


Figure 6.30.  $\sigma$ -pumping data, cell A, CF in field. No signal, except maybe some bleedover from other cells.

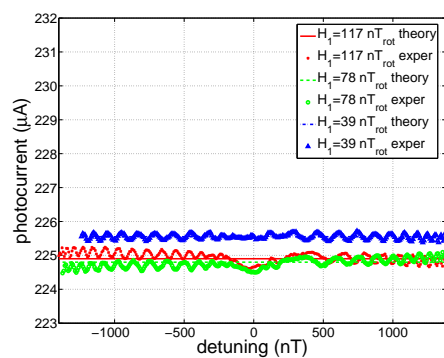


Figure 6.31.  $\sigma$ -pumping data, cell D, CF in field. No signal, except maybe some bleedover from other cells.

## CHAPTER 7

### CONCLUSIONS, APPLICATIONS, AND FUTURE EXTENSIONS

The work presented here is directly applicable to the task of rapidly evaluating new magnetometer designs and to the problem of identifying ranges of parameter values to experimentally optimize within. Several sets of data demonstrate effects that agree well with the new theory, and, in the case presented in Section 6.3, agree with an experimentally-known effect not even qualitatively predicted by prior theory. The ability to parameterize magnetic resonance curves without losing essential features to inaccurate fits is beneficial for straightforward comparisons with this theory and future theory. The means to predict the amount of variation in approximately-isotropic magnetometer designs can save time by allowing the first few design iterations to proceed in simulation. Finally, the work here provides a solid foundation for further extensions into interesting theory and practical effects relevant to the field of optically-pumped magnetometers, overall.

Future extensions to the model may include polarization-dependent and spatially-dependent discharge effects, incorporation of the repopulation pumping and collisional mixing effects that become important in the less-expensive lamp-pumped systems, additional resonance-broadening effects (possibly due to  $H_1$  inhomogeneities), the inclusion of noise sources and other stochastic phenomena, and output equations for the monitoring of scattered light or the polarization of the transmitted light. If stochastic processes are included in the model, the solution would likely need significant modification. The solutions may also be extended to include time-varying parameters and transient effects, which are important primarily because  $\omega$  is a function of time in a locked-loop magnetometer, and  $\omega'$  is also usually varied when using a laser. A thorough study of the harmonics in the transmitted light may also yield valuable information on vector components of the field.

APPENDIX A  
ELECTRIC DIPOLE APPROXIMATION

We will work in the world coordinate system, as shown in Figure 3.1.  $\hat{\mathbf{z}}$  is still the (local axis) direction of light propagation, and we now define  $\vec{\mathbf{R}}$  as the position operator in the world system. Symbols defined in this appendix, such as  $\vec{\mathbf{A}}$ , are local to the appendix.

Reference [48] outlines the electric dipole (E1) approximation, in the context of time-dependent perturbation by classical light. Briefly, in the notation of this work, the electric field of the light is given by:

$$\vec{\mathbf{E}}'(t) = \frac{-1}{c} \frac{\partial}{\partial t} \vec{\mathbf{A}}(t) = \frac{-1}{c} \frac{\partial}{\partial t} \left[ \frac{cE_0}{\omega'} \vec{\mathbf{e}} \sin \left( \frac{\omega' (\vec{\mathbf{R}} \cdot \hat{\mathbf{z}})}{c} - \omega' t \right) \right] = E_0 \vec{\mathbf{e}} \cos \left( \frac{\omega' (\vec{\mathbf{R}} \cdot \hat{\mathbf{z}})}{c} - \omega' t \right)$$

where  $\vec{\mathbf{A}}(t)$  is the vector potential. The perturbation is:

$$\mathcal{H}'_L = \frac{-q}{m_e c} \vec{\mathbf{A}} \cdot \vec{\mathbf{P}} = \frac{-q}{m_e c} \left[ \frac{cE_0}{\omega'} \vec{\mathbf{e}} \sin \left( \frac{\omega' (\vec{\mathbf{R}} \cdot \hat{\mathbf{z}})}{c} - \omega' t \right) \right] \cdot \vec{\mathbf{P}} = \frac{-qE_0}{m_e \omega'} (\vec{\mathbf{e}} \cdot \vec{\mathbf{P}}) \sin \left( \frac{\omega' (\vec{\mathbf{R}} \cdot \hat{\mathbf{z}})}{c} - \omega' t \right)$$

In order to write the dipole approximation in the form used in Reference [34], we have to throw away a 90-degree phase factor in the light, but an overall phase will not be important anyway:

$$\mathcal{H}'_L \rightarrow \frac{iqE_0}{m_e \omega'} (\vec{\mathbf{e}} \cdot \vec{\mathbf{P}}) \cos \left( \frac{\omega' (\vec{\mathbf{R}} \cdot \hat{\mathbf{z}})}{c} - \omega' t \right) \quad (\text{A.1})$$

Moreover, the electric field only enters our treatment via the perturbation, so we can define things to avoid inconsistency.

We define the dipole operator as:

$$\vec{\mathbf{D}} = \frac{-iq}{m_e \omega'} \vec{\mathbf{P}} = q \vec{\mathbf{R}}$$

The final equality is the result of an extension to the brief explanation in reference [48]:

$$[\vec{\mathbf{R}}, \mathcal{H}_0] = \left[ \vec{\mathbf{R}}, \frac{\mathbf{P}^2}{2m_e} \right] = \frac{i\hbar \vec{\mathbf{P}}}{m_e} \quad \Rightarrow \quad \langle m | \vec{\mathbf{P}} | \mu \rangle = \frac{m_e}{i\hbar} \langle m | [\vec{\mathbf{R}}, \mathcal{H}_0] | \mu \rangle = im_e \omega' \langle m | \vec{\mathbf{R}} | \mu \rangle$$

Equation (A.1) can be restated now, and the electric dipole approximation can be applied:

$$\mathcal{H}'_L \rightarrow -\vec{\mathbf{E}}'(t) \cdot \vec{\mathbf{D}} = -qE_0 (\vec{\mathbf{e}} \cdot \vec{\mathbf{R}}) \cos \left( \frac{\omega' (\vec{\mathbf{R}} \cdot \hat{\mathbf{z}})}{c} - \omega' t \right) \approx -qE_0 (\vec{\mathbf{e}} \cdot \vec{\mathbf{R}}) \cos \omega' t$$

This is a result of taking the first term of the Taylor series of  $e^{\pm i\omega' (\vec{\mathbf{R}} \cdot \hat{\mathbf{z}})/c}$ , which is 1.

Now we can redefine the symbols to take the approximation into account:

$$\vec{\mathbf{E}}(t) = E_0 \vec{\mathbf{e}} \cos \omega' t \quad \mathcal{H}_L = -\vec{\mathbf{E}}(t) \cdot \vec{\mathbf{D}}$$

Reference [48], which all of this appendix is based loosely on, gives the region of validity as  $Z \ll 137$ , which is true for helium:  $2 \ll 137$ .  $Z$  is the atomic number. Reference [32] indicates that parity must remain unchanged in magnetic dipole (M1) and electric quadrupole (E2) transitions, however it is clear that  $\Delta L = \pm 1$  is odd for  $D_0$ ,  $D_1$ , and  $D_2$  transitions, so M1 and E2 probabilities do not contribute and E1 is therefore an even better approximation than it already was for the spectral lines of interest in this work.

APPENDIX B  
COORDINATE ROTATIONS

The purpose here is to develop coordinate transformations between the local and world systems defined in Figure 3.1. Symbols defined in this appendix, such as  ${}^0\mathbf{q}$ , are local to the appendix.

$\hat{\mathbf{X}}$ ,  $\hat{\mathbf{Y}}$ , and  $\hat{\mathbf{Z}}$  are the world axes (0). The local axes (1) are identified by small  $\hat{\mathbf{x}}$ ,  $\hat{\mathbf{z}}$ , and  $\hat{\mathbf{y}}$ , as defined previously. To take a vector  $\vec{\mathbf{p}}_1$  in local coordinates to a vector  $\vec{\mathbf{p}}_0$  in world coordinates, we apply a quaternion transform,  $\vec{\mathbf{p}}_0 = ({}^0\mathbf{q})\vec{\mathbf{p}}_1({}^0\mathbf{q}^*)$ . We derive this as a frame rotation, rotating first about the common  $\hat{\mathbf{x}}/\hat{\mathbf{X}}$  axis by  $\phi$ , and then about the local  $\hat{\mathbf{z}}$  axis by  $\theta$ :

$$\begin{aligned}\mathbf{q}_{x,\phi} &\equiv \cos \gamma + \mathbf{i} \sin \gamma & \phi &\equiv 2\gamma & \phi &\text{in } [0, \pi] \\ \mathbf{q}_{z,\theta} &\equiv \cos \beta + \mathbf{k} \sin \beta & \theta &\equiv 2\beta & \theta &\text{in } [-\pi, \pi]\end{aligned}$$

Composing these, we obtain:

$${}^0\mathbf{q} \equiv \mathbf{q}_{x,\phi}\mathbf{q}_{z,\theta} = [\cos \beta \cos \gamma] + [\cos \beta \sin \gamma] \mathbf{i} - [\sin \beta \sin \gamma] \mathbf{j} + [\sin \beta \cos \gamma] \mathbf{k} \quad (\text{B.1})$$

Note that the  $\mathbf{i}$ ,  $\mathbf{j}$ , and  $\mathbf{k}$  are not the unit spatial vectors of [34], but, rather, the standard pure unit quaternions. This usage is local to the appendix. It should be clear from Figure 3.1 that:

$$\hat{\mathbf{x}} \cdot \hat{\mathbf{Z}} = \sin \phi \sin \theta \quad \hat{\mathbf{y}} \cdot \hat{\mathbf{Z}} = \sin \phi \cos \theta \quad \hat{\mathbf{z}} \cdot \hat{\mathbf{Z}} = \cos \phi$$

If it is not clear, however, one could also obtain those relations from Equation (B.1). Note that  $\theta$  is undetermined when  $\phi = 0$ . We can take

$$\phi = \cos^{-1}(\hat{\mathbf{z}} \cdot \hat{\mathbf{Z}}) \quad \theta = \text{atan2}(\hat{\mathbf{x}} \cdot \hat{\mathbf{Z}}, \hat{\mathbf{y}} \cdot \hat{\mathbf{Z}})$$

where the two-argument arctan follows the convention of MATLAB<sup>®</sup> and C, but is opposite of Excel<sup>®</sup> and Mathematica<sup>®</sup>. The sine and cosine of these angles can be obtained in terms of the direction cosines:

$$\cos \phi = \hat{\mathbf{z}} \cdot \hat{\mathbf{Z}} \quad \sin \phi = \sqrt{1 - (\hat{\mathbf{z}} \cdot \hat{\mathbf{Z}})^2} \quad \cos \theta = \frac{\hat{\mathbf{y}} \cdot \hat{\mathbf{Z}}}{\sqrt{1 - (\hat{\mathbf{z}} \cdot \hat{\mathbf{Z}})^2}} \quad \sin \theta = \frac{\hat{\mathbf{x}} \cdot \hat{\mathbf{Z}}}{\sqrt{1 - (\hat{\mathbf{z}} \cdot \hat{\mathbf{Z}})^2}} \quad (\text{B.2})$$

### B.1 3-D Jones Vector

Section 3.1 gives, from [4], an arbitrary state of elliptical polarization in the local coordinate system, constrained to have zero azimuth ( $\theta = 0$ ) and zero absolute phase, as:

$$\begin{bmatrix} \cos \epsilon & -i \sin \epsilon & 0 \end{bmatrix}^T$$

The quaternion transform, using Equation (B.1), yields:

$$\vec{\mathbf{e}} = \begin{pmatrix} 0 \\ 1 \end{pmatrix} \mathbf{q} \begin{bmatrix} \cos \epsilon \\ -i \sin \epsilon \\ 0 \end{bmatrix} \begin{pmatrix} 0 \\ 1 \end{pmatrix} \mathbf{q}^*$$

which evaluates out to give Equation (3.2). Substituting Equation (B.2) into Equation (3.2) yields Equation (3.3).

The quantity  $\langle \mu | \vec{\mathbf{e}}^* \cdot \vec{\mathbf{D}} | m \rangle \langle m | \vec{\mathbf{e}} \cdot \vec{\mathbf{D}} | \mu' \rangle$  is clearly invariant if a unit magnitude complex number is multiplied by  $\vec{\mathbf{e}}$ , so all cross sections are invariant under such a multiplication. This is as it should be, since some uses of these coordinate system transformations will introduce such a phase, and that phase must not affect the cross sections. This also justifies the lack of an explicit absolute phase above.

### B.2 3-D Magnetic Field

The Helmholtz coil direction has been defined in Figure 3.18 to be  $\begin{bmatrix} \sin \eta \cos \xi & \sin \eta \sin \xi & \cos \eta \end{bmatrix}^T$  in the local system, and so it must be rotated.  $H_0$  is already in the world system. The common amplitude factor of  $2H_1 \cos \omega t$  rides along, since rotations are linear transformations. Then, using Equation (B.1):

$$\begin{aligned} \vec{\mathbf{H}} &= 2H_1 \cos \omega t \begin{pmatrix} 0 \\ 1 \end{pmatrix} \mathbf{q} \begin{bmatrix} \sin \eta \cos \xi \\ \sin \eta \sin \xi \\ \cos \eta \end{bmatrix} \begin{pmatrix} 0 \\ 1 \end{pmatrix} \mathbf{q}^* + \begin{bmatrix} 0 \\ 0 \\ H_0 \end{bmatrix} \\ &= 2H_1 \cos \omega t \begin{bmatrix} \sin \eta \cos \Theta \\ \sin \eta \sin \Theta \cos \phi - \cos \eta \sin \phi \\ \sin \eta \sin \Theta \sin \phi + \cos \eta \cos \phi \end{bmatrix} + \begin{bmatrix} 0 \\ 0 \\ H_0 \end{bmatrix} \end{aligned}$$

which can be rewritten as in Equation (3.33).

### B.3 Multiple Cells

If multiple cells are used, and if not all of  $\theta, \phi, \eta, \xi$ , and  $\epsilon$  are the same, it is sometimes desirable to account for the world axes  $\hat{\mathbf{X}}$  and  $\hat{\mathbf{Y}}$ , not just  $\hat{\mathbf{Z}}$ , as we did in the introduction to this appendix. This is, however, not generally possible, since  $\hat{\mathbf{z}}$  is constructed orthogonal to  $\hat{\mathbf{X}}$ :

$$\begin{aligned}\hat{\mathbf{x}} \cdot \hat{\mathbf{X}} &= \cos \theta & \hat{\mathbf{y}} \cdot \hat{\mathbf{X}} &= -\sin \theta & \hat{\mathbf{z}} \cdot \hat{\mathbf{X}} &= 0 \\ \hat{\mathbf{x}} \cdot \hat{\mathbf{Y}} &= \sin \theta \cos \phi & \hat{\mathbf{y}} \cdot \hat{\mathbf{Y}} &= \cos \theta \cos \phi & \hat{\mathbf{z}} \cdot \hat{\mathbf{Y}} &= -\sin \phi\end{aligned}$$

Note that now, even when  $\phi = 0$ ,  $\theta$  can still be determined as long as  $\hat{\mathbf{x}}$  and  $\hat{\mathbf{y}}$  are distinguishable (i.e., for anything but circularly polarized pumping light), provided that  $\hat{\mathbf{X}}$  and  $\hat{\mathbf{Y}}$  have some meaning. As just mentioned, neither  $\hat{\mathbf{X}}$  nor  $\hat{\mathbf{Y}}$  has any intrinsic meaning, but they can nevertheless be defined to retain information about relative arrangements between any two cells. Then, for example,  $\theta = \text{atan2}(-\hat{\mathbf{y}} \cdot \hat{\mathbf{X}}, \hat{\mathbf{x}} \cdot \hat{\mathbf{X}}) = \text{atan2}(\hat{\mathbf{x}} \cdot \hat{\mathbf{Y}}, \hat{\mathbf{y}} \cdot \hat{\mathbf{Y}})$ . However, this formula for  $\theta$  is incorrect if the transformation was not originally constructed to obey the relation  $\hat{\mathbf{z}} \cdot \hat{\mathbf{X}} = 0$ , a relation we will violate below.

Certainly a rotation could have been constructed with an extra degree of freedom, aside from  $\theta$  and  $\phi$ , that would have allowed consistency in “world” systems from one cell to the next, but, since only  $\hat{\mathbf{Z}}$  matters, any consistency in  $\hat{\mathbf{X}}$  and  $\hat{\mathbf{Y}}$  is of no theoretical benefit. At the expense of a more complicated formulation including this extra degree of freedom, there would be a *practical* benefit: the ability to confirm the solution by approaching the problem differently. This will not be pursued here.

Now if two local systems,  $\hat{\mathbf{x}}_1/\hat{\mathbf{y}}_1/\hat{\mathbf{z}}_1$  and  $\hat{\mathbf{x}}_2/\hat{\mathbf{y}}_2/\hat{\mathbf{z}}_2$ , each corresponding to one cell orientation, are known to be related, and if we know the dot products between the axes, then we can express the direction of  $\hat{\mathbf{Z}}$  in the second system using our knowledge of the orientation of the first system. Note that this construction only ensures consistency of  $\hat{\mathbf{Z}}$ ; in other words, if this construction is applied twice to support, e.g., 3 cells, one should not expect any consistent relationship between the  $\hat{\mathbf{X}}$  and  $\hat{\mathbf{Y}}$  resulting from the two iterations. Then we find:

$$\begin{aligned}\hat{\mathbf{x}}_2 \cdot \hat{\mathbf{Z}} &= (\hat{\mathbf{x}}_2 \cdot \hat{\mathbf{x}}_1) \sin \theta_1 \sin \phi_1 + (\hat{\mathbf{x}}_2 \cdot \hat{\mathbf{y}}_1) \cos \theta_1 \sin \phi_1 + (\hat{\mathbf{x}}_2 \cdot \hat{\mathbf{z}}_1) \cos \phi_1 = \sin \phi_2 \sin \theta_2 \\ \hat{\mathbf{y}}_2 \cdot \hat{\mathbf{Z}} &= (\hat{\mathbf{y}}_2 \cdot \hat{\mathbf{x}}_1) \sin \theta_1 \sin \phi_1 + (\hat{\mathbf{y}}_2 \cdot \hat{\mathbf{y}}_1) \cos \theta_1 \sin \phi_1 + (\hat{\mathbf{y}}_2 \cdot \hat{\mathbf{z}}_1) \cos \phi_1 = \sin \phi_2 \cos \theta_2 \\ \hat{\mathbf{z}}_2 \cdot \hat{\mathbf{Z}} &= (\hat{\mathbf{z}}_2 \cdot \hat{\mathbf{x}}_1) \sin \theta_1 \sin \phi_1 + (\hat{\mathbf{z}}_2 \cdot \hat{\mathbf{y}}_1) \cos \theta_1 \sin \phi_1 + (\hat{\mathbf{z}}_2 \cdot \hat{\mathbf{z}}_1) \cos \phi_1 = \cos \phi_2\end{aligned}$$

From there, we can easily solve for  $\phi_2$  and  $\theta_2$  in the same way we did previously.

## APPENDIX C

### REDUCED CROSS SECTIONS WITH ARBITRARY POLARIZATION

In order to be able to fit everything on the page, we define three temporary factors that are local to this appendix:

$$\begin{aligned}
 f_1 &= [\cos \theta + i \sin \theta \cos \phi] \cos \epsilon + [i \sin \theta + \cos \theta \cos \phi] \sin \epsilon \\
 f_2 &= \sqrt{2} [\sin \theta \sin \phi] \cos \epsilon - i \sqrt{2} [\cos \theta \sin \phi] \sin \epsilon \\
 f_3 &= [\cos \theta - i \sin \theta \cos \phi] \cos \epsilon + [i \sin \theta - \cos \theta \cos \phi] \sin \epsilon
 \end{aligned}$$

We first multiply the polarization vector from Equation (3.2) with Equation (3.20):

$$\begin{aligned}
 D_0 : \quad \langle m | \vec{e} \cdot \vec{D} | \mu \rangle &= \frac{D_0}{\sqrt{6}} \left[ \begin{array}{c|ccc} & (\mu = 1) & (\mu = 0) & (\mu = -1) \\ \hline (m = 0) & f_1 & -f_2 & -f_3 \end{array} \right] \\
 D_1 : \quad \langle m | \vec{e} \cdot \vec{D} | \mu \rangle &= \frac{D_0}{2} \left[ \begin{array}{c|ccc} & (\mu = 1) & (\mu = 0) & (\mu = -1) \\ \hline (m = 1) & f_2 & f_3 & 0 \\ (m = 0) & f_1 & 0 & f_3 \\ (m = -1) & 0 & f_1 & -f_2 \end{array} \right] \\
 D_2 : \quad \langle m | \vec{e} \cdot \vec{D} | \mu \rangle &= \frac{D_0}{2\sqrt{3}} \left[ \begin{array}{c|ccc} & (\mu = 1) & (\mu = 0) & (\mu = -1) \\ \hline (m = 2) & -f_3 \sqrt{6} & 0 & 0 \\ (m = 1) & f_2 \sqrt{3} & -f_3 \sqrt{3} & 0 \\ (m = 0) & f_1 & 2f_2 & -f_3 \\ (m = -1) & 0 & f_1 \sqrt{3} & f_2 \sqrt{3} \\ (m = -2) & 0 & 0 & f_1 \sqrt{6} \end{array} \right]
 \end{aligned}$$

Then we multiply the matrices with themselves to obtain:

$$\langle \mu | \vec{e}^* \cdot \vec{D} | m \rangle \langle m | \vec{e} \cdot \vec{D} | \mu' \rangle =$$

$$D_0 : \frac{D_0^2}{6} \begin{array}{c|ccc} & (\mu' = 1) & (\mu' = 0) & (\mu' = -1) \\ \hline (\mu = 1) & f_1 f_1^* & -f_2 f_1^* & -f_3 f_1^* \\ (\mu = 0) & -f_1 f_2^* & f_2 f_2^* & f_3 f_2^* \\ (\mu = -1) & -f_1 f_3^* & f_2 f_3^* & f_3 f_3^* \end{array}$$

$$D_1 : \frac{D_0^2}{4} \begin{array}{c|ccc} & (\mu' = 1) & (\mu' = 0) & (\mu' = -1) \\ \hline (\mu = 1) & f_1 f_1^* + f_2 f_2^* & f_3 f_2^* & f_3 f_1^* \\ (\mu = 0) & f_2 f_3^* & f_3 f_3^* + f_1 f_1^* & -f_2 f_1^* \\ (\mu = -1) & f_1 f_3^* & -f_1 f_2^* & f_2 f_2^* + f_3 f_3^* \end{array}$$

$$D_2 : \frac{D_0^2}{12} \begin{array}{c|ccc} & (\mu' = 1) & (\mu' = 0) & (\mu' = -1) \\ \hline (\mu = 1) & f_1 f_1^* + 3f_2 f_2^* + 6f_3 f_3^* & 2f_2 f_1^* - 3f_3 f_2^* & -f_3 f_1^* \\ (\mu = 0) & 2f_1 f_2^* - 3f_2 f_3^* & 3f_1 f_1^* + 4f_2 f_2^* + 3f_3 f_3^* & 3f_2 f_1^* - 2f_3 f_2^* \\ (\mu = -1) & -f_1 f_3^* & 3f_1 f_2^* - 2f_2 f_3^* & 6f_1 f_1^* + 3f_2 f_2^* + f_3 f_3^* \end{array}$$

Substituting into the equations in Section 3.7.2 and using the representations of Equation (3.21), we find the traces for lines D<sub>0</sub>, D<sub>1</sub>, and D<sub>2</sub>, respectively, where these are arrays, not matrices:

$$Q_I = \frac{\hbar D_0^2}{6} (f_1 f_1^* + f_2 f_2^* + f_3 f_3^*) \begin{bmatrix} 1 & 3 & 5 \end{bmatrix} \quad Q_0 = \frac{\hbar D_0^2}{12\sqrt{6}} (f_1 f_1^* - 2f_2 f_2^* + f_3 f_3^*) \begin{bmatrix} 2 & -3 & 1 \end{bmatrix}$$

$$Q_z = \frac{\hbar D_0^2}{12} (f_1 f_1^* - f_3 f_3^*) \begin{bmatrix} 2 & 3 & -5 \end{bmatrix} \quad Q_1 = \frac{\hbar D_0^2}{12\sqrt{2}} (f_2 f_3^* + f_1 f_2^*) \begin{bmatrix} 2 & -3 & 1 \end{bmatrix}$$

$$Q_+ = \frac{\hbar D_0^2 \sqrt{2}}{12} (f_2 f_3^* - f_1 f_2^*) \begin{bmatrix} 2 & 3 & -5 \end{bmatrix} \quad Q_2 = \frac{\hbar D_0^2}{12} (-f_1 f_3^*) \begin{bmatrix} 2 & -3 & 1 \end{bmatrix}$$

It is apparent that:

$$f_1 f_1^* + f_2 f_2^* + f_3 f_3^* = 2$$

$$f_1 f_1^* - 2f_2 f_2^* + f_3 f_3^* = \frac{1 + 3 \cos 2\phi + 3(1 - \cos 2\phi) \cos 2\epsilon \cos 2\theta}{2}$$

$$= 3(\hat{\mathbf{z}} \cdot \hat{\mathbf{Z}})^2 - 1 - 3\left[(\hat{\mathbf{x}} \cdot \hat{\mathbf{Z}})^2 - (\hat{\mathbf{y}} \cdot \hat{\mathbf{Z}})^2\right] \cos 2\epsilon$$

$$f_1 f_1^* - f_3 f_3^* = 2 \cos \phi \sin 2\epsilon = 2 \sin 2\epsilon (\hat{\mathbf{z}} \cdot \hat{\mathbf{Z}})$$

$$-f_1 f_3^* = \sin^2 \epsilon (\cos \theta \cos \phi + i \sin \theta)^2 - \cos^2 \epsilon (\cos \theta + i \cos \phi \sin \theta)^2$$

$$= \frac{\left[(\hat{\mathbf{y}} \cdot \hat{\mathbf{Z}}) + i(\hat{\mathbf{x}} \cdot \hat{\mathbf{Z}})(\hat{\mathbf{z}} \cdot \hat{\mathbf{Z}})\right]^2 \cos^2 \epsilon + \left[(\hat{\mathbf{x}} \cdot \hat{\mathbf{Z}}) - i(\hat{\mathbf{y}} \cdot \hat{\mathbf{Z}})(\hat{\mathbf{z}} \cdot \hat{\mathbf{Z}})\right]^2 \sin^2 \epsilon}{(\hat{\mathbf{z}} \cdot \hat{\mathbf{Z}})^2 - 1}$$

Similarly,

$$\begin{aligned}
 f_2 f_3^* + f_1 f_2^* &= \sqrt{2} \cos 2\epsilon \sin 2\theta \sin \phi - \frac{i}{\sqrt{2}} (\cos 2\epsilon \cos 2\theta - 1) \sin 2\phi \\
 &= \sqrt{2} \frac{i(\hat{\mathbf{z}} \cdot \hat{\mathbf{Z}}) [1 - (\hat{\mathbf{z}} \cdot \hat{\mathbf{Z}})^2]}{\sqrt{1 - (\hat{\mathbf{z}} \cdot \hat{\mathbf{Z}})^2}} \\
 &\quad + \sqrt{2} \frac{\cos 2\epsilon \left[ i(\hat{\mathbf{x}} \cdot \hat{\mathbf{Z}})^2 (\hat{\mathbf{z}} \cdot \hat{\mathbf{Z}}) - i(\hat{\mathbf{y}} \cdot \hat{\mathbf{Z}})^2 (\hat{\mathbf{z}} \cdot \hat{\mathbf{Z}}) + 2(\hat{\mathbf{x}} \cdot \hat{\mathbf{Z}})(\hat{\mathbf{y}} \cdot \hat{\mathbf{Z}}) \right]}{\sqrt{1 - (\hat{\mathbf{z}} \cdot \hat{\mathbf{Z}})^2}} \\
 f_2 f_3^* - f_1 f_2^* &= -i \sqrt{2} \sin 2\epsilon \sin \phi = -i \sqrt{2} \sin 2\epsilon \sqrt{1 - (\hat{\mathbf{z}} \cdot \hat{\mathbf{Z}})^2}
 \end{aligned}$$

This yields the results in Section 3.7.3, but also provides an alternative method of evaluation for the situations in which certain limits are difficult to evaluate, notably when  $\hat{\mathbf{z}} \cdot \hat{\mathbf{Z}} = 1$ . In that situation, we find that  $\mathcal{Q}_1 = 0$  and  $\mathcal{Q}_2 = -\frac{\hbar D_0^2}{12} e^{2i\theta} \cos 2\epsilon$ , but  $\theta$  is indeterminate in this situation, so we can arbitrarily take  $\mathcal{Q}_2 = \frac{\hbar D_0^2}{12} \cos 2\epsilon$ , as described in Section 4.3.

APPENDIX D  
COMMUTATOR LIST

D.1 Commutators

$$\left[ \left[ \begin{array}{c} J_z \\ J_+ \\ J_- \\ T_2^{(2)} \\ T_1^{(2)} \\ T_0^{(2)} \\ T_{-1}^{(2)} \\ T_{-2}^{(2)} \end{array} \right], \left[ \begin{array}{c} J_z \\ J_+ \\ J_- \\ T_2^{(2)} \\ T_1^{(2)} \\ T_0^{(2)} \\ T_{-1}^{(2)} \\ T_{-2}^{(2)} \end{array} \right]^T \right] = \hbar \left[ \begin{array}{cccccccc} 0 & J_+ & -J_- & 2T_2^{(2)} & T_1^{(2)} & 0 & -T_{-1}^{(2)} & -2T_{-2}^{(2)} \\ -J_+ & 0 & 2J_z & 0 & 2T_2^{(2)} & \sqrt{6}T_1^{(2)} & \sqrt{6}T_0^{(2)} & 2T_{-1}^{(2)} \\ J_- & -2J_z & 0 & 2T_1^{(2)} & \sqrt{6}T_0^{(2)} & \sqrt{6}T_{-1}^{(2)} & 2T_{-2}^{(2)} & 0 \\ -2T_2^{(2)} & 0 & -2T_1^{(2)} & 0 & 0 & 0 & \frac{-1}{2}J_+ & J_z \\ -T_1^{(2)} & -2T_2^{(2)} & -\sqrt{6}T_0^{(2)} & 0 & 0 & \sqrt{\frac{3}{8}}J_+ & \frac{-1}{2}J_z & \frac{1}{2}J_- \\ 0 & -\sqrt{6}T_1^{(2)} & -\sqrt{6}T_{-1}^{(2)} & 0 & -\sqrt{\frac{3}{8}}J_+ & 0 & -\sqrt{\frac{3}{8}}J_- & 0 \\ T_{-1}^{(2)} & -\sqrt{6}T_0^{(2)} & -2T_{-2}^{(2)} & \frac{1}{2}J_+ & \frac{1}{2}J_z & \sqrt{\frac{3}{8}}J_- & 0 & 0 \\ 2T_{-2}^{(2)} & -2T_{-1}^{(2)} & 0 & -J_z & \frac{-1}{2}J_- & 0 & 0 & 0 \end{array} \right]$$

Note that “transpose” here is just a device to make a row vector of operators; the operators *themselves* inside the second argument are not transposed by this notation.

D.2 Anticommutators

$$\left[ \left[ \begin{array}{c} J_z \\ J_+ \\ J_- \\ T_2^{(2)} \\ T_1^{(2)} \\ T_0^{(2)} \\ T_{-1}^{(2)} \\ T_{-2}^{(2)} \end{array} \right], \left[ \begin{array}{c} J_z \\ J_+ \\ J_- \\ T_2^{(2)} \\ T_1^{(2)} \\ T_0^{(2)} \\ T_{-1}^{(2)} \\ T_{-2}^{(2)} \end{array} \right]^T \right] = \hbar \left[ \begin{array}{cccccccc} * & -2T_1^{(2)} & 2T_{-1}^{(2)} & 0 & \frac{-1}{2}J_+ & \sqrt{\frac{2}{3}}J_z & \frac{1}{2}J_- & 0 \\ -2T_1^{(2)} & 4T_2^{(2)} & * & 0 & 0 & \frac{-1}{\sqrt{6}}J_+ & J_z & J_- \\ 2T_{-1}^{(2)} & * & 4T_{-2}^{(2)} & J_+ & -J_z & \frac{-1}{\sqrt{6}}J_- & 0 & 0 \\ 0 & 0 & J_+ & 0 & 0 & \sqrt{\frac{2}{3}}T_2^{(2)} & T_1^{(2)} & * \\ \frac{-1}{2}J_+ & 0 & -J_z & 0 & -T_2^{(2)} & \frac{-1}{\sqrt{6}}T_1^{(2)} & * & T_{-1}^{(2)} \\ \sqrt{\frac{2}{3}}J_z & \frac{-1}{\sqrt{6}}J_+ & \frac{-1}{\sqrt{6}}J_- & \sqrt{\frac{2}{3}}T_2^{(2)} & \frac{-1}{\sqrt{6}}T_1^{(2)} & * & \frac{-1}{\sqrt{6}}T_{-1}^{(2)} & \sqrt{\frac{2}{3}}T_{-2}^{(2)} \\ \frac{1}{2}J_- & J_z & 0 & T_1^{(2)} & * & \frac{-1}{\sqrt{6}}T_{-1}^{(2)} & -T_{-2}^{(2)} & 0 \\ 0 & J_- & 0 & * & T_{-1}^{(2)} & \sqrt{\frac{2}{3}}T_{-2}^{(2)} & 0 & 0 \end{array} \right]$$

$$\hbar^{-1} \{J_z, J_z\} = \frac{4\hbar}{3} + \sqrt{\frac{8}{3}}T_0^{(2)} \quad \hbar^{-1} \{J_{\pm}, J_{\mp}\} = \frac{8\hbar}{3} - \sqrt{\frac{8}{3}}T_0^{(2)} \quad \hbar^{-1} \{T_0^{(2)}, T_0^{(2)}\} = \frac{2\hbar}{3} - \sqrt{\frac{2}{3}}T_0^{(2)}$$

$$\hbar^{-1} \{T_{\pm 1}^{(2)}, T_{\mp 1}^{(2)}\} = \frac{-2\hbar}{3} + \frac{1}{\sqrt{6}}T_0^{(2)} \quad \hbar^{-1} \{T_{\pm 2}^{(2)}, T_{\mp 2}^{(2)}\} = \frac{2\hbar}{3} + \sqrt{\frac{2}{3}}T_0^{(2)}$$

## APPENDIX E

### FURTHER $\pi$ -PERPENDICULAR CALCULATIONS

Continuing from Section 4.3, we find that the next level up is governed by a similar system of equations:

$$2i\omega \begin{bmatrix} u_{2,2} \\ u_{1,2} \\ u_{0,2} \\ u_{-1,2} \\ u_{-2,2} \end{bmatrix} = \Phi Q_P^{(22)} \begin{bmatrix} \sqrt{3/2}u_{0,4} \\ {}^3/2u_{-1,4} \\ \sqrt{3/2}(u_{2,0} + u_{-2,4}) \\ {}^3/2u_{1,0} \\ \sqrt{3/2}u_{0,0} + 1 \end{bmatrix} + \begin{bmatrix} 2k_3 - \tau_1^{-1} & 2k_4 & 0 & 0 & 0 \\ 2k_4 & k_3 - \tau_2^{-1} & \sqrt{6}k_4 & 0 & 0 \\ 0 & \sqrt{6}k_4 & -\tau_0^{-1} & \sqrt{6}k_4 & 0 \\ 0 & 0 & \sqrt{6}k_4 & -k_3 - \tau_2^{-1} & 2k_4 \\ 0 & 0 & 0 & 2k_4 & -2k_3 - \tau_1^{-1} \end{bmatrix} \begin{bmatrix} u_{2,2} \\ u_{1,2} \\ u_{0,2} \\ u_{-1,2} \\ u_{-2,2} \end{bmatrix}$$

$$-2i\omega \begin{bmatrix} u_{2,-2} \\ u_{1,-2} \\ u_{0,-2} \\ u_{-1,-2} \\ u_{-2,-2} \end{bmatrix} = \Phi Q_P^{(22)} \begin{bmatrix} \sqrt{3/2}u_{0,0} + 1 \\ {}^3/2u_{-1,0} \\ \sqrt{3/2}(u_{2,-4} + u_{-2,0}) \\ {}^3/2u_{1,-4} \\ \sqrt{3/2}u_{0,-4} \end{bmatrix} + \begin{bmatrix} 2k_3 - \tau_1^{-1} & 2k_4 & 0 & 0 & 0 \\ 2k_4 & k_3 - \tau_2^{-1} & \sqrt{6}k_4 & 0 & 0 \\ 0 & \sqrt{6}k_4 & -\tau_0^{-1} & \sqrt{6}k_4 & 0 \\ 0 & 0 & \sqrt{6}k_4 & -k_3 - \tau_2^{-1} & 2k_4 \\ 0 & 0 & 0 & 2k_4 & -2k_3 - \tau_1^{-1} \end{bmatrix} \begin{bmatrix} u_{2,-2} \\ u_{1,-2} \\ u_{0,-2} \\ u_{-1,-2} \\ u_{-2,-2} \end{bmatrix}$$

Let

$$\alpha_2 \equiv 2i\omega - k_3 + \tau_2^{-1} - \frac{4k_4^2}{\tau_1^{-1} - 2k_3 + 2i\omega} \quad \alpha_3 \equiv -2i\omega - k_3 + \tau_2^{-1} - \frac{4k_4^2}{\tau_1^{-1} - 2k_3 - 2i\omega}$$

$$2i\omega \begin{bmatrix} 0 \\ u_{0,2} \\ 0 \end{bmatrix} = \Phi Q_P^{(22)} \begin{bmatrix} {}^3/2u_{-1,4} + \frac{2k_4}{\tau_1^{-1} - 2k_3 + 2i\omega} \sqrt{3/2}u_{0,4} \\ \sqrt{3/2}(u_{2,0} + u_{-2,4}) \\ {}^3/2u_{1,0} + \frac{2k_4}{\tau_1^{-1} + 2k_3 + 2i\omega} (\sqrt{3/2}u_{0,0} + 1) \end{bmatrix} + \begin{bmatrix} -\alpha_2 & \sqrt{6}k_4 & 0 \\ \sqrt{6}k_4 & -\tau_0^{-1} & \sqrt{6}k_4 \\ 0 & \sqrt{6}k_4 & -\alpha_3^* \end{bmatrix} \begin{bmatrix} u_{1,2} \\ u_{0,2} \\ u_{-1,2} \end{bmatrix}$$

$$-2i\omega \begin{bmatrix} 0 \\ u_{0,-2} \\ 0 \end{bmatrix} = \Phi Q_P^{(22)} \begin{bmatrix} 3/2u_{-1,0} + \frac{2k_4}{\tau_1^{-1}-2k_3-2i\omega} (\sqrt{3/2}u_{0,0} + 1) \\ \sqrt{3/2}(u_{2,-4} + u_{-2,0}) \\ 3/2u_{1,-4} + \frac{2k_4}{\tau_1^{-1}+2k_3-2i\omega} \sqrt{3/2}u_{0,-4} \end{bmatrix} + \begin{bmatrix} -\alpha_3 & \sqrt{6}k_4 & 0 \\ \sqrt{6}k_4 & -\tau_0^{-1} & \sqrt{6}k_4 \\ 0 & \sqrt{6}k_4 & -\alpha_2^* \end{bmatrix} \begin{bmatrix} u_{1,-2} \\ u_{0,-2} \\ u_{-1,-2} \end{bmatrix}$$

This procedure can be completed, allowing the  $u_{\xi,0}$  terms of Section 4.3 to be expressed in terms of the  $u_{\xi,\pm 4}$  coefficients, by eliminating the  $u_{\xi,\pm 2}$  coefficients through the equations in this section. Each set of such equations relates fifteen coefficients, five each of orders  $2n$ , and  $2n \pm 2$ . While this procedure appears to introduce a solution in terms of quantities at both  $\pm 2n$ , it should be noted that careful treatment allows one to use Hermitian and/or skew-Hermitian properties to keep the number of unknowns the same. Each additional order likely introduces a small perturbation in those components observable through Equation (3.42), but each additional order must necessarily become smaller. Indeed, numerical tests with the model of Chapter 5 seem to indicate that, at most, only the  $n = -2, 0, 2$  coefficients need be treated in order to account for light level variations at DC ( $0\omega$ ) to within rounding error. This appendix serves as the beginning to an analytic treatment, and may be completed in a future extension.

## REFERENCES

- [1] Milton Abramowitz and Irene A. Stegun. *Handbook of Mathematical Functions with Formulas, Graphs, and Mathematical Tables*. Dover, New York, ninth Dover printing, tenth GPO printing edition, 1964.
- [2] Mario H. Acuña. Space-Based Magnetometers. *Rev. Sci. Instrum.*, 73(11):3717–3736, Nov 2002.
- [3] C. Amsler et al. Clebsch-Gordan Coefficients, Spherical Harmonics, and  $d$  Functions. [Online] 1–5, Physics Letters B, Sep 2008. Also available as <http://pdg.lbl.gov/2008/reviews/clebrpp.pdf>.
- [4] R. M. A. Azzam and N. M. Bashara. *Ellipsometry and Polarized Light*. Elsevier North-Holland, Amsterdam, 1977.
- [5] W. E. Bell and A. L. Bloom. Optically Driven Spin Precession. *Phys. Rev. Lett.*, 6(6):280–281, Mar 1961.
- [6] F. Bitter. The Optical Detection of Radiofrequency Resonance. *Phys. Rev.*, 76(6):833–835, Sep 1949.
- [7] F. Bloch. Nuclear Induction. *Phys. Rev.*, 70(7–8):460–474, Oct 1946.
- [8] F. Bloch and A. Siegert. Magnetic Resonance for Nonrotating Fields. *Phys. Rev.*, 57(6):522–527, Mar 1940.
- [9] G. Breit and E. Teller. Metastability of Hydrogen and Helium Levels. *Astrophysical Journal*, 91:215–238, Mar 1940.
- [10] Jean Brossel and Francis Bitter. A New “Double Resonance” Method for Investigating Atomic Energy Levels. Application to  $HgP13$ . *Phys. Rev.*, 86(3):308–316, May 1952.
- [11] D. Budker and M. Romalis. Optical Magnetometry. *Nature Physics*, 3:227–234, Apr 2007.
- [12] B. Chéron, H. Gilles, J. Hamel, O. Moreau, and E. Noël. A New Optical Pumping Scheme Using a Frequency Modulated Semi-conductor Laser for  $4He$  Magnetometers. *Optics Communications*, 115(1–2):71–74, 1995.
- [13] F. D. Colegrove and P. A. Franken. Optical Pumping of Helium in the  $^3S_1$  Metastable State. *Phys. Rev.*, 119(2):680–690, Jul 1960.
- [14] G. W. F. Drake, G. A. Victor, and A. Dalgarno. Two-Photon Decay of the Singlet and Triplet Metastable States of Helium-like Ions. *Phys. Rev.*, 180(1):25–32, Apr 1969.
- [15] Robert C. Forrey. Compact Representation of Helium Wave Functions in Perimetric and Hyperspherical Coordinates. *Phys. Rev. A*, 69(2):022504, Feb 2004.

- [16] P. A. Franken and F. D. Colegrove. Alignment of Metastable Helium Atoms by Unpolarized Resonance Radiation. *Phys. Rev. Lett.*, 1(9):316–318, Nov 1958.
- [17] A. C. Fraser-Smith. The Magnetic Field Gradiometer. Final Technical Report E723-1, Stanford Electronics Laboratories, Feb 1983.
- [18] N. L. Freire and S. C. Douglas. Adaptive Cancellation of Geomagnetic Background Noise Using a Sign-Error Normalized LMS Algorithm. In *Acoustics, Speech, and Signal Processing, 1993. ICASSP-93., 1993 IEEE International Conference on*, volume 3, pages 523–526, Apr 1993.
- [19] H. Gilles, J. Hamel, and B. Chéron. Laser pumped  $^4\text{He}$  magnetometer. *Rev. of Sci. Instr.*, 72:2253–2260, May 2001.
- [20] C. Guttin, J. M. Leger, and F. Stoeckel. An Isotropic Earth Field Scalar Magnetometer Using Optically Pumped Helium 4. *J. Phys. IV France*, 4(C4):655–659, 1994.
- [21] W. Happer. Optical Pumping. *Rev. Mod. Phys.*, 44(2):169–249, Apr 1972.
- [22] W. Happer and B. S. Mathur. Effective Operator Formalism in Optical Pumping. *Phys. Rev.*, 163(1):12–25, Nov 1967.
- [23] J. P. Heppner. The World Magnetic Survey. *Space Science Reviews*, 2(3):315–354, Sep 1963.
- [24] J. C. Hill, L. L. Hatfield, N. D. Stockwell, and G. K. Walters. Direct Demonstration of Spin-Angular-Momentum Conservation in the Reaction  $\text{He}(2^3\text{S}_1) + \text{He}(2^3\text{S}_1) \rightarrow \text{He}(1^1\text{S}_0) + \text{He}^+ + e^-$ . *Phys. Rev. A*, 5(1):189–195, Jan 1972.
- [25] V. Hughes, G. Tucker, E. Rhoderick, and G. Weinreich. The Magnetic Moment of the Helium Atom in the Metastable Triplet State. *Phys. Rev.*, 91(4):828–841, Aug 1953.
- [26] Alfred Kastler. Optical Methods of Atomic Orientation and of Magnetic Resonance. *J. Opt. Soc. Am.*, 47(6):460–465, Jun 1957.
- [27] Alfred Kastler. Displacement of Energy Levels of Atoms by Light. *J. Opt. Soc. Am.*, 53(8):902–906, Aug 1963.
- [28] A. R. Keyser, J. A. Rice, and L. D. Schearer. A Metastable Helium Magnetometer for Observing Small Geomagnetic Fluctuations. *J. Geophys. Res.*, 66:4163–4169, Dec 1961.
- [29] A. Kponou, V. W. Hughes, C. E. Johnson, S. A. Lewis, and F. M. J. Pichanick. Experiments on the  $2^3P$  state of Helium. III. Measurement of the  $2^3P_0 - 2^3P_1$  Fine-structure Interval. *Phys. Rev. A*, 24(1):264–278, Jul 1981.
- [30] D. A. Landman. Lifetimes and Alignment Depolarization Cross Sections of the  $(3p^5 4p) ^3D_3$  and  $^1D'_2$  Levels in Argon and the  $(1s2p) ^3P$  Term in Helium. *Phys. Rev.*, 173(1):33–39, Sep 1968.
- [31] J. Lenz and S. Edelstein. Magnetic Sensors and Their Applications. *IEEE Sensors Journal*, 6(3):631–649, Jun 2006.

- [32] W. C. Martin and W. L. Wiese. Atomic, Molecular, and Optical Physics Handbook (version 1.01). [online], National Institute of Standards and Technology, May 2007.
- [33] M. V. McCusker, L. L. Hatfield, and G. K. Walters. Cumulative Ionization in Optically Pumped Helium Discharges: A Source of Polarized Electrons. *Phys. Rev. A*, 5(1):177–189, Jan 1972.
- [34] Douglas D. McGregor. High-Sensitivity Helium Resonance Magnetometers. *Rev. Sci. Instrum.*, 58(6):1067–1076, Jun 1987.
- [35] Douglas D. McGregor. private communication, Sep 2006.
- [36] Douglas D. McGregor. private communication, May 2009.
- [37] B. L. Moiseiwitsch and S. J. Smith. Electron Impact Excitation of Atoms. *Rev. Mod. Phys.*, 40(2):238–353, Apr 1968.
- [38] A. Papoulis and S. U. Pillai. *Probability, Random Variables and Stochastic Processes*. McGraw-Hill, New York, 4th ed. edition, 2002.
- [39] C. L. Pekeris.  $1^1S$  and  $2^3S$  States of Helium. *Phys. Rev.*, 115(5):1216–1221, Sep 1959.
- [40] C. L. Pekeris.  $1^1S$ ,  $2^1S$ , and  $2^3S$  States of  $H^-$  and of He. *Phys. Rev.*, 126(4):1470–1476, May 1962.
- [41] A. V. Phelps and J. P. Molnar. Lifetimes of Metastable States of Noble Gases. *Phys. Rev.*, 89(6):1202–1208, Mar 1953.
- [42] F. M. J. Pichanick, R. D. Swift, C. E. Johnson, and V. W. Hughes. Experiments on the  $2^3P$  State of Helium. I. A Measurement of the  $2^3P_1 - 2^3P_2$  Fine Structure. *Phys. Rev.*, 169(1):55–78, May 1968.
- [43] M. K. Plante, D. L. MacFarlane, D. D. McGregor, R. E. Slocum, W. M. Sampson, and A. W. Brown. A Generalized Theory of Double-Resonance Optical Pumping of Helium-4. To appear in *Phys. Rev. A*.
- [44] Polatomic, Inc. <http://polatomic.com/>. (accessed 2008).
- [45] W. H. Press, S. A. Teukolsky, W. T. Vetterling, and B. P. Flannery. *Numerical Recipes in C*. Cambridge University Press, New York, second, corrected edition, 1999.
- [46] I. I. Rabi, N. F. Ramsey, and J. Schwinger. Use of Rotating Coordinates in Magnetic Resonance Problems. *Rev. Mod. Phys.*, 26(2):167–171, Apr 1954.
- [47] Y. Ralchenko, A. E. Kramida, J. Reader, and NIST ASD Team. NIST Atomic Spectra Database (version 3.1.5). [online], National Institute of Standards and Technology, 2008.
- [48] J. J. Sakurai. *Modern Quantum Mechanics*. Ed. Tuan, S. F. Addison-Wesley, Reading, MA, revised edition, 1994.
- [49] L. Schearer, M. Leduc, D. Vivien, A. M. Lejus, and J. Thery. LNA: A New CW Nd Laser Tunable Around 1.05 and 1.08  $\mu\text{m}$ . *Quantum Electronics, IEEE Journal of*, 22(5):713–717, May 1986.

- [50] L. D. Schearer. Energy Shifts of the Magnetic Sublevels of  $S^{13}$  Helium Caused by Optical Pumping. *Phys. Rev.*, 127(2):512–517, Jul 1962.
- [51] L. D. Schearer. Collision-Induced Mixing in the  $2^3P$  Levels of Helium. *Phys. Rev.*, 160(1):76–80, Aug 1967.
- [52] L. D. Schearer. Depolarization of Light Scattered by Aligned  $2^3S$  and  $2^3P$  Helium Atoms at Resonance. *Phys. Rev.*, 166(1):30–33, Feb 1968.
- [53] L. D. Schearer and F. D. Sinclair. Gyromagnetic Ratio of Helium  $2^3S_1$  Atoms By Optical Pumping: Level Shifts. *Phys. Rev.*, 175(1):36–39, Nov 1968.
- [54] L. D. Schearer and P. Tin. Tunable Lasers at 1080 nm for Helium Optical Pumping. *Journal of Applied Physics*, 68:943–949, Aug 1990.
- [55] B. Schiff and C. L. Pekeris.  $f$  Values for Transitions between the  $1^1S$ ,  $2^1S$ , and  $2^3S$ , and the  $2^1P$ ,  $2^3P$ ,  $3^1P$ , and  $3^3P$  States in Helium. *Phys. Rev.*, 134(3A):A638–A640, May 1964.
- [56] V. Y. Shifrin, P. G. Park, C. G. Kim, V. N. Khorev, and C. H. Choi. Experimental Determination of the Gyromagnetic Ratio of the Helium-4 Atom in Terms of That of the Helium-3 Nucleus. *Instrumentation and Measurement, IEEE Transactions on*, 46(2):97–100, Apr 1997.
- [57] T. L. Skillman and P. L. Bender. Measurement of the Earth's Magnetic Field with a Rubidium Vapor Magnetometer. *J. Geophys. Res.*, 63(3):513–515, Sep 1958.
- [58] C. P. Slichter. *Principles of Magnetic Resonance*. Springer, Berlin, third enl. and updated edition, 1996.
- [59] R. Slocum and B. Marton. A Nuclear Free Precession Magnetometer using Optically Polarized  $He^3$  Gas. *Magnetics, IEEE Transactions on*, 10(3):528–531, Sep 1974.
- [60] R. E. Slocum, G. Kuhlman, L. Ryan, and D. King. Polatomic Advances in Magnetic Detection. In H. W. Anderson and T. W. Donaldson V, editors, *OCEANS '02 MTS/IEEE*, Biloxi, MS, 2002. IEEE Press.
- [61] R. E. Slocum and E. J. Smith. Advances in Optically Pumped Helium Magnetometers for Space and Earth Science. *Contributions to Geophysics and Geodesy*, 31(1):99–110, 2001.
- [62] E. J. Smith, M. K. Dougherty, C. T. Russell, and D. J. Southwood. Scalar Helium Magnetometer Observations at Cassini Earth Swing-by. *J. Geophys. Res.*, 106(A12):30129–30139, Dec 2001.

## VITA

Michael K. Plante was born in Houston, Texas on October 13, 1983, the son of Ronald S. Plante and Karen A. Plante. Michael began programming in 1990, and programming in C in 1992. He graduated from Clear Brook High School in May, 2002. Michael passed his Fundamentals of Engineering (FE/EIT) exam for the Texas Board of Professional Engineers with a score of 94% in October of 2005. He secured a double degree in May, 2006 in Electrical Engineering and Computer Science from the University of Texas at Dallas in exactly 8 semesters with Collegium V honors. Michael was UT Dallas' third double-*summa cum laude*, with a GPA of 3.949. He began Ph.D. research for Dr. Duncan MacFarlane, in association with Polatomic, Inc., in the area of optically pumped helium magnetometers in June, 2006. He completed his M.S.E.E. in May, 2009 with a 4.0 GPA.

Michael has held several positions, including I.T. support at Data Systems and Solutions (at the time, a joint venture between SAIC and Rolls-Royce) in 2001 and assembly language embedded software development at The Boeing Company in 2004 and 2005. At Boeing, he wrote a portion of the code controlling the head-up display (HUD) in the backup flight software (BFS) for use during the OPS 3 descent phase on the Space Shuttle Orbiter.

Michael has been active in the UT Dallas Autonomous Underwater Vehicle (AUV) Team since January of 2006, and has worked on nearly every aspect of the AUV, including control loops, inertial navigation, client-server host software architecture (personally actively maintaining over one hundred thousand lines of code, as of June, 2010), embedded firmware (microcontroller and FPGA), UI design, computer vision processing, dynamics simulations, sonar processing, mixed-signal board design, and systems integration (specification, verification, and validation). In 2009 and 2010, he served as the team captain. The team placed second out 25 teams internationally in the 2008 AUVSI competition, held at the Space and Naval Warfare (SPAWAR) Systems Center in San Diego, and fifth out of a similar number of teams in 2006 and 2009.